

1980

The influence of turbulence on combustion in open pre-mixed flames

Eldon Stanley Powell
Iowa State University

Follow this and additional works at: <https://lib.dr.iastate.edu/rtd>

 Part of the [Mechanical Engineering Commons](#), and the [Oil, Gas, and Energy Commons](#)

Recommended Citation

Powell, Eldon Stanley, "The influence of turbulence on combustion in open pre-mixed flames " (1980). *Retrospective Theses and Dissertations*. 7119.
<https://lib.dr.iastate.edu/rtd/7119>

This Dissertation is brought to you for free and open access by the Iowa State University Capstones, Theses and Dissertations at Iowa State University Digital Repository. It has been accepted for inclusion in Retrospective Theses and Dissertations by an authorized administrator of Iowa State University Digital Repository. For more information, please contact digirep@iastate.edu.

INFORMATION TO USERS

This was produced from a copy of a document sent to us for microfilming. While the most advanced technological means to photograph and reproduce this document have been used, the quality is heavily dependent upon the quality of the material submitted.

The following explanation of techniques is provided to help you understand markings or notations which may appear on this reproduction.

1. The sign or "target" for pages apparently lacking from the document photographed is "Missing Page(s)". If it was possible to obtain the missing page(s) or section, they are spliced into the film along with adjacent pages. This may have necessitated cutting through an image and duplicating adjacent pages to assure you of complete continuity.
2. When an image on the film is obliterated with a round black mark it is an indication that the film inspector noticed either blurred copy because of movement during exposure, or duplicate copy. Unless we meant to delete copyrighted materials that should not have been filmed, you will find a good image of the page in the adjacent frame.
3. When a map, drawing or chart, etc., is part of the material being photographed the photographer has followed a definite method in "sectioning" the material. It is customary to begin filming at the upper left hand corner of a large sheet and to continue from left to right in equal sections with small overlaps. If necessary, sectioning is continued again—beginning below the first row and continuing on until complete.
4. For any illustrations that cannot be reproduced satisfactorily by xerography, photographic prints can be purchased at additional cost and tipped into your xerographic copy. Requests can be made to our Dissertations Customer Services Department.
5. Some pages in any document may have indistinct print. In all cases we have filmed the best available copy.

University
Microfilms
International

300 N. ZEEB ROAD, ANN ARBOR, MI 48106
18 BEDFORD ROW, LONDON WC1R 4EJ, ENGLAND

POWELL, ELDON STANLEY

THE INFLUENCE OF TURBULENCE ON COMBUSTION IN OPEN PRE-
MIXED FLAMES

Iowa State University

PH.D.

1980

University
Microfilms
International 300 N. Zeeb Road, Ann Arbor, MI 48106

PLEASE NOTE:

In all cases this material has been filmed in the best possible way from the available copy. Problems encountered with this document have been identified here with a check mark .

1. Glossy photographs _____
2. Colored illustrations _____
3. Photographs with dark background _____
4. Illustrations are poor copy _____
5. Print shows through as there is text on both sides of page _____
6. Indistinct, broken or small print on several pages
7. Tightly bound copy with print lost in spine _____
8. Computer printout pages with indistinct print _____
9. Page(s) _____ lacking when material received, and not available from school or author
10. Page(s) _____ seem to be missing in numbering only as text follows
11. Poor carbon copy _____
12. Not original copy, several pages with blurred type _____
13. Appendix pages are poor copy _____
14. Original copy with light type _____
15. Curling and wrinkled pages _____
16. Other _____

The influence of turbulence on combustion in open pre-mixed flames

by

Eldon Stanley Powell

A Dissertation Submitted to the
Graduate Faculty in Partial Fulfillment of the
Requirements for the Degree of
DOCTOR OF PHILOSOPHY

Majors: Aerospace Engineering
Mechanical Engineering

Approved:

Signature was redacted for privacy.

In Charge of Major Work

Signature was redacted for privacy.

For the Major Departments

Signature was redacted for privacy.

For the Graduate College

Iowa State University
Ames, Iowa

1980

TABLE OF CONTENTS

	<u>Page</u>
NOMENCLATURE	v
I. STATEMENT OF PURPOSE	1
II. REVIEW OF PREVIOUS WORK	2
A. Early Developments	2
B. Recent Turbulent Flame Speed Developments	4
C. Turbulent Flame Models	6
D. Computer Combustion Modeling	8
E. Review of Some Experimental Techniques	10
1. Temperature measurement	10
2. Ionization measurements	11
3. Sampling of flame region	12
4. Velocity measurements in flames	12
5. Optical methods of flame study	13
F. The Crossed-Beam Schlieren System	17
III. THEORETICAL BACKGROUND	19
A. Laminar Combustion	19
B. Turbulent Premixed Flame Theories	22
C. Correlation Technique for Data Reduction	24
IV. EXPERIMENTAL APPARATUS	28
A. Flow System	28
B. Instrumentation	35
C. Calibration of Flow System	38
D. Turbulent Flow Field Measurement	40
E. Instrument Calibration	42
F. Data Acquisition System	54
V. RESULTS	57

A. Preliminary Results	57
1. Convection speed	57
2. Signal spectra	60
B. Reaction Zone Modeling	70
1. Signal shape observations	70
2. Flame model development	71
C. Model Verification	77
1. Signal shape comparisons	77
2. Flame front motion	81
D. Qualitative Signal Observations	93
E. Model Based Data Analysis	96
1. Simple model analysis	96
2. Data reduction using simple model analysis	97
F. Concluding Flame Signal Observations	121
1. Off centerline observations	121
2. Kernels outside the model size range	122
G. Data Uncertainty	123
1. Flow system uncertainty	123
2. Instrumentation uncertainties	124
3. Analysis uncertainties	126
VI. SUMMARY, CONCLUSIONS, AND RECOMMENDATIONS	129
A. Summary	129
1. Instrument improvement	129
2. Model development and verification	130
B. Conclusions	130
C. Recommendations	131
1. Instrumentation improvement	131
2. Recommendations for future research	132
VII. REFERENCES	134
VIII. APPENDIX: MATHEMATICAL MODEL	139

A.	Derivation of Mathematical Model	139
1.	Central beam-kernel interaction	139
2.	Noncentral beam-kernel interaction	146
B.	Statistical Analysis of Signals	149
1.	Correlation	149
2.	Fourier transformation	151
C.	Derivation of Frequency Change Due to Flame Front Motion	154
1.	Converging flame front	154
2.	Diverging flame front	155
D.	Noncentral Beam-Kernel Interactions	156
1.	Probability analysis	156
2.	Interaction cross section	161

NOMENCLATURE

A	Distance from flame centerline to detector
A_f	Activity fraction
C	Covariance of parameters denoted by subscripts
C'	Correlation coefficient between parameters denoted by subscripts
e	Signal level
E	Unspecified function of time
E'	Fluctuating part of E
f	Frequency
G	Spectral energy distribution function
H_z	Height above burner exit plane
I	Interaction cross-section
K	Kernel number density distribution
L	Kernel size
\tilde{L}	Arithmetic mean of two adjacent kernel sizes
L'	Apparent diameter of kernel
L_{\max}	Maximum size kernel considered in simple model
L_{\min}	Minimum size kernel considered in simple model
n_1	Refractive index of flame region surrounding kernel
n_2	Refractive index of interior of flame kernel
P	Probability
r	Radial coordinate
R	Radius of kernels
\tilde{R}	Radius of interaction cross-section
S	Linear sensitivity of detectors

S_l	Laminar burning speed
S_t	Turbulent burning speed
S'	Linear power sensitivity of detectors
t	Time
T	Half of averaging or observation period
U	Mean approach speed
U_c	Convection speed
U'	Fluctuating speed
V	Speed
V_f	Volume fraction occupied by kernels
X, Y, Z	Cartesian coordinate directions
α	Angle
δ	Effective half width of beam
δ_l	Laminar flame thickness
η	Dimensionless length
θ	Beam deflection angle
κ	Wavenumber
λ	Wavelength
λ_g	Taylor microscale
Λ	Turbulent integral scale
ν	Viscosity (kinematic)
σ	Standard deviation of Gaussian distribution
τ	Delay time

Subscripts

o True or maximum

- a Pertaining to assembly A or signal A
- b Pertaining to assembly B or signal B
- c Pertaining to kernel center
- 1, 2 Distinct values of the same variable

Superscript

$\overline{(\)}$ Average

I. STATEMENT OF PURPOSE

Most flames in nature are turbulent. Care is exercised in many controlled flames to assure that they are turbulent, since the volumetric heat release rate of turbulent flames is larger than that of laminar flames. The concepts of laminar flames are reasonably well understood. Turbulence alone is poorly understood and this is even more so when turbulent fluctuations interact with the heat release of combustion.

A limiting factor in the study of turbulent combustion has been the difficulty of making measurements in the flame region. A new measurement technique was developed for this study and was used to study the structure of an open premixed turbulent flame. The study also included development of a physical model of the flame based on observations, mathematical modeling of the physical model, and analysis of the flame generated data using the assumed model.

II. REVIEW OF PREVIOUS WORK

A. Early Developments

The modern study of turbulent combustion began with Damkholer's (1) study of premixed propane-oxygen flames. Preflame turbulence was generated by fully-developed pipe flow. He made a theoretical study of the effect of two turbulent length scales in a flow incident on a laminar flame. For scales $\Lambda < \delta_{\lambda}$, the flame thickness, he assumed the increase in burning speed was due to the enhanced mixing in the flame front which would produce a thickened flame front. For scales $\Lambda \gg \delta_{\lambda}$, he assumed the effect of the flow fluctuations was to distort or wrinkle the flame front producing an increased flame surface area. This was the origin of what has become known as the wrinkled laminar flame concept. The separate effects of turbulent intensity, U' , for different scale lengths indicate that Damkholer considered both the scale length and intensity to be important.

Shchelkin (2) extended the analysis of Damkholer and modified his equation for the burning speed. He made two main postulates. First, for strong turbulence, the burning speed was assumed proportional to the intensity of the turbulence and independent of both scale and laminar burning speed. Second, for strong turbulence, the flame surface was assumed to become so distorted that the flame front breaks up into discrete islands of flame which are swept away by the fluctuating velocity. This was the first mention of a disperse flame model as distinct from the wrinkled laminar flame model which assumed a continuous but distorted flame surface.

These two studies generated great interest in the topic of turbulent combustion. Most ensuing work, initially, repeated and extended the experiments of Damkholer and Shchelkin. Karlovitz, et al. (3) reported the failure of a flame to propagate through strong velocity gradients. This failure was attributed to flame stretch, or gas phase quenching. They also reported evidence of holes in a flame front, the first experimental observation of a noncontinuous flame front. Wohl, et al. (4) developed an equation based on a distorted but continuous flame front. They fit an equation which was dependent upon intensity but independent of scale to their data from an enclosed burner.

Hottel, et al. (5) made one of the first studies where scale and intensity were controlled. From measurements on spark shadowgraphs, they concluded that the dimensions of the perturbations of the laminar flame front were a function of the scale and intensity of the turbulence and of the laminar flame speed. From their observations, they derived a relationship between the area increase of the flame front and the turbulent characteristics of the flow. The observed increase in flame speed was attributed to the increased flame front area. They also concluded that the local flame speed was little if any different from the laminar flame speed.

Scurlock and Grover (6) presented an analysis of the effect of turbulence on propagation of an infinite plane combustion wave. They assumed that the depth of the wrinkles caused by the turbulence was determined by the turbulent intensity, length scales, and the laminar flame speed. By assuming a geometry for the perturbations, they were able to predict an increase of flame front area.

Bowditch (7) studied an open propane air flame. He arrived at an equation, based on his data, which was strongly dependent on laminar burning speed and turbulent intensity but independent of scale. Turbulence generated by the flame was assumed to dominate the combustion.

The previously mentioned studies represent the period through 1954. Turbulent combustion studies continued at an active pace following these early developments. The next group of studies discussed are from the period beginning in the mid-1970's.

B. Recent Turbulent Flame Speed Developments

One of the most interesting recent experiments was reported by Ballal and LeFebvre (8). They determined the flame speed in an enclosed burner using a stoichiometric mixture of propane and air for a variety of turbulent intensities and scale lengths. Three ranges of intensity level were studied: $U' < 2 S_L$, $U' \sim 2 S_L$, and $U' > 2 S_L$ where S_L is the laminar flame speed. The turbulent length scales studied varied from $\Lambda = 0.28$ mm to $\Lambda = 2.5$ mm. The conclusions drawn were that in the first range, S_t , the turbulent burning speed, was a strong function of U' and integral scale Λ ; in the second range, S_t was independent of scale length but still a function of U' ; in the third range, S_t decreased with increasing scale length and increased as U' increased. The explanation admits the possibility of a disperse flame but was given in terms of a distorted continuous flame.

Andrews, et al. (9) studied turbulent burning speed in a stirred reactor in methane-air and ethane-air mixtures at atmospheric pressure

and temperature. They plotted the ratio of turbulent burning speed divided by laminar burning speed (S_t/S_L) vs turbulent Reynolds number $Re_\lambda (= U' \lambda_g / \nu)$ where λ_g is the Taylor microscale). The plots showed that the ratio S_t/S_L increased as the turbulent Reynolds number increased. The plots also exhibited the large scatter in the data. In a later report Andrews, et al. (10) proposed a correlation of S_t/S_L vs Re_λ . They include selected data which appears to support their correlation.

Sriramulu, et al. (11) pointed out the interdependence of U' and λ_g for any given turbulent flow. They asserted that Re_λ alone was not sufficient to correlate turbulent burning speed and that because of the relationships existing among variously defined turbulence Reynolds numbers, no Reynolds number would be adequate.

Vilyunov (12) developed an equation for turbulent burning speed based on "dimensional estimates and similarity." He considered some limiting cases but allowed enough undefined constants to assure a good correlation between his equation and the selected data. He assumed the most influential turbulent fluctuations were large low frequency pulsations, supporting the wrinkled laminar flame model.

Kuznetsov (13) introduced a flame thickness parameter into his analysis of turbulent burning speed. The result derived was that the burning speed increased in proportion to the integral scale of the turbulence and the mean square of the velocity fluctuations. His analysis was based on the wrinkled laminar flame model.

The turbulent flame studies mentioned illustrate the fact that despite much effort by many outstanding researchers, the mechanisms

of turbulent flame propagation are still poorly understood. The understanding is so limited that the most basic macroscopic property, the flame speed, cannot be predicted accurately except in cases where it has been experimentally determined.

C. Turbulent Flame Models

The wrinkled laminar flame model proposed by Damkholer was the first turbulent flame model. In this section, two other theories will be described.

Summerfield, et al. (14, 15) proposed an alternative to the wrinkled laminar flame model of flame structure in a turbulent flow. They assumed that the combustion occurred in "a region of distributed reaction, with smooth spatial variation of the time average values of composition and temperature much like a thickened laminar flame." This was similar to the action of small scale length turbulence as postulated by Damkholer (1). Their model, called a distributed reaction model, was supported by a variety of measurements in a two-dimensional pilot-anchored lean methane-air flame.

One description of a disperse flame was given by Howe and Shipman (16). In order to explain their observations in an enclosed flame, they proposed a model in which the flame region was assumed to be composed of a mixture of burned volumes and unburned volumes. One case discussed was a distribution of unburned isolated parcels in burned surroundings. The second case corresponded to burned isolated parcels in unburned surroundings. In both cases, the reaction was assumed to

occur at the burned-unburned interface. They assumed that parcels change size either by burning or by splitting due to shear. For the shear dominated case, they derived an equation for the time dependent size distribution of parcels. They assumed spherical parcels with the initial distribution given by an exponential function of the radius, R . The initial condition for their calculation was assumed to be isolated burned parcels distributed in unburned surroundings. The transition to isolated unburned parcels dispersed in burned surroundings was assumed to be continuous. Their choice of shear dominated parcel dynamics for an enclosed flame was logical because of the increase in mean velocity which accompanies combustion. The predictions of the model were supported by their data.

Basu and Bhaduri (17) report a study using a spark shadowgraph and an ionization probe to investigate an open premixed turbulent flame. Their conclusions were that both the wrinkled laminar flame and the disperse flame models are applicable for certain conditions and that the transition from one to the other is continuous. They did not report scale length, intensity or chemical composition in the unburned gas so comparison with any other study is impossible. They reported homogeneous pockets or volumes in the vicinity of the mean flame front which they attributed to the break up of the wrinkled laminar flame front. Their results could be interpreted to support the model of Howe and Shipman.

D. Computer Combustion Modeling

Libby (18) developed a turbulent flame model using the chemical conservation equations. The set of equations contains more unknowns than equations. This closure problem was left to be solved separately for each case. One of the conclusions was the prediction of a disperse flame for inhomogeneous fuel-oxidizer mixtures.

Gibson and Libby (19) modeled the concentrations of products and reactants near a reacting surface. They simulated the reaction experimentally with an inhomogeneous liquid acid base mixture. This procedure recognizes the concept of a reacting interface which was especially appropriate for a diffusion flame.

Spalding (20, 21) developed a computer model of turbulent flames with emphasis on diffusion flames and premixed confined flames downstream of flame holders. Mixing length models were used to close the equations at the level of kinetic energy of turbulence, vorticity fluctuation, and mean square concentration fluctuation. A mixture of fragments of unburned and almost fully burned gases was assumed for a confined premixed flame. The rate of burning was assumed to be controlled by the rate at which the fragments of unburned gas were broken into smaller fragments. An eddy breakup process, dominated by mean shear, was postulated as the mechanism for breaking fragments into smaller fragments. The predictions of the model were consistent with observations for the two cases emphasized.

Bray and Moss (22) developed a computer model of premixed turbulent flames. The modeling of the chemistry was simplified by assuming a

global, irreversible, one step transformation from reactants to products. The modeling of the fluid mechanics of combustion was simplified by the following assumptions: reactants and products were ideal gases, the specific heats of reactants and products were equal and constant, thermal and pressure diffusion were negligible, normal binary diffusion was described by Ficks law, the reaction was isobaric, pressure fluctuations were negligible, all velocities were small in comparison to the local sonic speed, and the flow was adiabatic. The model equations were closed at the level of turbulent kinetic energy and mean square fluctuation of product concentration by postulating a probability density function (PDF) for product concentration. They developed probability density functions based on the physical models as described by Damkholer, Summerfield, et al., and Howe and Shipman. The conclusions included: the reaction rate "does not appear to be very sensitive to the form of the assumed PDF." Direct measurement of the PDF of concentration, or something directly related to it, may allow determination of the proper PDF but mean measurements are unlikely to.

Champion, et al. (23) modified the model of Bray and Moss by replacing the product concentration PDF with a temperature PDF and by adding a ten step reaction model for the combustion of propane and air. They showed results which indicate that the temperature fluctuations and turbulent kinetic energy are relatively insensitive to the form of the PDF. One distinct advantage of the PDF method was that it was not limited to small fluctuations.

Other investigators have been active in turbulent flame modeling (24, 25, 26, 27 and others), but the models are similar to those

discussed above. None of the computational models studied contain any significant physical modeling. All are macroscopic models of the action of the entire flame region.

E. Review of Some Experimental Techniques

In a combustion process, all thermodynamic properties of the reactants change. An instrument that responds to change in any property can be used to study the flame process. Most measurements in a flame are made at a fixed point in the flame region.

1. Temperature measurement

One means of measuring temperature changes is to use a fine wire thermocouple in the flame region. Errors in the measured temperature can be caused by alteration of the flame due to probe interference and by imprecisely known heat transfer characteristics in the flame. The finite thermal capacity of the wire limits the frequency response of the thermocouple when measuring fluctuating temperature. The frequency response can be improved by selective amplification of the signal. The other errors can be reduced by careful design and operation but cannot be eliminated.

Parker and Guillon (28) used a 12.5 μm diameter hot wire operated at low overheats to study temperature fluctuations in an open methane-air flame. The problems of imprecisely known heat transfer characteristics, possible probe interference, and signal interpretation mentioned above remain. In addition, durability of the wire can be a serious problem.

By correlating the output of two hot wires, operating as resistance thermometers, Ho, et al. (29) obtained statistical information about the shape, in two dimensions, of temperature inhomogeneities in the flame region.

One method of temperature measurement which does not suffer the problems of insertion of a probe into the flame is the spectral line reversal method. A complete discussion of the method is contained in Reference 30. Briefly, the temperature is determined by comparison of the absorption of some spectral line of a constituent in the flame to the brightness of the same spectral line from a reference source of known emissivity and temperature. The most commonly used spectral line is the sodium D line. The spectral line reversal method can give accurate results, averaged along a line through the flame. Two major disadvantages of the method are that the results represent the average temperature through the flame and that the emitter must often be artificially introduced into the flame. Only miniscule amounts of sodium need be used due to the strength of the sodium D line.

2. Ionization measurements

Double ionization probes can be used to observe the instantaneous electrical conductivity of the flame region (15, 17). The flame front is characterized by a much higher conductivity than the reactants or the equilibrium products. Ionization probe traverses through laminar flame fronts confirm this increased conductivity and yield flame thicknesses in agreement with other methods. Investigators disagree in the interpretation of results obtained with ionization probes (31), since the in-

creased conductivity results from nonequilibrium chemi-ionization. The output represents an average conductivity between two points so information of interest in small scale length turbulent flames is not available.

3. Sampling of flame region

Fristrom (32) discusses several methods of studying the changing chemical composition of the flame region. Direct sampling of the flame region will be discussed briefly. If material is removed from the flame, its composition can be determined by standard techniques. The amount of material required depends upon the analysis technique to be used. The trade-off between small probe size for minimum flow disturbance and large size for quick sampling determines the probe design. Identification of unstable species is difficult because of continued reaction of the sample after it is withdrawn from the flame. The method is not suited for study of unsteady flames because of the time required to obtain a sample. The sample gives information about the composition at a point and is of limited value for the study of the fluid mechanical structure of a flame.

4. Velocity measurements in flames

Measurement of velocities in flame regions using hot wires or hot films is difficult. The wire temperature required for significant velocity sensitivity in most flame systems is in excess of the melting temperature of common hot wire materials.

Velocities in the reaction zone can be measured using laser velocimeters. Laser velocimeters require solid particles moving

with the flow to interact with the focused beam for their operation. If measurements in the post flame region are to be made, the concentration of solid particles in the reactants must be large, since the expansion in the flame will reduce the concentration. Particles which are unaffected by the flame and which do not affect the flame must be used. Velocities in a turbulent flame region cannot unambiguously be related to a flame structure.

5. Optical methods of flame study

Three general types of optical methods will be described in this section. They are spectroscopy, direct photography, and refractive index methods. Primary emphasis will be on the third.

Spectroscopy is the study of composition by the selective absorption or emission of light by molecules in the flame. Dieke (33) presents a description of the method. Spectroscopy is used to determine the concentrations of selected molecules. Both time averages and instantaneous concentrations can be determined. Spatial resolution is a serious limitation of most systems, since the measurement is an average along a ray through the region.

Direct photography (34) of the flame self-luminosity is the simplest optical method of flame study. The only equipment required is a camera and the camera need not be sophisticated. The additive effects of multiple light sources in line, with respect to the camera, can cause difficulty in interpretation of the photographs. If a time exposure of a turbulent flame is made, the line of maximum optical density on the negative can be used as the mean flame position. This is informative

but gives little information about flame structure. If inert reflective particles are introduced into the pre-flame flow and illuminated stroboscopically while a time exposure is being made, the particle paths through the flame can be determined. Much like velocity, particle paths yield little direct information about the detailed structure of the reaction region.

An excellent explanation of the techniques based on the refractive index variations of a flame region is given by Weinberg (35). Most texts on combustion contain examples of the products of these methods. These methods, interferometry, Schlieren and shadow photography depend on making visible the variations in refractive index in the flame. The refractive index of a gaseous medium depends on both composition and density and these properties change simultaneously in the flame front. The index of refraction is normally a linear function of density for fixed composition. If the light source is monochromatic as in the case of a laser light source and if the laser wavelength corresponds to the wavelength of an absorption band of a molecule in the flame region, the linear relationship is not valid. Only a small part of the energy of a white light beam will be absorbed so the linear relationship may be nearly valid. The wavelength of the absorption bands of a molecule are determined by the molecular structure so the wavelength of the absorption bands change in a reacting flow.

A typical Schlieren system is shown schematically in Figure II-1. The light from the source S is focused on a small aperture A. The lighted aperture is placed at the focal point of lens L so that a collimated beam of light is produced. A second lens L' focuses the

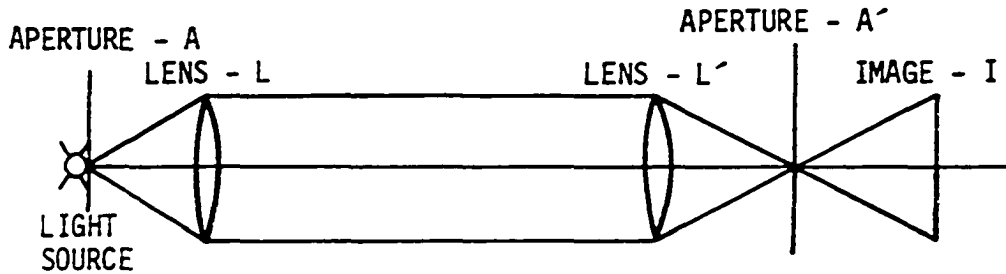


Figure II-1. Schematic of Simple Schlieren System.

collimated beam on a second aperture A' which intercepts part of the beam, uniformly darkening the image at I . Some of the light rays will be deflected if the collimated beam is passed through a region of inhomogeneous refractive index. The lens L' will focus the deflected rays to a slightly different point at aperture A' . Some of the rays intercepted by the aperture A' in the undisturbed beam will pass the aperture due to their deflection. Similarly, some of the rays which were passed by the aperture in the undisturbed beam will be intercepted due to their deflection. The intensity of the image at I varies from point-to-point as a result of the deflections of the light rays. The variation indicates the location of gradients in refractive index.

The lenses L and L' are often replaced in practice by concave mirrors for reasons of economy and because of the superior optical quality. Refractive index gradients in the direction of the beam do not deflect the beam. For this reason, Schlieren images are an incomplete picture of the refractive index variations encountered by the beam. In laminar flames, the flame front produces distinct images with little confusion. Schlieren images are a result of deflection of light rays from their initial path. Shadowgraph images are made using a similar light source but without a second focusing element and without a second aperture. The shadowgraph images represent the deflection of light rays relative to the remainder of the beam, or the focusing of the beam by the refractive index field. The relative deflection is determined by the gradient of the gradient of the refractive index. This property of shadowgraphs makes them well-suited to the study of small scale turbulent structure. Sub-microsecond light pulses can be generated which effectively freezes the fastest fluctuations in refractive index. In turbulent flames, the instantaneous motion can be stopped but the undulations in the flame region create multiple gradients in the path of each ray. The effects of multiple gradients is to so confuse the image that unambiguous interpretation is impossible. An extensive study of photographic methods led Grummer, et al. (36) to conclude that Schlieren and shadowgraph methods were not suited for determination of the structure of the turbulent flame brush.

F. The Crossed-Beam Schlieren System

Fisher and Krause (37) developed a dual beam cross-correlation technique to circumvent the integrating effect of the single system. A schematic of the apparatus is shown in Figure II-2. The region of turbulent fluctuations is contained within the dashed line. The turbulence is convected in a direction perpendicular to the plane of the figure. They studied the fluctuation in extinction coefficient in a subsonic jet seeded to scatter part of the incident beam energy. They showed that the time mean product (or covariance) of two fluctuating integrated signals represents the average product of the fluctuation in a sampling volume near the intersection of the crossed-beams. Wilson

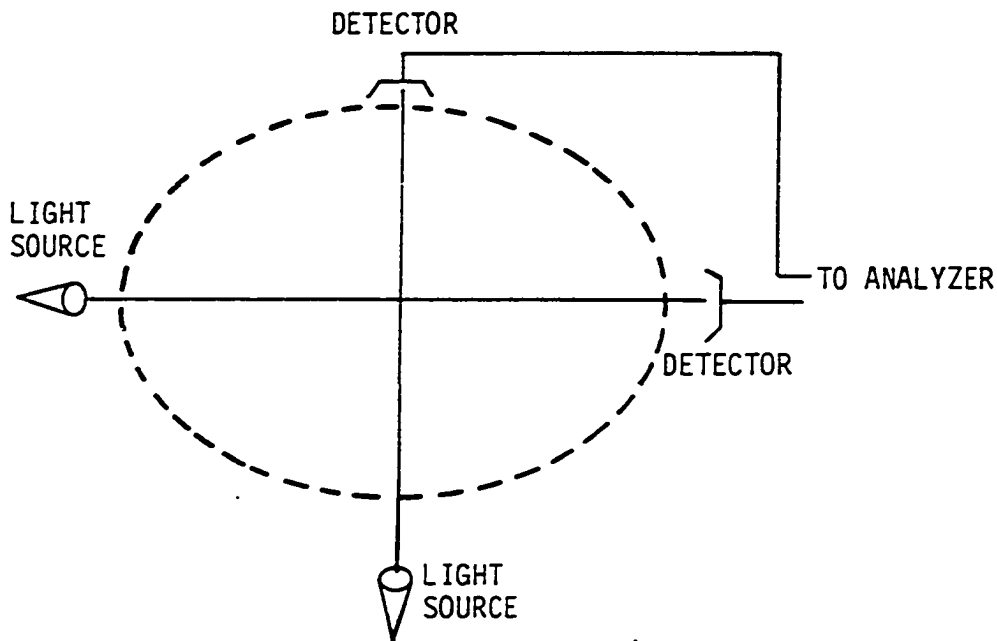


Figure II-2. Schematic of Experimental Setup of Fischer and Krause.

and Damkevala (38) used a similar instrument, but used the beam fluctuations caused by turbulent density fluctuations (crossed-beam Schlieren) to study density gradients in a subsonic jet. They showed that the spectrum of the cross-correlation is one component of the three-dimensional turbulent energy spectrum. Martin (39) used the same instrument to study the decay of isotropic grid generated temperature inhomogeneities. The first application of the crossed-beam Schlieren to a turbulent flame was by Parks (40). He demonstrated that with certain limitations, useful local information could be obtained in non-isotropic reacting turbulent regions.

If sufficiently small size beams are used for the crossed-beam Schlieren system, each beam can be assumed to be a single ray. The beams then are deflected as a whole eliminating the ambiguity caused by beam distortion which occurs in a beam of finite size. Cross-correlation circumvents the integral effect present in all optical systems. For these reasons, the crossed-beam Schlieren system is an attractive tool for turbulent flame studies and was used in this study.

III. THEORETICAL BACKGROUND

A brief review of the theoretical background of combustion and the correlation technique for data reduction will be presented here.

A. Laminar Combustion

Many adequate books dealing with combustion are available. References 41-47 are suggested for a complete treatment of the topic. As a model for laminar combustion, consider a small homogeneous volume of reactants of known thermodynamic state in a uniform flow toward a stationary flame. At a large distance from the flame, the reactants are unaffected by the flame. As the flame is approached, energy is transferred to the volume in the form of heat by radiation and conduction. The energy transfer increases as the reactants approach the flame. At some point, sufficient energy will have been absorbed by the reactants that the reaction will begin. As the reaction proceeds, more energy will be liberated, accelerating the reaction. Reaction products will diffuse toward the reactants which also increases the reaction rate. This continues until the reactants are consumed. The entire process, from the first detectable change in the reactants until virtually all reactants are consumed, usually occurs in a distance of less than one millimeter at normal temperature and pressure.

The precise chemical mechanisms are not completely known except for the simplest reactions. The generally accepted hypothesis is that the stable reactants are transformed into an excited state by collisions with high energy molecules in the flame region. These excited

molecules then react to form the stable products of combustion and more high energy molecules. The unknown participants in most reactions are the high energy molecules and the excited molecules. The molecules in the excited state normally have short lifetimes and are confined to narrow regions of the reaction zone. The possibility of multiple high energy species and multiple excited states complicates the task of determining the exact chemical mechanism.

Downstream of the flame is a relaxation zone. In this region, typically an order of magnitude larger than the reaction zone, the combustion products gradually approach chemical equilibrium. The flame, therefore, can be divided into three regions: a preheat zone, a reaction zone, and a relaxation zone. The entire process is continuous, so definition of the edges of the individual zones is somewhat arbitrary. Similarly, the length of the entire region depends on arbitrary definitions but is typically on the order of one centimeter. The flame region is schematically illustrated in Figure III-1.

A number of parameters are defined to quantify laminar flames. They include the adiabatic flame temperature, the flame speed, ignition energy, and flame thickness. The adiabatic flame temperature is the temperature the equilibrium products would assume if none of the energy of reaction was transferred out of the system (46). In practice the final temperature of the products is less than the adiabatic flame temperature because of heat transfer to the surroundings. The adiabatic flame temperature is a theoretical rather than experimental parameter. It is useful for comparison of various reactants.

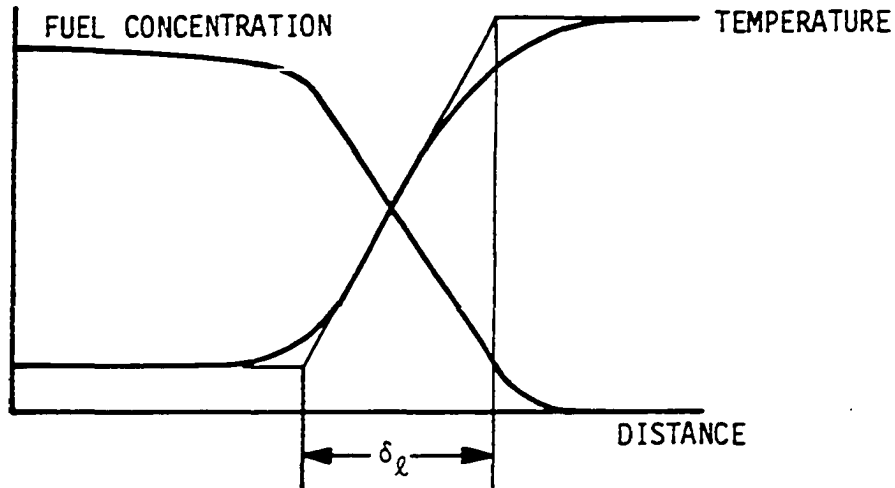


Figure III-1. Schematic Representation of a Laminar Flame Zone.

The flame speed is the speed of the reaction zone relative to the reactants. It is dependent upon the thermodynamic state of the reactants. Theoretical determination of the flame speed is difficult since it depends on many, often unknown, transport processes and rates. It is a fundamental property of the flame which must be determined experimentally.

The ignition energy is the amount of energy which must be added to a mixture of reactants to initiate a self-sustaining reaction. The ignition energy depends on the thermodynamic state of the reactants and the method of energy addition. In some instances, transport properties and system geometry are important. The minimum ignition energy is

determined by spark discharge between fine electrodes placed in the reactants.

The flame thickness can be defined in many ways. One common definition is the distance in the flow direction between the point where the temperature rise has reached prescribed fractions of the total temperature rise. For instance, the flame thickness could be defined as the distance between the points where the local temperature minus the initial temperature divided by the final temperature minus the initial temperature equalled 0.05 and 0.95. Another definition is the ratio of the total temperature change divided by the maximum temperature gradient in the flow direction. This definition is shown schematically in Figure III-1. These two definitions do not necessarily give consistent comparative results so care is required in their use.

B. Turbulent Premixed Flame Theories

Flames with thoroughly mixed reactants and flames with initially separate reactants are basically different. For the latter, fluid mechanical mixing is necessary to bring the reactants into contact and is therefore normally the controlling combustion mechanism. For the former, the effect of turbulence is not as clear. The three theories discussed here are based on experimental observations. All have been used to attempt to explain the increased burning speed observed in turbulent premixed flames.

The original theory was the wrinkled laminar flame hypothesis

of Damkholer (1). He assumed that if the scale length of the turbulence was large compared to the flame thickness, the action of the fluctuating velocity was to distort the smooth laminar flame. A continuous front would be formed but the surface area of the flame and the burning rate would be increased. For the conditions studied by Damkholer, the wrinkled laminar flame theory explained the results using a reasonable assumption for increased area. Damkholer also postulated a mechanism for the effect of small scale length turbulence. He assumed that for scales smaller than the laminar flame thickness, the effect of turbulence was to enhance the transport processes within the flame. This would produce a thickened but essentially smooth flame front. The increased volume due to the thickened flame was responsible for increasing the burning rate.

Summerfield, et al. (14, 15) expounded at greater length on the second theory which they called the distributed reaction model. The flame surface was replaced by a thickened reaction zone through which the average values of temperature and composition changed smoothly and continuously. The reaction rates were determined by the appropriate turbulent transport processes. The wrinkled laminar flame and the distributed reaction models are plausible. Each is most likely applicable over different ranges of turbulent intensity and scale length for some combustion systems.

The best description of the third theory, the disperse flame model is Reference 16. The combustion zone was characterized as parcels of burned (or unburned) gas surrounded by unburned (or burned) gas. Laminar like flames were assumed at the interface between the burned

and unburned gas. The source of the burning parcels was assumed to be the rupture of the laminar flame surface by shear strains. This assumption recognized the effect of turbulent speed fluctuations and scale lengths and the effect of mean shear on the flame structure. The implied assumption was that the turbulence affects the geometry of the flame front without any significant effect on the transport properties within the flame. There appears to have been little subsequent work based on the disperse flame model.

The wrinkled laminar flame and the disperse flame models assumed a distorted laminar like flame. The geometry of the flame front distinguishes the two. The distributed reaction model assumed a laminar like geometry but an altered reaction region.

It is likely that all three models are applicable for certain conditions, and that some combustion systems will possess characteristics of more than one model. The criterion for existence of any specific type are unknown.

C. Correlation Technique for Data Reduction

The technique of signal correlation is used in analysis of many different types of data. It is the technique applied in this study which allows local information to be obtained from the integrated Schlieren signals. For this reason and because the method is not commonly used, it will be reviewed. Reference (48) is suggested for a more general discussion and Reference (49) for an application to incompressible turbulent flows.

Consider two statistically stationary time varying continuous functions of zero mean. Denote the functions as $E_a(t)$ and $E_b(t)$. The auto (or self) covariance of function $E_a(t)$ is defined as

$$C_{aa}(\tau) = \frac{1}{2T} \int_{t-T}^{t+T} E_a(t)E_a(t + \tau)dt \quad (\text{III-1})$$

For the special case $\tau = 0$, $C_{aa}(0)$ is the mean square of the function $E_a(t)$. For convenience, divide both sides of the equation by the mean square $\overline{E_a^2}$. This restricts the function to the range $(-1, 1)$ and allows functions whose value is dimensional to be studied without mathematical difficulties. The normalized covariance is known as the correlation $C'_{aa}(\tau)$. If the function $E_a(t)$ is periodic or contains periodic components, the auto correlation will emphasize the periodic component. The emphasis appears as a local maximum in the correlation function at times τ corresponding to the period of the component. If the function $E_a(t)$ represents a random variable, the correlation will decrease with increasing time τ . In this case, the integral

$$\int_0^{\infty} C'_{aa}(\tau)d\tau$$

converges. The value of the integral is one measure of the delay required for the function to become independent of its present value.

The average product

$$C_{ab}(\tau) = \frac{1}{2T} \int_{t-T}^{t+T} E_a(t)E_b(t + \tau)dt \quad (\text{III-2})$$

is the cross covariance of the functions $E_a(t)$ and $E_b(t)$. $C_{ab}(t)$

can be divided by $(\overline{E_a^2} \overline{E_b^2})^{1/2}$. The range is then $(-1, 1)$ and the cross correlation is dimensionless. Unlike the auto correlation, the cross correlation does not necessarily reach a maximum value of 1 nor does its maximum occur at zero delay time. $C'_{ab}(\tau)$ represents the extent to which the functions $E_a(t)$ and $E_b(t)$ are linearly related. If the functions are independent, $C'_{ab}(\tau)$ will be zero for all τ . If $E_a(t)$ and $E_b(t)$ have some common component, the common component will be emphasized by the cross correlation.

Assume $E_a(t) = E(t) + E'_a(t)$ and $E_b(t) = E(t) + E'_b(t)$ and that $E(t)$, $E'_a(t)$, and $E'_b(t)$ are mutually independent. It is easily shown that

$$C'_{ab}(0) = \overline{E^2} / [(\overline{E^2} + \overline{E_a'^2})^{1/2} (\overline{E^2} + \overline{E_b'^2})^{1/2}] \quad (\text{III-3})$$

which shows the emphasis of the common component.

The output of the detectors used in the crossed-beam Schlieren system is the result of local beam deflections integrated along the beams. For the case when the beams are orthogonal, it has been shown (37) that the cross correlation C'_{ab} is the normalized output of the detectors due to the conditions in their common sampling volume. For the case when the output is determined by the Schlieren effect, Wilson and Damkevala (38) have shown that for isotropic turbulence, the cross covariance is related to density fluctuations near the intersection of the beams.

If the local processes which cause a detector output are being convected past the instrument, the cross correlation can be formed in such a way that mean convective speed can be determined. If one beam of the crossed-beam Schlieren system is displaced in the streamwise

direction, the cross correlation will have its maximum value at some nonzero delay. The delay will correspond to the most likely time of flight from one beam to the other. The known displacement divided by the delay, therefore, gives the most likely convection speed. Determination of the convection speed in this manner requires only that the signal causing disturbances generate repeatable signals in the two beams and that the time of flight is not a uniformly distributed random function. If the variation in individual times of flight from one beam to the other is large, the correlogram (the plot of the correlation vs delay), will have a broadened peak. Broadening will also occur due to finite signal duration.

The cross correlation technique as described here was applied in this study.

IV. EXPERIMENTAL APPARATUS

A. Flow System

The flow system is shown schematically in Figure IV-1. The combustible mixture used was commercial propane and air. The propane was supplied by standard cylinders mounted in the room adjacent to the experimental set-up. The propane cylinders were filled to a pressure of $1.5 \text{ E}+06 \text{ Pa}$. For safety, the pressure was reduced by a regulator at the cylinder to about $1.25 \text{ E}+05 \text{ Pa}$. The propane was passed through a double tube heat exchanger to counteract the cooling caused by liquid vaporization and throttling in the regulator. The propane temperature was maintained at $294^\circ\text{K} \pm 1^\circ\text{K}$. The propane flowed through a needle valve and rotameter and was injected radially into the air flow line.

Air was supplied by a low pressure compressor and stored in outdoor underground tanks ($25 \text{ m}^3 @ 2 \text{ E}+06 \text{ Pa}$). The air pressure at the apparatus was maintained slightly above atmospheric ($1.4 \text{ E}+05 \text{ Pa}$) by a large capacity regulator at the branch point from the pressure system. The flow rate was controlled by a cone valve and measured by a rotameter. No attempt was made to control the air temperature. After about 3 minutes, the air temperature stabilized at $294^\circ\text{K} \pm 2^\circ\text{K}$. From the rotameter, the air flowed through a series of fittings to where the propane was injected. Due to the turbulence in the pipe flow, complete mixing of the air and propane was assured within a few diameters of the injection point. From the point of mixing, the gases flowed through about 1 m of 5 cm nominal inside diameter pipe into about 3 m

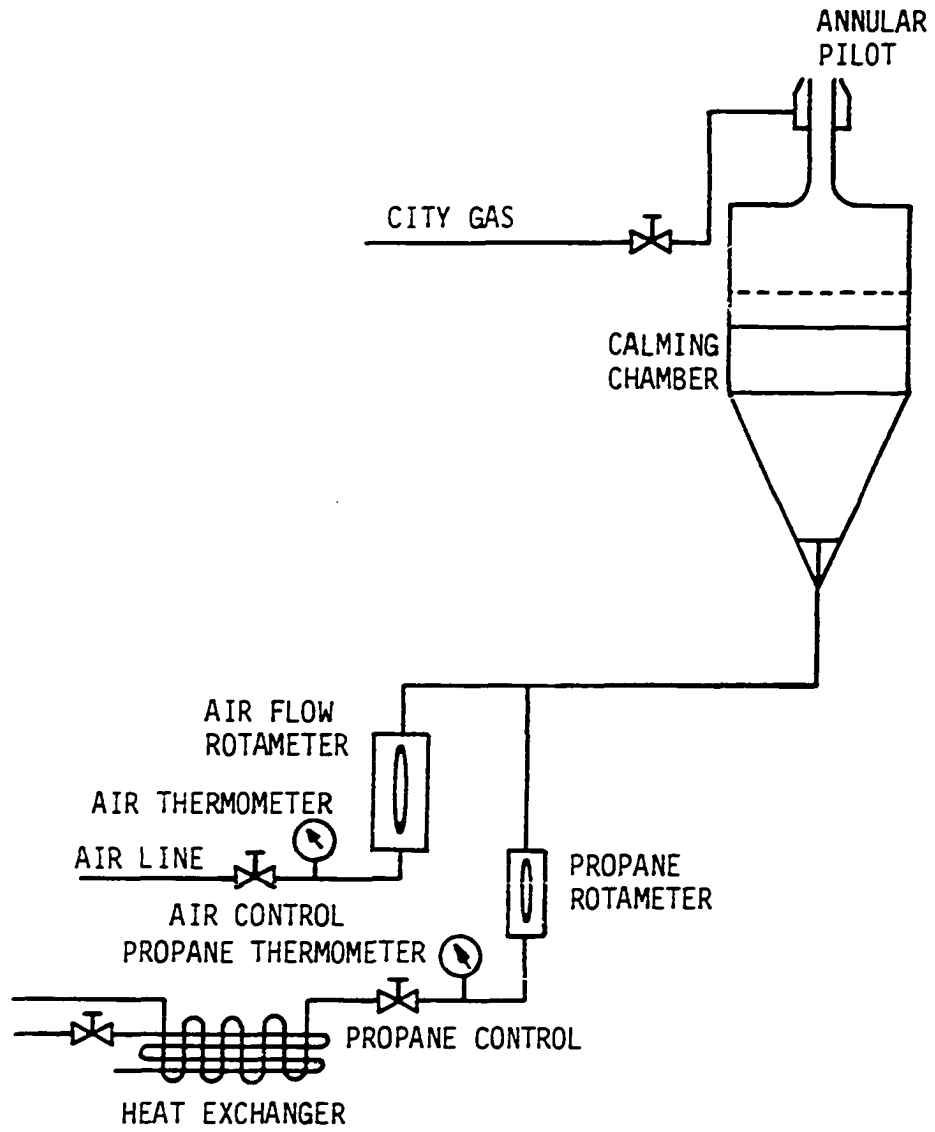


Figure IV-1. Schematic of Flow System.

of flexible tubing. The tubing mechanically isolated the flow control apparatus from the remainder of the combustion facility.

The gas then entered the stilling chamber consisting of an inverted cone and two straight sections. The inverted cone was 1.2 m long. The diameter increased from 5 cm to 60 cm. A four bladed flow straightener was placed in the apex of the cone to reduce any swirl created at the exit of the flexible tube. Atop this cone were the two straight sections, each 60 cm in diameter and 30 cm long. Aluminum screens were mounted between each two sections to reduce turbulence. In the lower straight section, approximately 7000 plastic straws, 20 cm long and 0.6 cm diameter, were placed on end creating a honeycomb through which the flow passed. For the maximum velocity, the pipe Reynolds number of each straw was about 35. Under these conditions, the length of the straws was at least an order of magnitude greater than the hydrodynamic entry length. Hence, the exit flow was fully developed small scale turbulence and equally important, the flow restriction was sufficient that any nonuniformity in velocity across the cylinder would be greatly reduced. Ten cm downstream from the exit of the straw honeycomb, the flow passed through another screen and then through the final 30 cm section, allowing time for the small scale turbulence to decay.

The final internal barrier to the flow was a standard 80 mesh brass soil sieve. The primary function of the sieve, mounted just upstream of the exit was to prevent flashback into the chamber if the flow speed ever became less than the burning speed. The exit was a short circular cross-section contraction. The area reduction from the chamber to the exit, was about 94 to 1. The turbulent intensity in the

exit plane, including instrument noise, was less than 0.5%. The volume of the stilling chamber was about 0.3 m^3 .

The turbulence was generated by a perforated disc mounted at the exit plane. The disc is shown 3/4 size in Figure IV-2. The diameter of the holes was 0.64 cm and the center-to-center spacing was 0.96 cm yielding a ratio of hole area to disc area of 0.4. The disc is made of thin steel to withstand flashback. This disc and the sieve were sufficient to provide safe operation.

The burner tube was 6.3 cm inside diameter 45 cm long hard copper tube. This length gave a ratio of tube length to hole diameter of 70 assuring reasonably homogeneous isotropic turbulence outside the tube boundary layer.

Since the approach speed was greater than the burning speed of the mixture, a flame holder was required. Numerous methods were tried and rejected. Among them were: an electrically heated coil which was difficult to control, a steel extension tube heated by gas jets which proved to be too cumbersome, and a ring of jets of pure city gas. The last worked but produced a flame with a sawtooth base as depicted in Figure IV-3. Since this could possibly affect the turbulent character of the flame, an annular pilot flame burner was built. The flame holder and resulting flame are shown in Figure IV-4. The flow rate was adjusted to the minimum required to anchor the main flame.

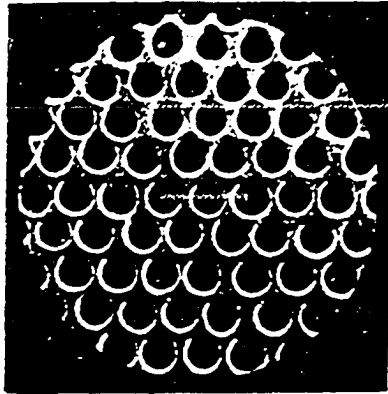


Figure IV-2. Perforated Disc Turbulence Generator.

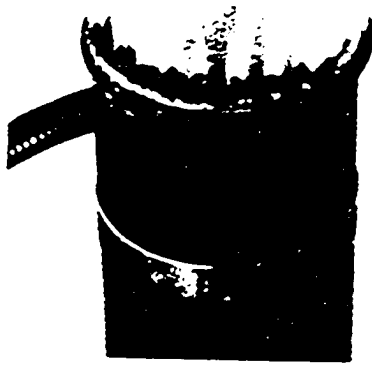


Figure IV-3. Flame Produced by Ring of City Gas Jets.

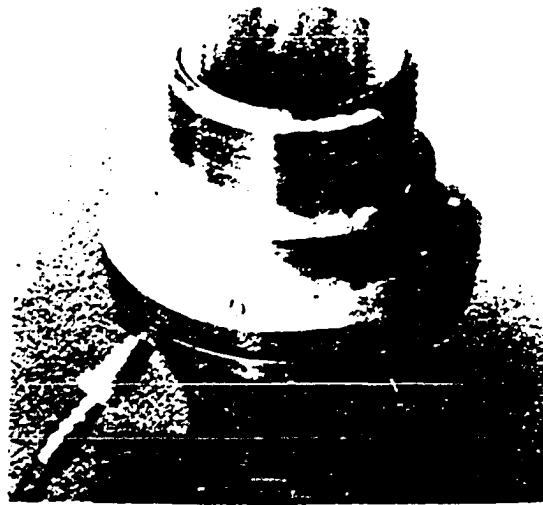


Figure IV-4. Flame Produced by Annular Pilot Flame Holder.

B. Instrumentation

The basic instrument used in this study was a crossed-beam Schlieren system. The instrument consists of two identical (ideally) assemblies, each consisting of a laser light source and its mount and a light sensitive detector and its mount. Since the individual as well as combined response of the assemblies was important, they were designated in use as assemblies A and B to indicate which (or both) was under consideration.

The light source for each assembly was a 2 mw HE-NE laser mounted on a mill table. The micrometer adjustment of the mill table allowed a total movement of approximately 14 cm in the streamwise and lateral directions. The mill tables were mounted on horizontal shafts which were mounted by split clamps on vertical shafts. The vertical shafts, 2.55 cm diameter steel 1.5 m long were bolted to the exit plane of the chamber. The tops of the shafts were secured by braces which joined each shaft to the two adjacent shafts. The resulting cage rigidly fixed the instrument to the chamber and the burner.

The horizontal shafts could be rotated and clamped so that the laser beam could be adjusted to any angle. The vertical position of the horizontal shafts was continuously variable over the entire 1.5 m of the vertical shafts.

Coarse laser positioning was done by raising or lowering the mill table mounts on the vertical shafts. Fine adjustments were made by adjusting the mill tables. The lasers were positioned a measured distance from the burner exit each time they were moved. In most cases,

the beams were set to have a small common sampling volume. One beam was positioned and the other was moved until they intersected. The flame was then ignited and after the systems had reached constant temperature, the detectors were adjusted to give zero mean output.

The laser beams passed through the flame region where they were deflected by density gradients, past knife edges which intercepted part of each beam and through converging lenses which focused them onto photodiodes. The arrangement is shown schematically in Figure IV-5. The output of the photodiode circuit was proportional to the laser power (assumed constant) and the fraction of the beam which passed the knife edge which in turn was proportional to the deflection of the beam by the flame. For small deflections, the output of the detectors was linearly related to the beam deflection. More complete discussions of the characteristics of the detectors are contained in References 38, 39 and 40. The second detector which replaced the knife edge, lens, and photodiode was a linear biaxial photodiode. This change gave the capability to sense the beam deflection in two orthogonal directions. The consequences of this change will be discussed later. (Shortly after the biaxial detectors were obtained, Ballantyne and Bray (50) reported their use in a slightly different manner in a combustion study.)

The detectors were affixed to mill tables supported as described for the laser mounts. This combination allowed the lasers to be positioned to study any point of the flame and the detector to be precisely positioned relative to the laser beam with no relative motion between the laser and the detector. Any relative motion between the laser and the detector would generate an output signal. It was noted that when

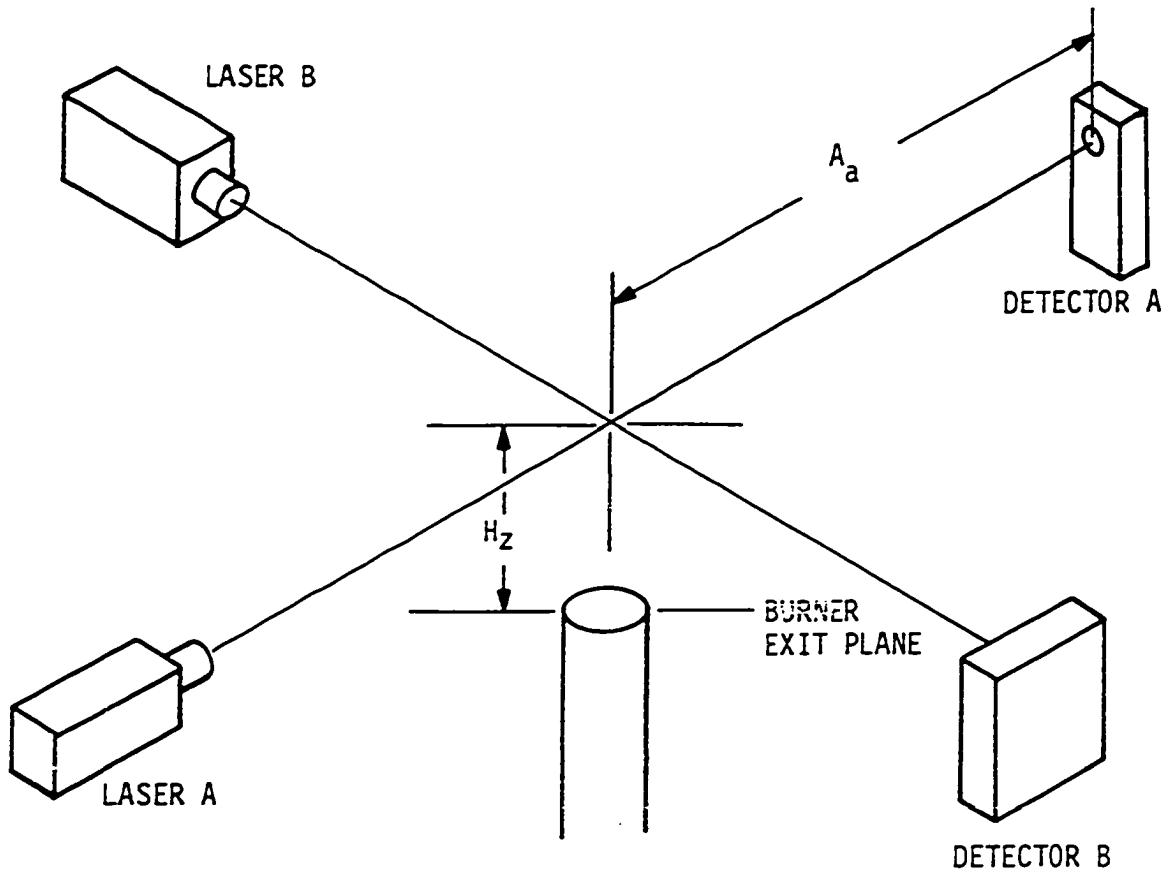


Figure IV-5. Schematic of Crossed-Beam Schlieren System.

the cage was given a sharp rap, an oscillation in the output was observed. The oscillation was rapidly damped out and was not a problem in data acquisition. Since the cage was rigidly mounted to the chamber which was independent of the operating platform, the instrument was independent of movement on the platform.

The flame generated heat at a rate of 40 to 90 kw, depending on approach speed and stoichiometry. Operation long enough to perform on-line data reduction was impractical because of operator discomfort and potential heat damage to the instruments. The output of each assembly was therefore filtered, amplified and recorded on FM tape for later analysis. A block diagram of the data recording system is shown in Figure IV-6.

C. Calibration of Flow System

The rotameter used to monitor the airflow was calibrated by measuring the burner exit plane air speed using a hot wire anemometer. The measured speeds allowed calibration of the rotameter in terms of mass flow as a linear function of flow meter setting. Speed measurements were made at each point of a rectangular grid in the exit plane with spacings of 2.54 mm.

The rotameter used to monitor propane flow was originally designed and calibrated as an oxygen flowmeter. Conversion to propane measurement was determined by allowing for the density difference between oxygen and propane. A short computer program was written to calculate the flowmeter settings, the heat generation rate, and the

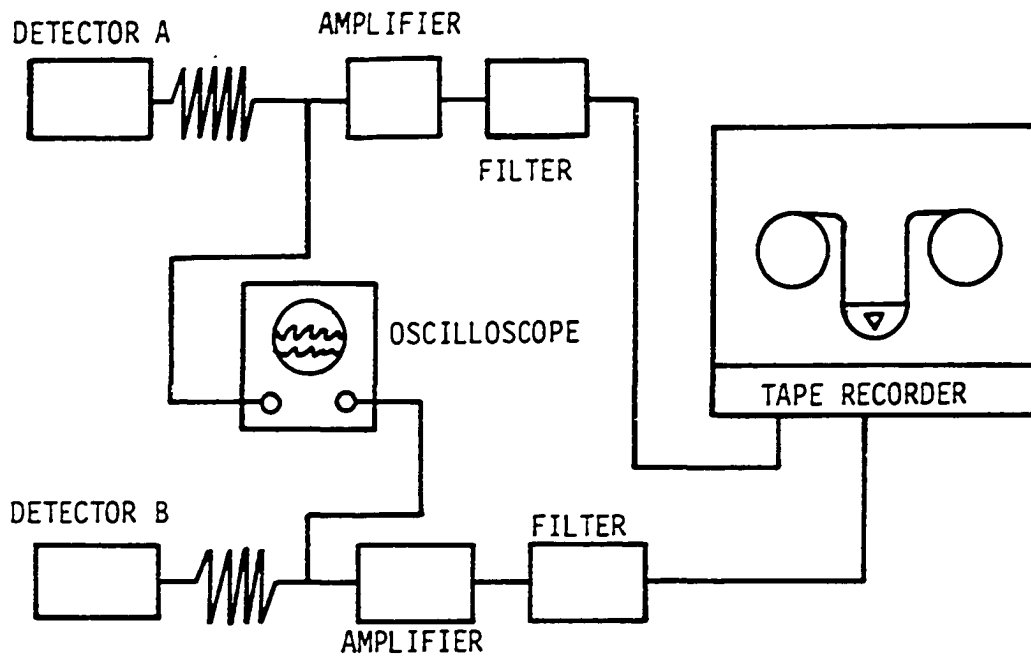


Figure IV-6. Block Diagram of Data Recording System.

Reynolds number based on gas properties and tube diameter for selected exit speeds.

D. Turbulent Flow Field Measurement

Measurements of the flow field velocity were made at the burner exit plane. Figure IV-7 shows the average speed in cm/s and the fluctuating speed in mm/s. The average speed shows a slight asymmetry which is believed to be a result of the entrance effect. The rms fluctuating speed was plotted rather than the normally reported ratio of fluctuating speed divided by mean speed. This was done because the important ratio for flame studies is the ratio of the fluctuating speed divided by the burning speed. The turbulent speed increased in the shear layer and was a minimum in the central region.

Table IV-1 lists some common parameters used to classify turbulent flows for the two mean speeds used. In both cases, the centerline root mean square fluctuating speed was less than the laminar burning speed. The microscale (λ_g) is a measure of the size of the eddies responsible for dissipation in the flow. The integral scale is a measure of the largest eddies in the flow. These two scales are comparable and were much larger than the flame thickness.

The turbulent velocity energy spectrum for the 4.5 m/s speed case is shown in Figure IV-8. The two straight lines represent the $-5/3$ power law expected in the universal equilibrium range and the -8 power law associated with the filter attenuation slope. The energy spectrum passes continuously through the $-5/3$ slope. The absence of

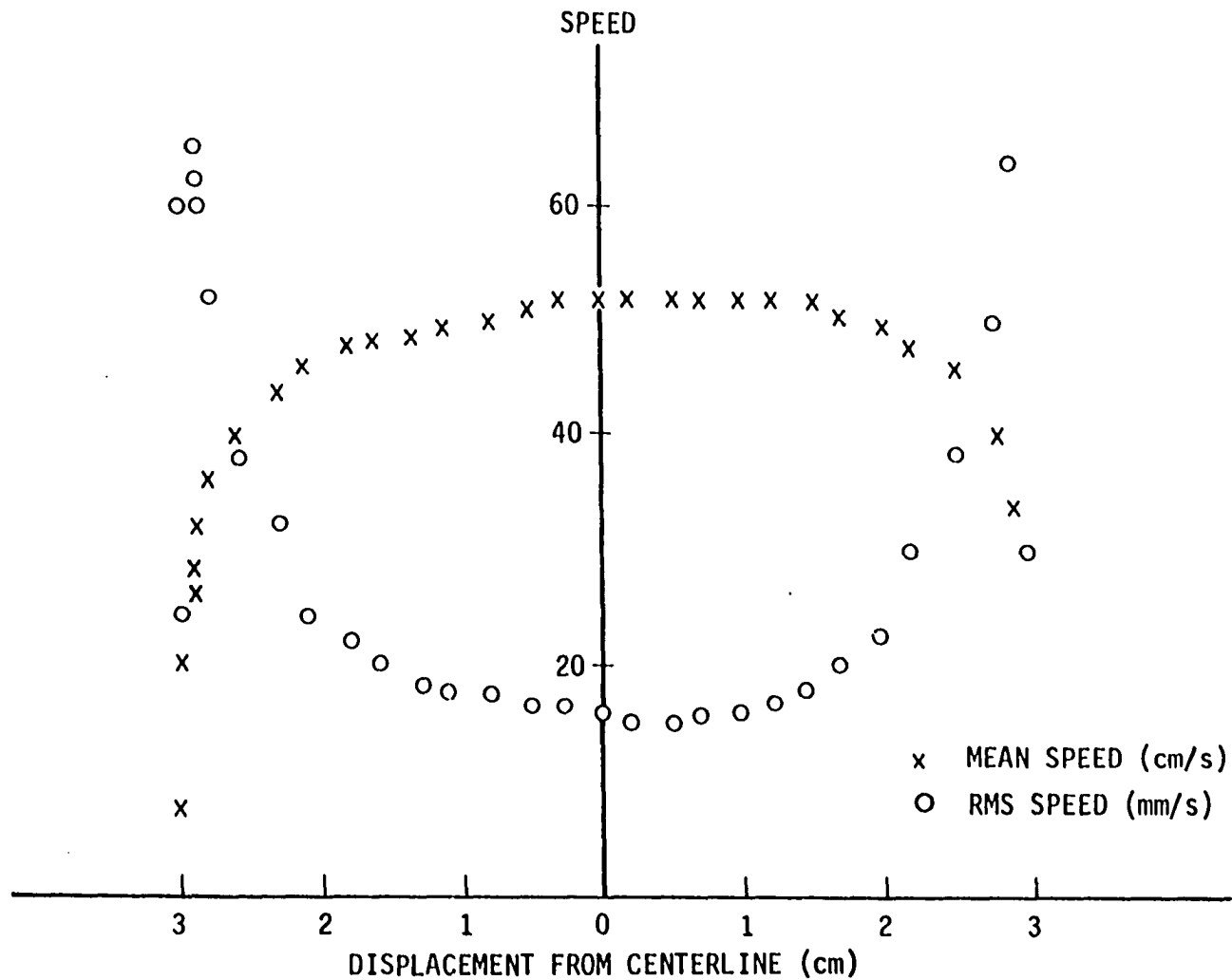


Figure IV-7. Average Speed and Fluctuating Speed at the Burner Exit Plane for the 4.5 m/s Approach Speed Case. Average Speed in cm/s and Fluctuating Speed in mm/s.

Table IV-1. Characteristics of turbulent flow fields

Mean speed m/s	4.5	8.0
Pipe Reynolds number	18200	32300
U' m/s	0.151	0.319
Integral scale mm	7.63	8.65
λ_g mm	3.92	2.48
Dissipation w/kgm	0.35	3.91

the Kolmogorov equilibrium range is expected, based on the scales. For the Kolmogorov equilibrium range to exist, the integral scale must be orders of magnitude larger than the microscale. The specimen, Figure IV-8, shows that there are no dominant frequencies in the turbulence.

E. Instrument Calibration

The power output of the lasers was stable despite many hours of prior use. The total noise was less than the suppliers' specifications. The noise level at 120 hz was about 0.4% in each laser. This 120 hz ripple was a result of voltage rectification in the power supply and was common to both lasers. The cross correlation technique used in analysis emphasized the common signal. Since 120 hz was in the range of frequencies of the data, it was necessary to reduce this specific component of the noise by inserting a 0.5 μ f, 5 kv capacitor in parallel with each laser tube. The capacitors reduced the 120 hz ripple by a factor of eight. Even when correlated, the noise level was at least

ENERGY OF VELOCITY FLUCTUATIONS
(ARBITRARY UNITS, LOG SCALE)

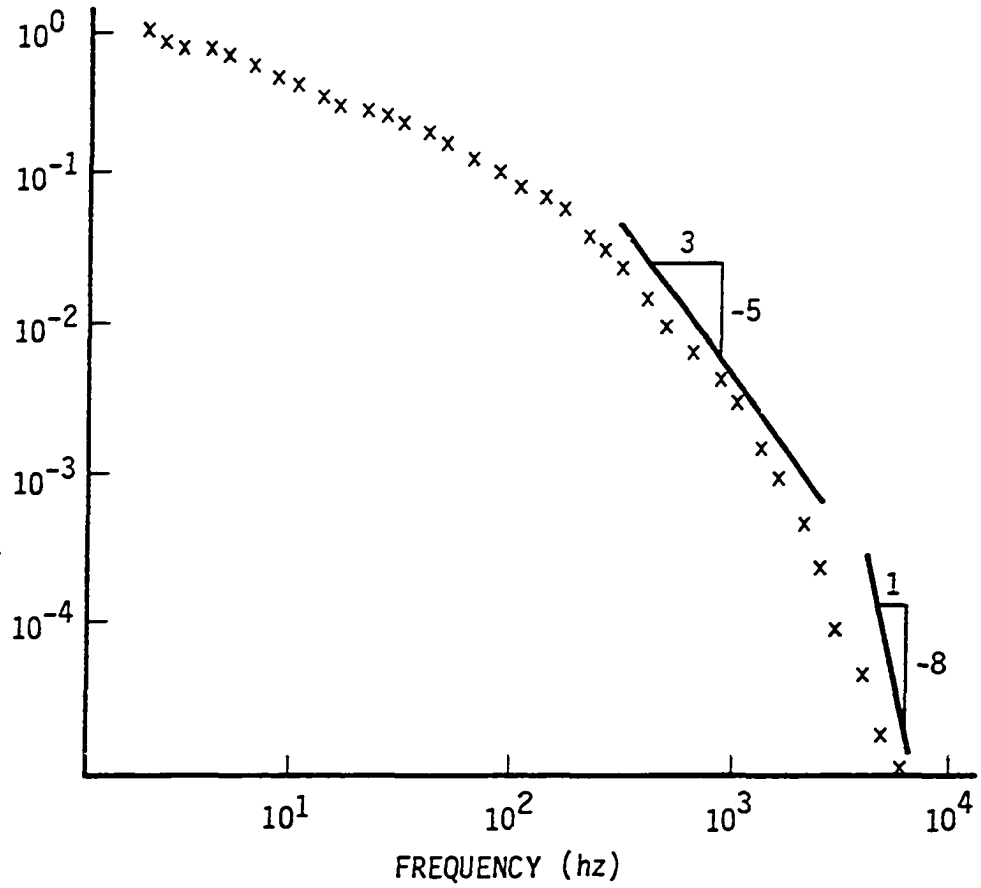


Figure IV-8. Turbulent Velocity Energy Spectrum for the 4.5 m/s Approach Speed as Measured at the Center of the Burner Exit Plane.

an order of magnitude below the measured flame signals.

The laser Schlieren system was calibrated on the cage used for data acquisition. Each laser was mounted on one side of the cage with the beam horizontal. The detector was mounted across the cage and the laser spot was carefully focused on the photodiode. The mill table was then moved in measured vertical steps beginning with the laser beam completely off the knife edge and continuing until the laser beam was completely intercepted by the knife edge. At each step, the total displacement and detector output were recorded. Since the frequency response of the detectors was at least 1 and probably 2 or more orders of magnitude higher than the maximum anticipated signal frequency, no dynamic response calibration was considered necessary. The calibration was repeated with the knife edge moved closer to the laser. The displacement-detector output data was used to calculate a beam diameter at each knife edge location by assuming a Gaussian intensity distribution in the beams. The diameter was defined as twice the radius to the point at which the intensity had decreased to e^{-2} times the centerline intensity. The sensitivity of the laser Schlieren systems was the slope of the output vs displacement curve at the point $e/e_{\max} = 0.5$ as shown in Figure IV-9 and was determined to be about 1100 v/m. The 40 beam widths for lasers A and B were 1.06 mm and 1.01 mm, respectively, at the intersection of the beams. This gave a sampling volume in the flame of slightly less than 10^{-3} cc. Due to the individual displacements of the beams and the spreading of the beams by the flame, the actual sampling volume could have been somewhat larger than 10^{-3} cc. In the worst imaginable case, the sampling volume is small with

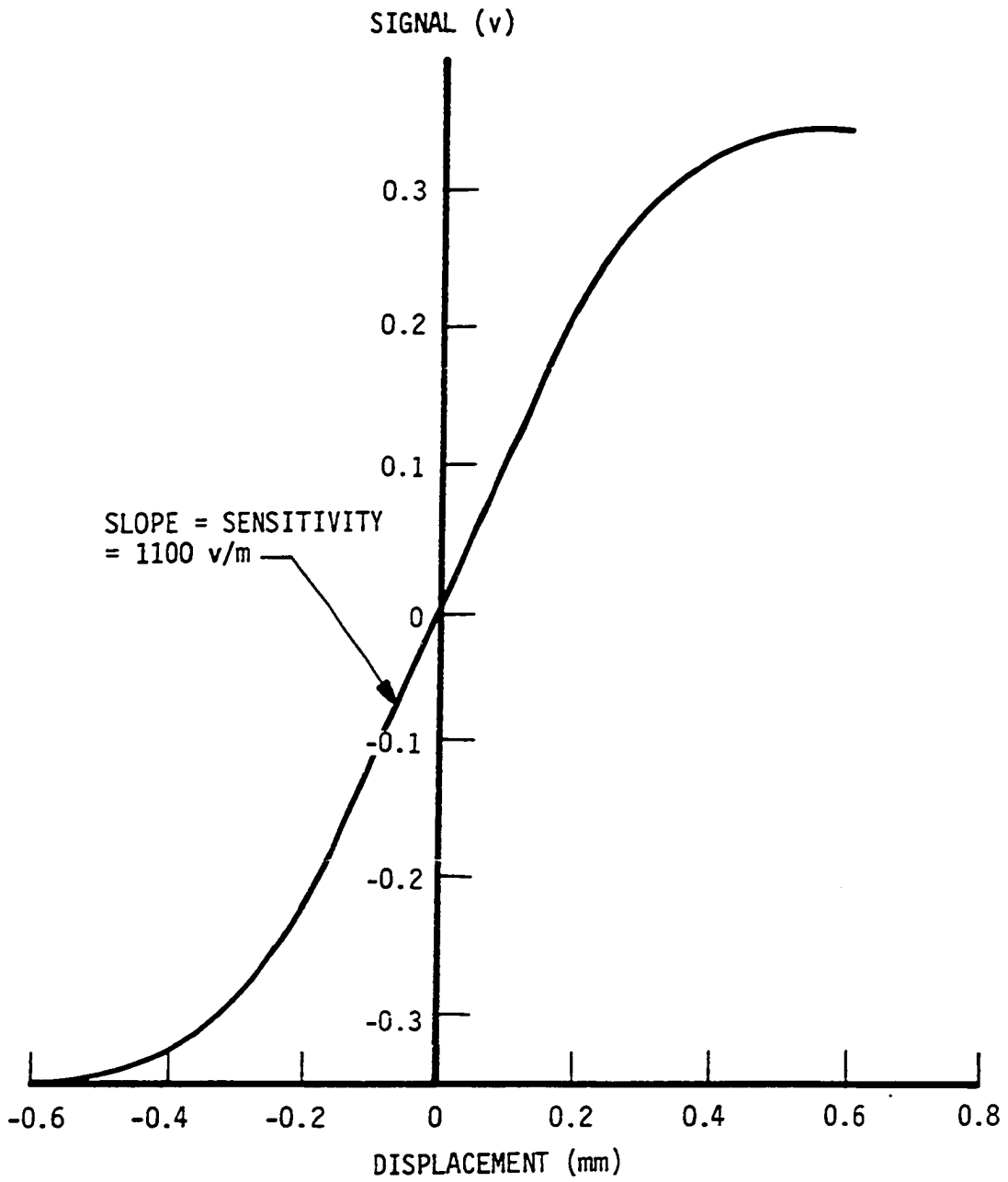


Figure IV-9. Detector Output vs. Displacement Curve with Sensitivity Indicated.

respect to the size of the flame region. The size of the beams is, however, large compared to the flame thickness. Divergences of the undisturbed laser beams were 0.35 m radian and 0.42 m radian, respectively, for lasers A and B. This was less than the supplier specified maximum.

Figure IV-10 is a plot of the output vs displacement data and a measured probability density distribution of a typical flame generated signal. The signal level extends into the nonlinear range of the calibration a significant portion of the time. There is, therefore, no unambiguous relationship between root mean square output and root mean square beam deflection for this case. A second problem resulted from the finite size of the beam. Since the beam size was comparable to the size of some of the disturbances in the flame region, the beam was sometimes distorted in addition to being deflected. This distortion of the beam invalidated the calibration, since the entire beam was displaced for the calibration. If the instrument responds proportional to beam deflection, the rms signal should increase linearly with distance from the flame to the knife edge. A test was done in which the knife edge to flame distance was varied from 12 cm to 40 cm and the root mean square signal level was recorded. The root mean square signal level was relatively independent of distance over this range. This was proof that the distortion effect and the excursions into the nonlinear range were significant. This measurement was supported by the qualitative observation of the laser spot when projected on a wall about 10 m from the flame. In addition to movement of the spot as a whole, which indicates a Schlieren effect, the spot size and shape changed indicating a distortion effect.

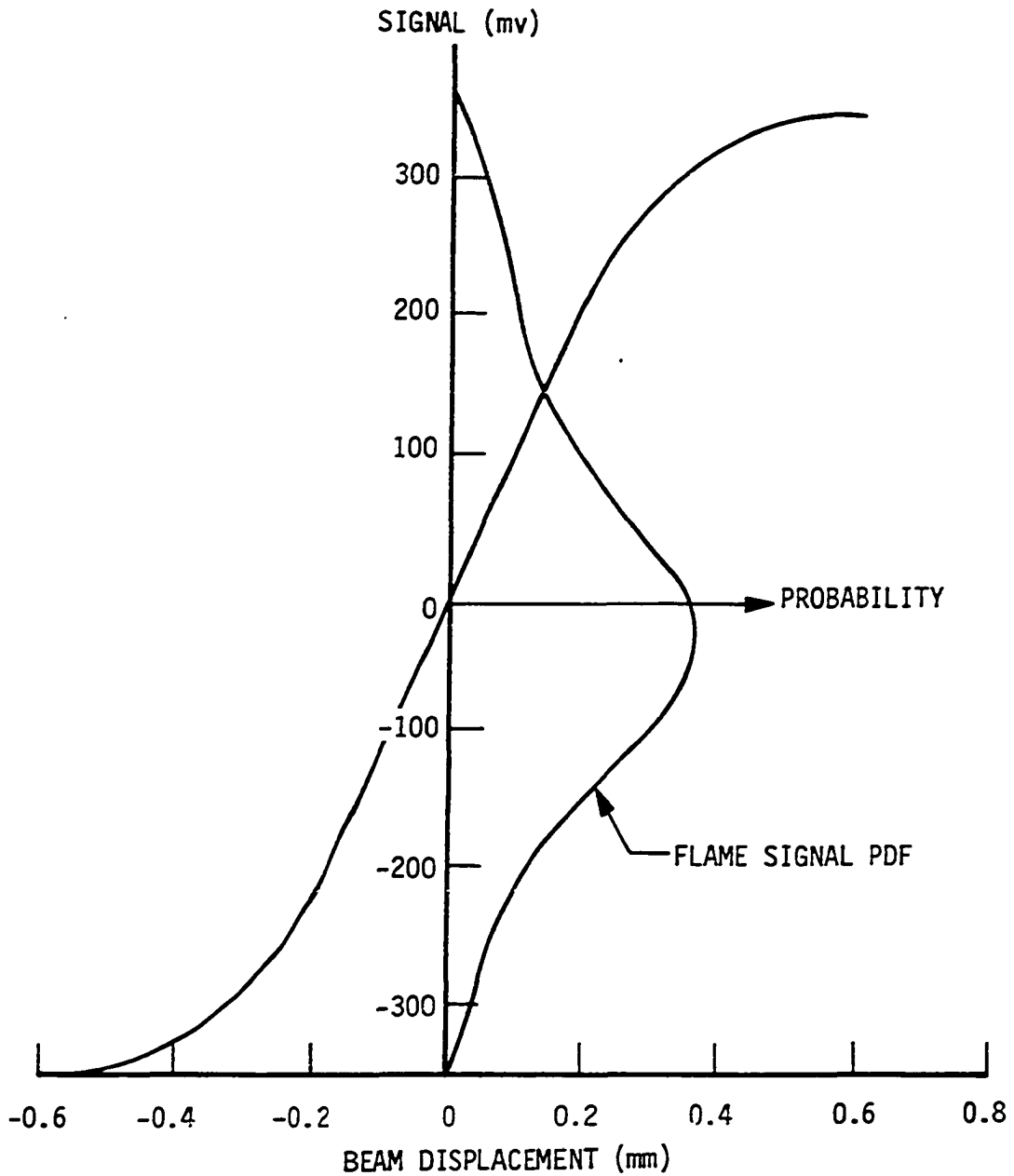


Figure IV-10. Detector Output vs. Displacement Curve and Signal Probability Density Function (PDF) Using the Initial Photodiode and Knife Edge Combination.

Linear biaxial detectors were used to overcome the difficulties with the knife edge and photodiode detectors. These detectors, with proper external circuitry, were sensitive to both the incident light power and the location of the centroid of the light power distribution relative to the crystal center. Each crystal produced two outputs. For clarity, these will be called "vertical output" and "horizontal output." On the crystal face, there were lines along which one output was zero and one output varied with position. The line corresponding to zero horizontal output was called the horizontal axis and the line corresponding to zero vertical output was called the vertical axis. The intersection of the axes was the center of the crystal. The two axes were not precisely orthogonal so the outputs were not entirely independent. With the laser beam centered, the cross sensitivities were at least a factor of ten less than the direct sensitivities so displacement in one direction did not appreciably affect the signal level in the other direction. Since the detectors were always operated with the beam centered on the crystal, the outputs were assumed independent.

Each biaxial crystal had five connectors, a common center connector and one attached to each edge of the crystal face. When the crystals were properly biased, the sum of the two voltages measured at opposite edges was proportional to the total light power incident on the crystal. The difference of the two voltages measured at opposite edges was proportional to the displacement of the centroid of the light intensity distribution relative to the crystal center. The capability to monitor total light power was not used during flame data acquisition in this study.

The lasers could be focused to a point without damaging the conventional photodiodes. The maximum allowable intensity of the biaxial detectors was about a factor of 13 less than the centerline intensity of the laser beams. This required attenuation of the laser beams to prevent damage in the form of a dead spot in the crystal face. Only complete recalibration of the detectors could show the defect but the output could be affected. Extreme caution was required when the biaxial crystals were used.

Numerous beam attenuators were tried including partially silvered mirrors, exposed film, sunglass lens, and variable polarizers. All attenuators provided a beam which was safe for the biaxial crystals. Only the variable polarizers provided continuously variable attenuation. Since the sensitivity of the detectors was a function of light power, the maximum safe beam power was desired. For this reason, the variable polarizers were used. All attenuators checked increased the beam diameter and beam divergence. The beam diameters and divergences were measured with the polarizers set for the biaxial crystals. The beam diameters (4 σ width) were 1.68 mm and 1.76 mm for lasers A and B. The beam divergences were 1.55 m radian and 1.75 m radian, respectively. The polarizers, therefore, increased the beam size about 60% and the divergences about 400% as compared with the unattenuated beams. The minimum sampling volume in the flame region was about four times the minimum for the unattenuated beams.

The calibration of the biaxial detectors was performed in the same fashion as the calibration of the photodiodes. Figure IV-11 gives the dimensions of the active area of the crystals. The lines

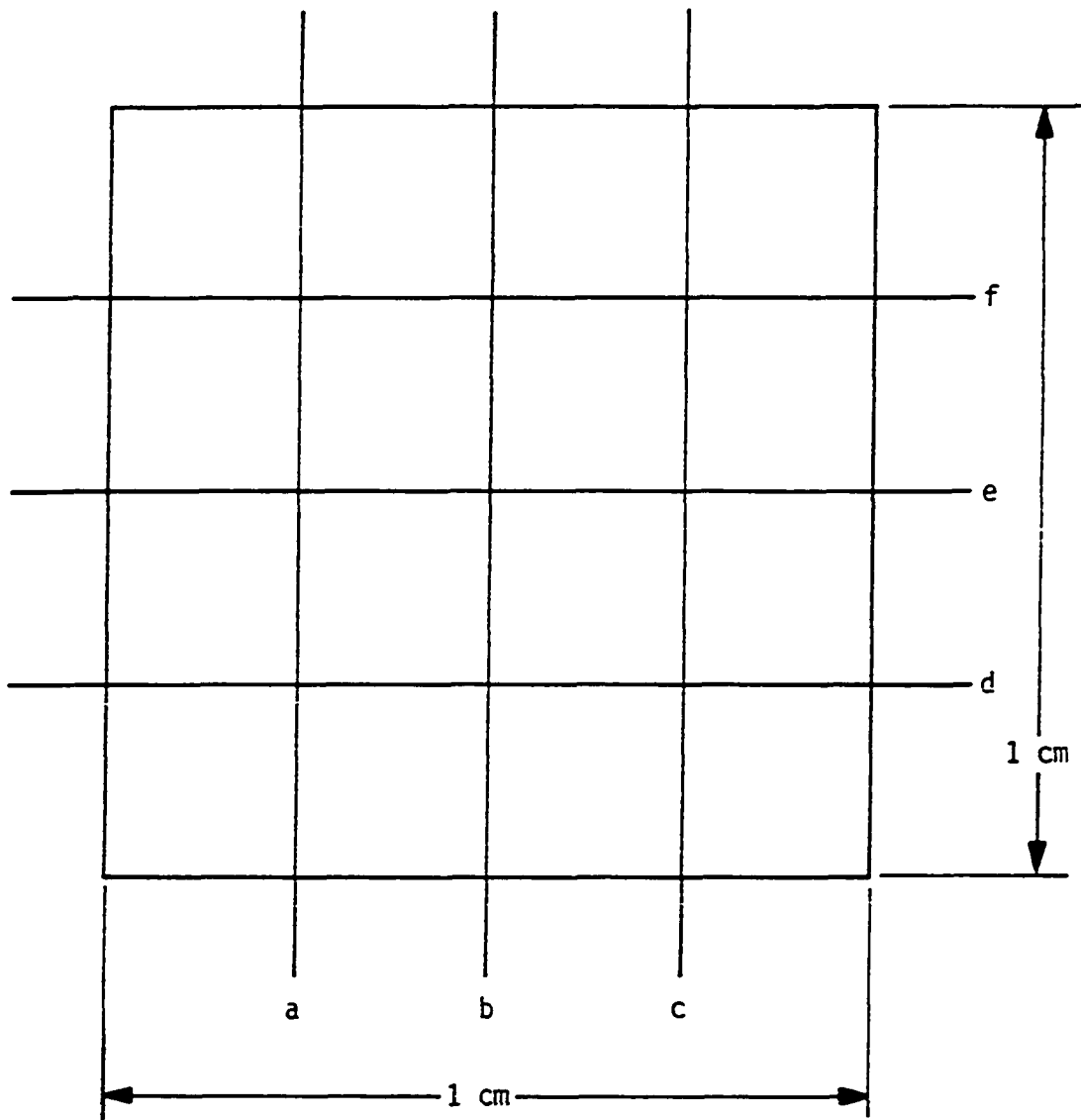


Figure IV-11. Dimensions of Biaxial Detectors and Locations of Calibration Paths.

labeled a through f denote the path of the centroid of the laser beam for the various steps of the calibration. A calibration along line b is shown in Figure IV-12. Additional traverses were made along line b with the laser intensity reduced and full battery voltage and with full intensity and reduced battery voltage. In both cases, the output level was reduced but linearity was preserved. Since the output level could change as battery voltage changed or if the beam attenuation was changed, a simple calibration check was done each time data were taken. The procedure consisted of aligning the crystal zero horizontal output axis vertically and moving the laser beam 1.27 mm. The resulting output divided by the displacement was used as the sensitivity.

The detrimental effect of the beam distortion effect was greatly reduced by the extended linear range of the biaxial detectors. The detectors allowed simultaneous observation of the beam deflection in two directions normal to the beam. The total beam deflection could be determined from the individual components. The importance of this will be discussed in later sections.

The root mean square detector output as a function of distance was checked using the same range of flame to detector distances as was used to test the photodiodes. The output of the detectors was linear over the range. This was proof that the detectors were sensitive to beam deflections and insensitive to beam distortion.

Shown in Figure IV-13 is the calibration curve of a biaxial detector and the probability density distribution of a typical flame generated signal. No signal approaches the limits of the linear range

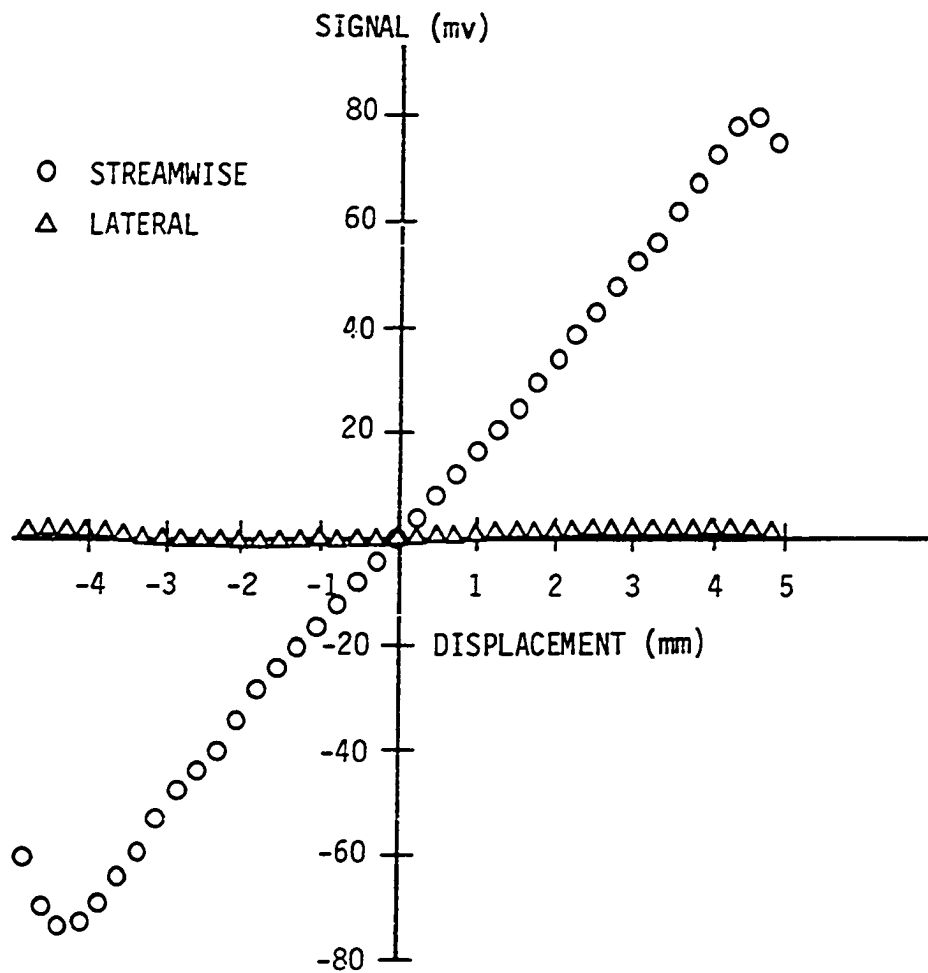


Figure IV-12. Output vs. Displacement (or Calibration Plot) for Biaxial Detector.

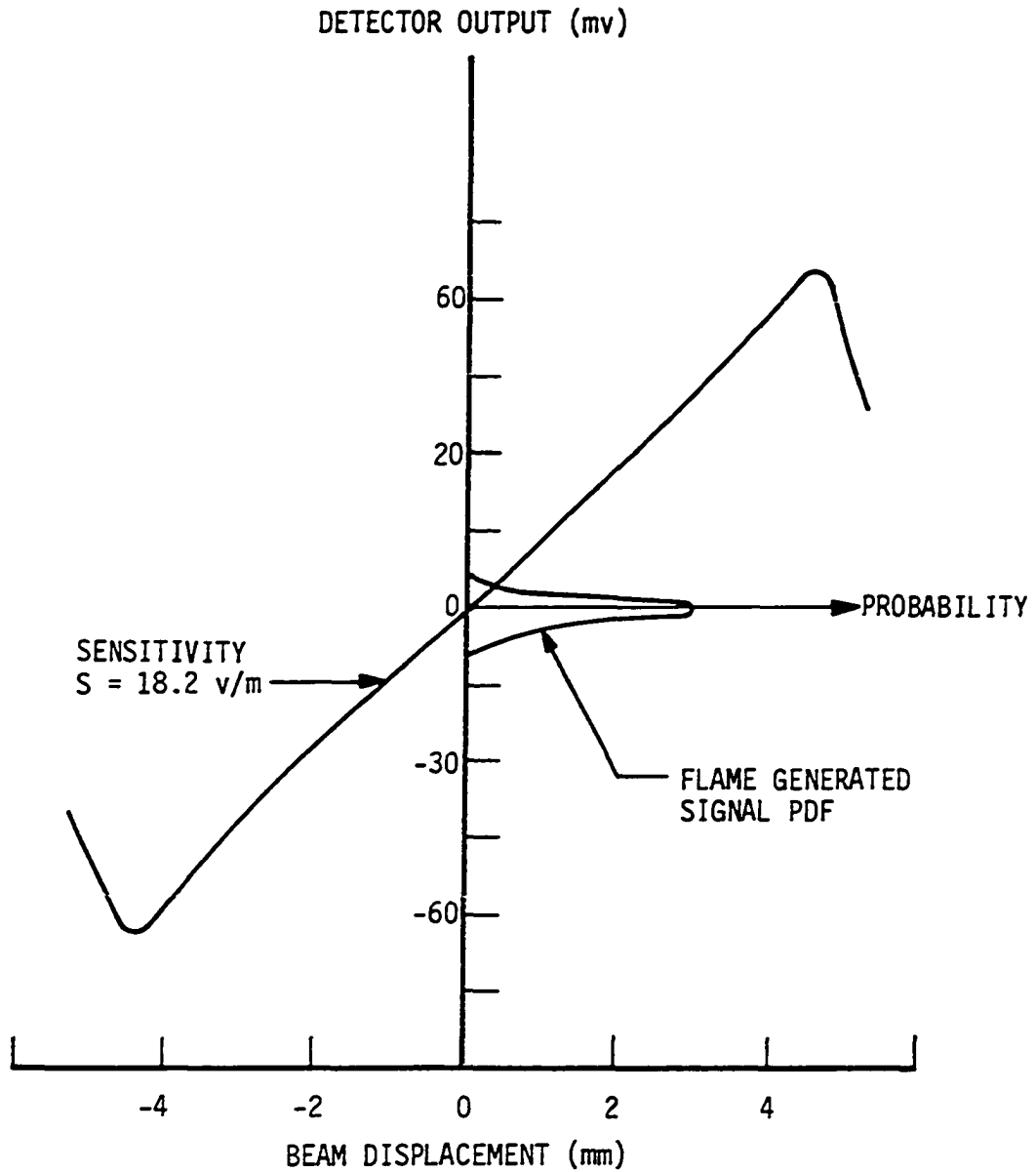


Figure IV-13. Output vs. Displacement for Biaxial Detectors and Probability Density Function (PDF) of Flame Generated Signal for 4.5 m/s Approach Speed Flame.

of the detector. Signal levels and beam deflections are simply related in this case. This was necessary for the subsequent analysis.

F. Data Acquisition System

The individual assemblies of the data acquisition system were labeled A and B so consistency could be maintained. A block diagram of the system is shown in Figure IV-14. The output of the detector circuit was amplified, filtered, and recorded on FM tape. The filters were set and the amplifiers were adjusted to approach saturation of the tape input. Most data recorded were filtered to reject all frequencies below 25 HZ. For selected cases, the filters were set to pass all signals above 2 HZ. The output of the detectors was displayed on a storage oscilloscope and photographs were made when the characteristics of individual traces were studied. Examples of these traces and their significance are discussed in later sections.

The primary data reduction instrument was the Saicor SAI 42 probability analyzer and correlator. Two channels of analog signals were input to the instrument. These were converted to digital form, then at the operator option, either auto correlation, cross correlation, or probability analysis was performed.

The majority of the equipment used in this study was identical to that used by Martin (39). The laser power filters previously described, the biaxial detectors, and the FM tape recorder were the new additions for this study. Each of these components was checked and found to add no unacceptable uncertainty due to instrument noise.

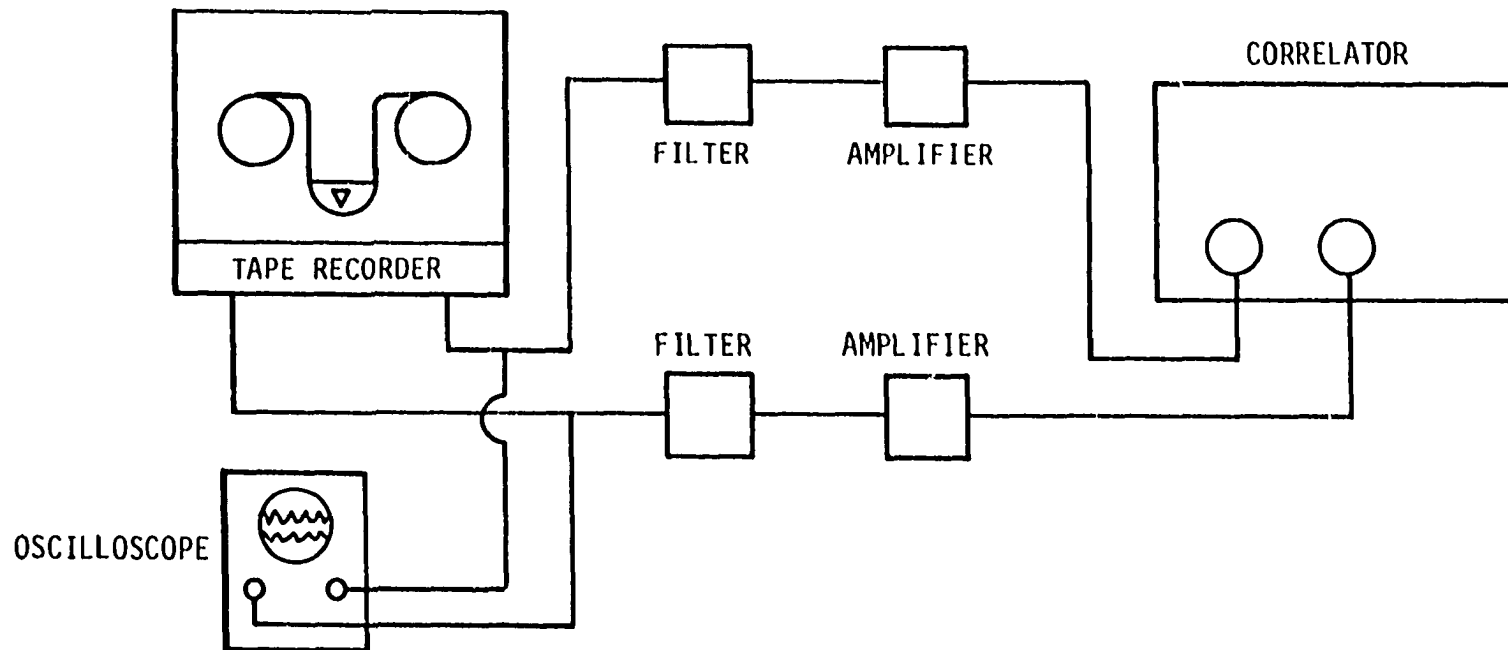


Figure IV-14. Block Diagram of Data Analysis System.

The levels of the signals in this case were significantly higher than those observed by Martin and instrument noise was not a significant problem.

V. RESULTS

A. Preliminary Results

1. Convection speed

The convection speed, U_c , was the most probable speed, in the streamwise direction, of the disturbances in the flame which cause a signal. This speed was used extensively in the data reduction. Since it gave some information about the flame, it was of interest on its own merit. The convection speed in the flame was determined from cross covariance of the signals produced when beam B was displaced a distance Δz in the streamwise direction from beam A as shown in Figure V-1.

If the signal producing disturbances were convected from beam A to beam B, signal B would have more in common with signal A at some prior time than it had with signal A at time t . Since the covariance is a measure of the commonality of two signals, the displacement of the peak of the covariance from zero was the most probable time for disturbances to be convected from one beam to the other. Most disturbances which produce a signal in one beam do not produce a signal in the other beam. Long averaging times were required to obtain a well-defined peak, since the level of covariance was low. Figure V-2 is a plot of a typical covariance obtained using a five-minute average. The approach speed was 4.5 m/s and the beams were positioned at 0.14 m and 0.16 m above the burner exit. The unfiltered signals were used for calculation of the convection speed. The reasons will be given in Section V-C. For a large number of samples, the mean displacement of the peak was 3.33 ms giving a convection speed of 6 m/s. For the

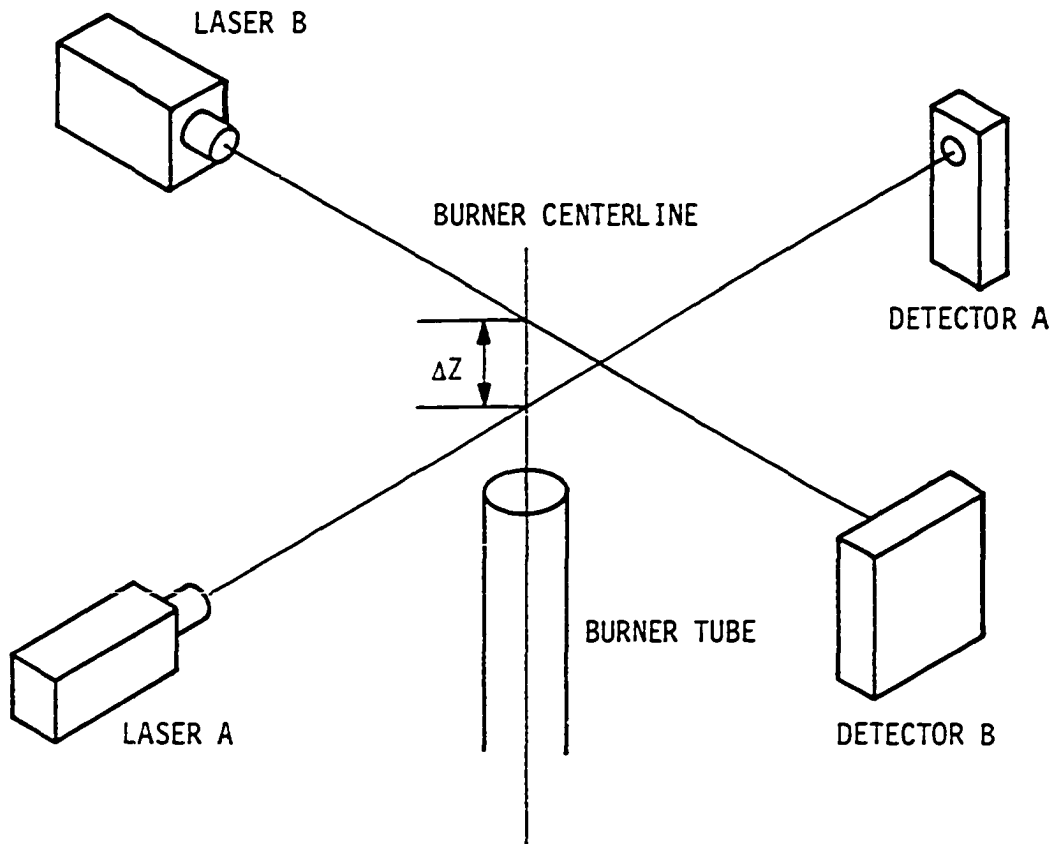


Figure V-1. Schematic Representation of the Experimental Arrangement for Determining Convection Speed.

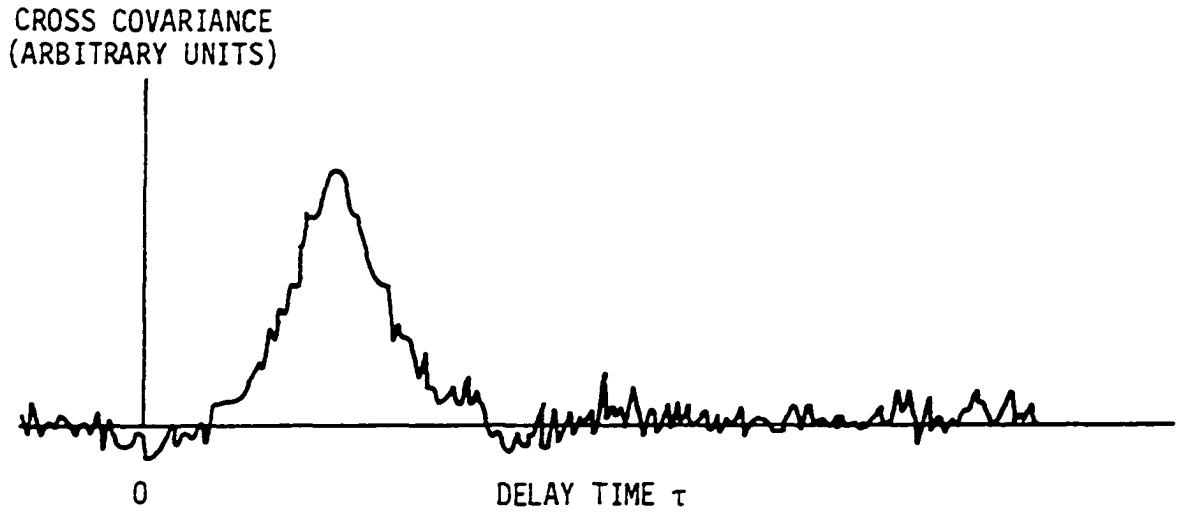


Figure V-2. Cross Covariance Plot Typical of the Plots Used to Determine Convection Speed.

8 m/s approach speed, heights of 0.18 m and 0.21 m above the exit were used. The average displacement of the peak observed was 3.09 ms giving a convection speed of 9.72 m/s. The convection speed exceeds the approach speed due to the expansion which accompanies the combustion and due to the buoyancy of the hot combustion products. This increase cannot be predicted accurately so the convection speeds must be measured. The convection speed was about 33% and 21% greater than the approach speed for the 4.5 m/s and 6 m/s approach speeds, respectively. These values were measured on the centerline of the burner in the active region of the flame and were assumed to be the same throughout the flame.

2. Signal spectra

The first step in the data analysis was the determination of the spectra of the flame generated signals. These spectra could have been obtained by a Fourier transform of the auto and cross correlations. However, results of the transformation are sensitive to the detailed shape of the covariance. The correlograms have inherent statistical uncertainties and their transforms can have large uncertainties, particularly at high frequencies. To circumvent this, the individual signals were bandpass filtered at one-tenth decade increments before they were correlated. The covariances were corrected for the insertion losses of the filters and were divided by the effective bandwidth of the filters. The results were the energy of the signal per unit frequency averaged over the filter bandwidth. The Fourier transform produces a signal energy content per unit frequency

at each frequency. The two techniques are equivalent in this respect if the center frequency of the filter bandwidth is assumed to represent the entire frequency band. The resulting measured spectra for the case $U = 4.5$ m/s are shown in Figure V-3. Two distinct peaks at about 10 Hz and 200 Hz are apparent in all three sets of data. It was determined early in the study that the low frequency peak was due to a large-scale instability causing a billowing of the air at the periphery of the flame. It was not related to the combustion process in the flow. The majority of the data was recorded with the filters set to eliminate the low frequency peak. The spectra of the same signal sample with the 10 Hz peak eliminated are shown in Figure V-4-A. A similar spectra is shown for the 8 m/s approach speed in Figure V-4-B. The levels of the two auto covariances in each plot are comparable. The level of the cross covariance is substantially less at all frequencies. This difference means that the two signals, A and B, were nearly independent. Physically, this means that most of the disturbances which generate a signal in one assembly did not generate a signal in the other assembly. The spectra of the cross covariance from Figures V-4-A and V-4-B are replotted in Figure V-5. The levels of the two sets of points are comparable, but the shapes are slightly different and the maximum frequencies at which cross covariances were obtained are different. To remove the effect of different convection speeds, the signals were transformed to the wavenumber (κ) domain.

Recall

$$U_c = f\lambda \quad (V-1)$$

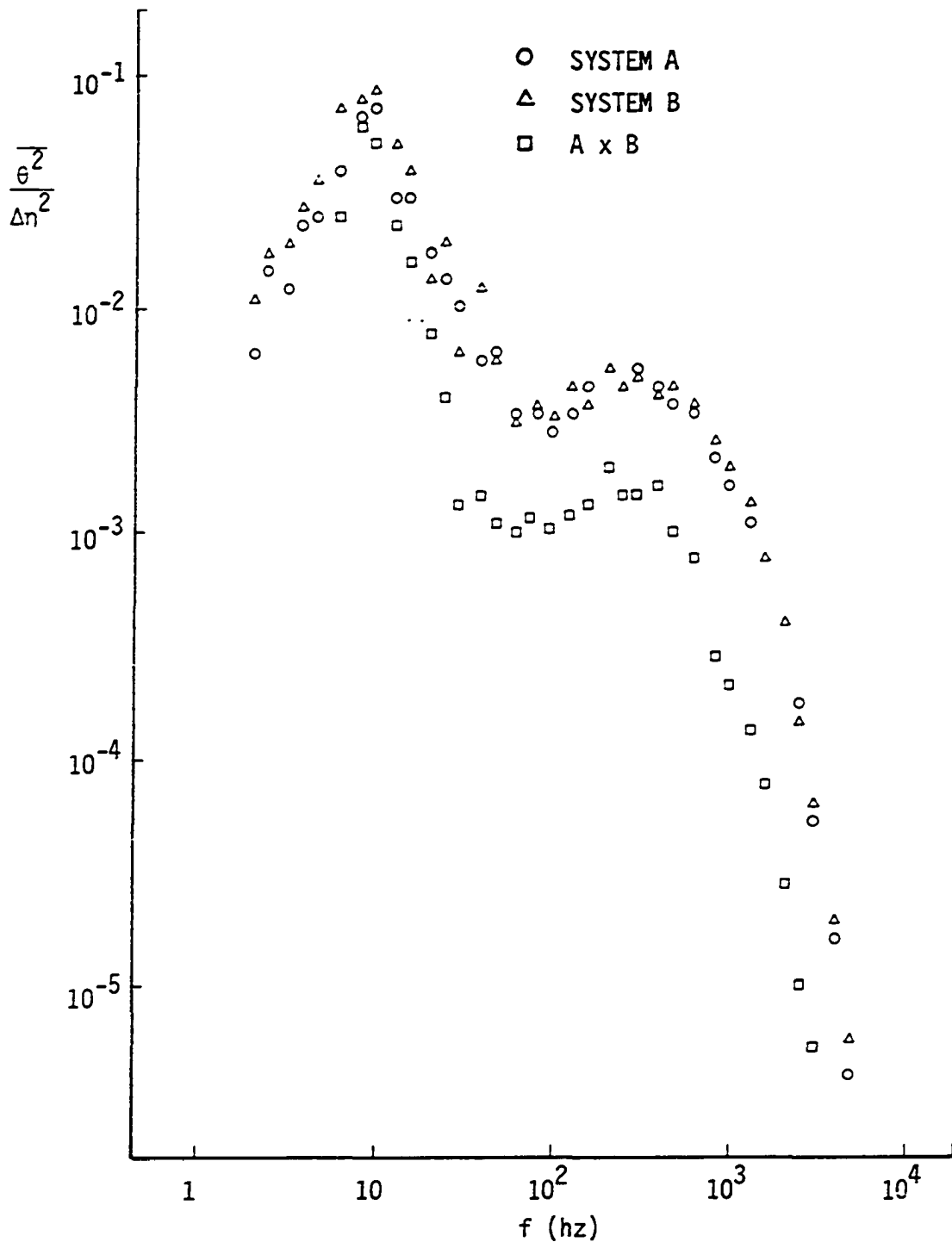
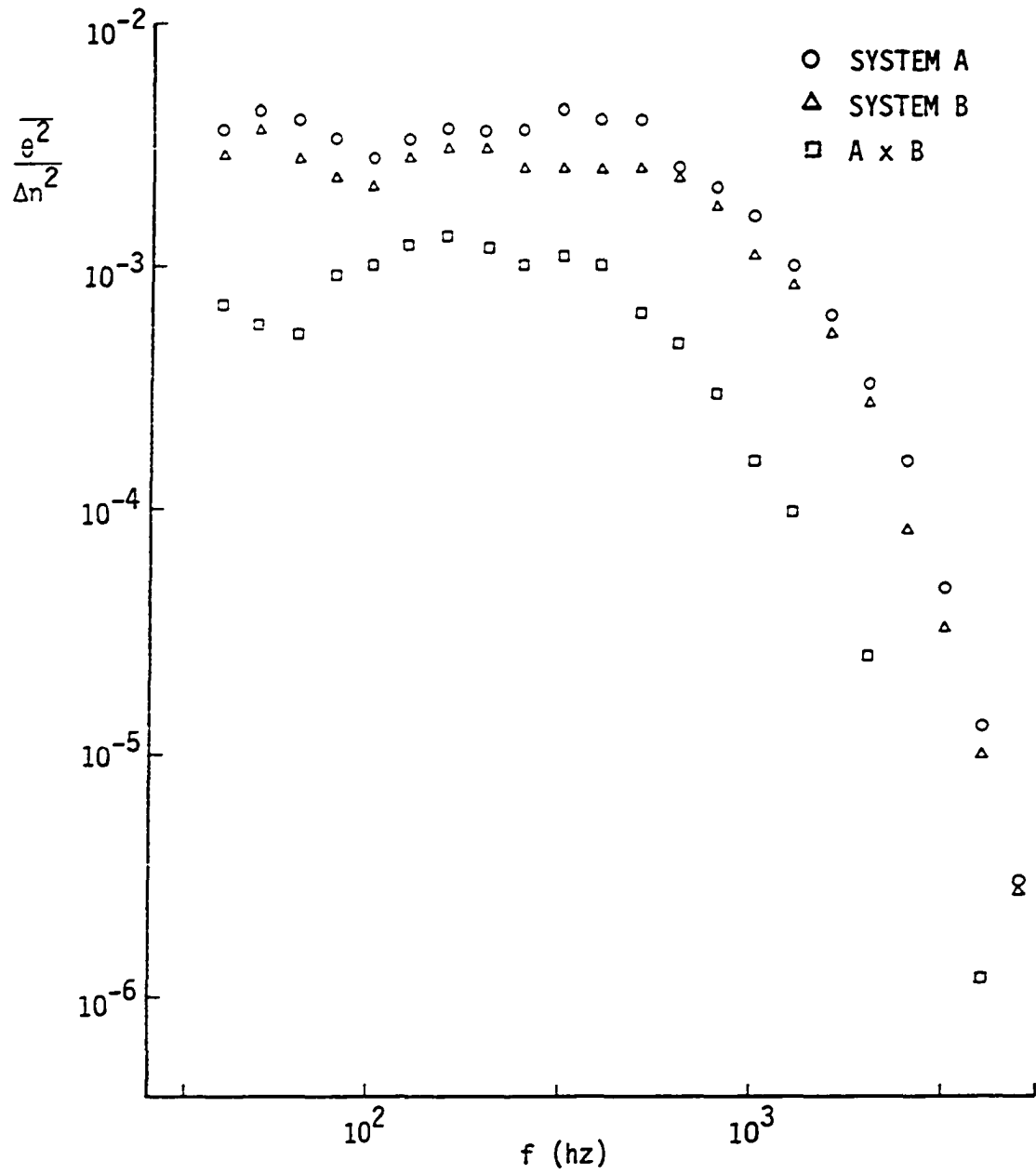


Figure V-3. Energy Frequency Spectra of the Flame Generated Signal Measured on the Burner Centerline 0.14 m Above the Exit for the 4.5 m/s Approach Flame. All Flame Generated Signal Frequencies Retained.



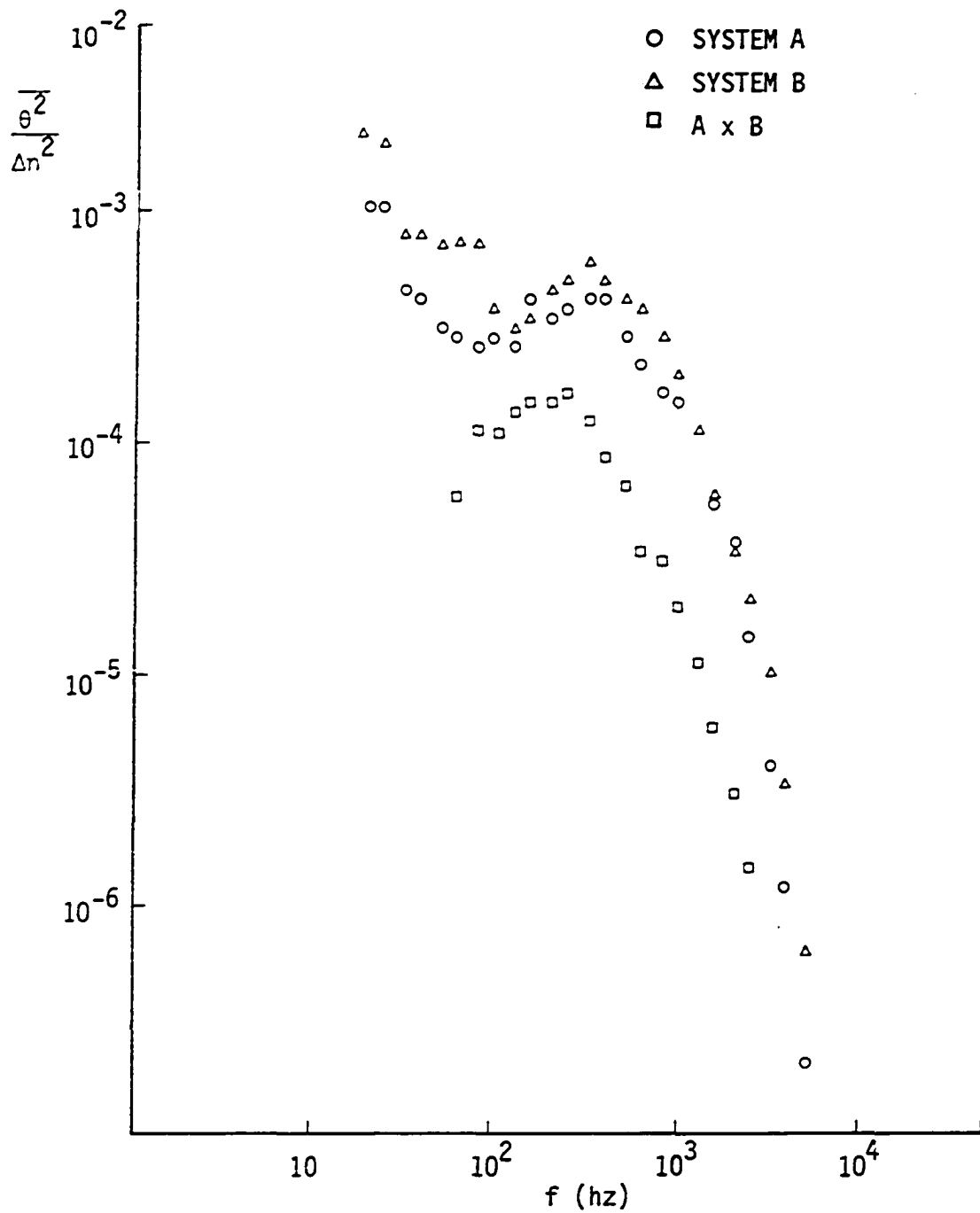


Figure V-4-B. Energy Spectrum of the Flame Generated Signal Measured on the Burner Centerline 0.15 m Above the Exit for the 8 m/s Approach Speed Flame with Frequencies Below 30 hz Deleted.

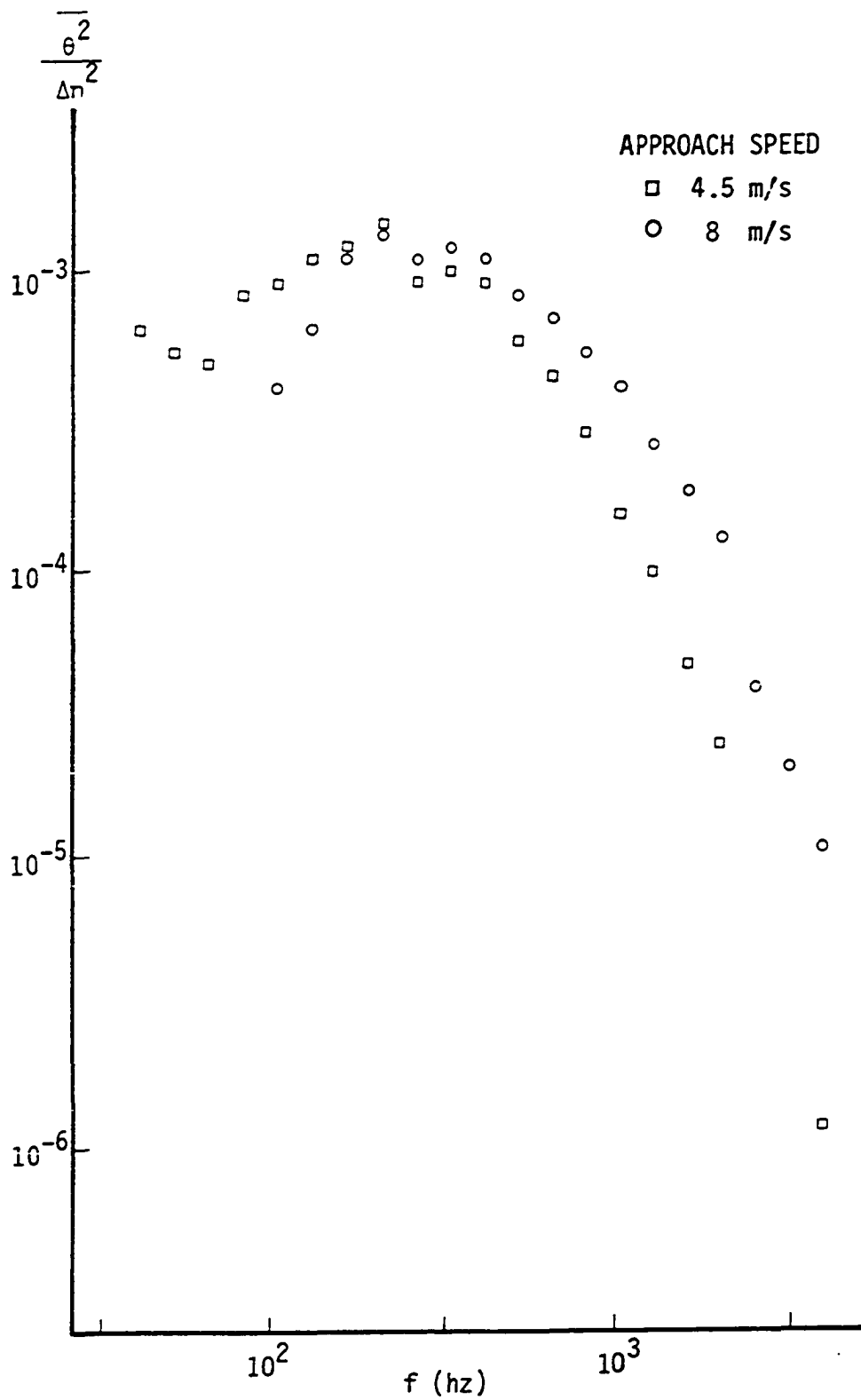


Figure V-5. Cross Covariances from Figures V-4-A and V-4-B.

where f is the frequency and λ is the wavelength in meters per cycle.

Or

$$U_c = 2\pi f/\kappa \quad (V-2)$$

where κ is the wavenumber

$$G(f) df = G(\kappa) d\kappa$$

Thus

$$G(\kappa) = G(f) \left| \frac{df}{d\kappa} \right| \quad (V-3)$$

$$\left| \frac{df}{d\kappa} \right| = \frac{U_c}{2\pi}$$

$$G(\kappa) = G(f) U_c / 2\pi \quad (V-4)$$

The factor $U_c/2\pi$ is 0.95 for the 4.5 m/s approach speed flame and 1.55 for the 8 m/s approach speed flame.

By plotting energy vs κ , the data for the most active regions of the two flames almost collapse to a single line. This agreement indicates that the signals are independent of the convection speed. They are the result of some common occurrence in the two flames. The common occurrence is the combustion process. The decay slopes of the two sets of data are similar, and the magnitudes differ by less than 60%. The most detailed analysis was done on the 4.5 m/s flame and the conclusions were checked on the 8 m/s flame. Extended observations of the 8 m/s flame were not made due to the increased heat generation rate.

Figure V-6A and B are summary plots of the energy vs f for the two

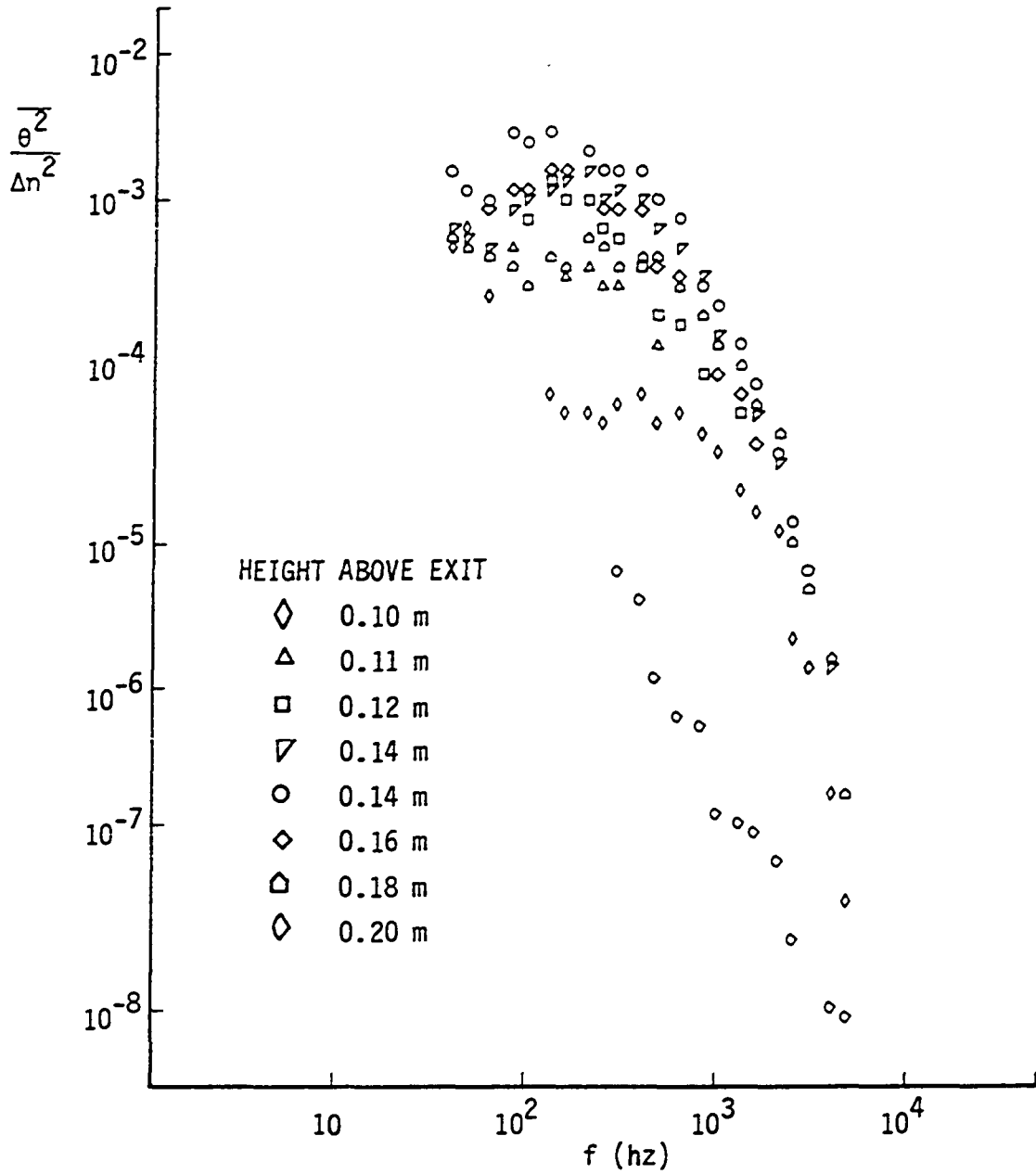


Figure V-6-A. Summary Plot of the Flame Signal Energy Spectra for the 4.5 m/s Approach Speed with Frequencies Below 30 hz Deleted.

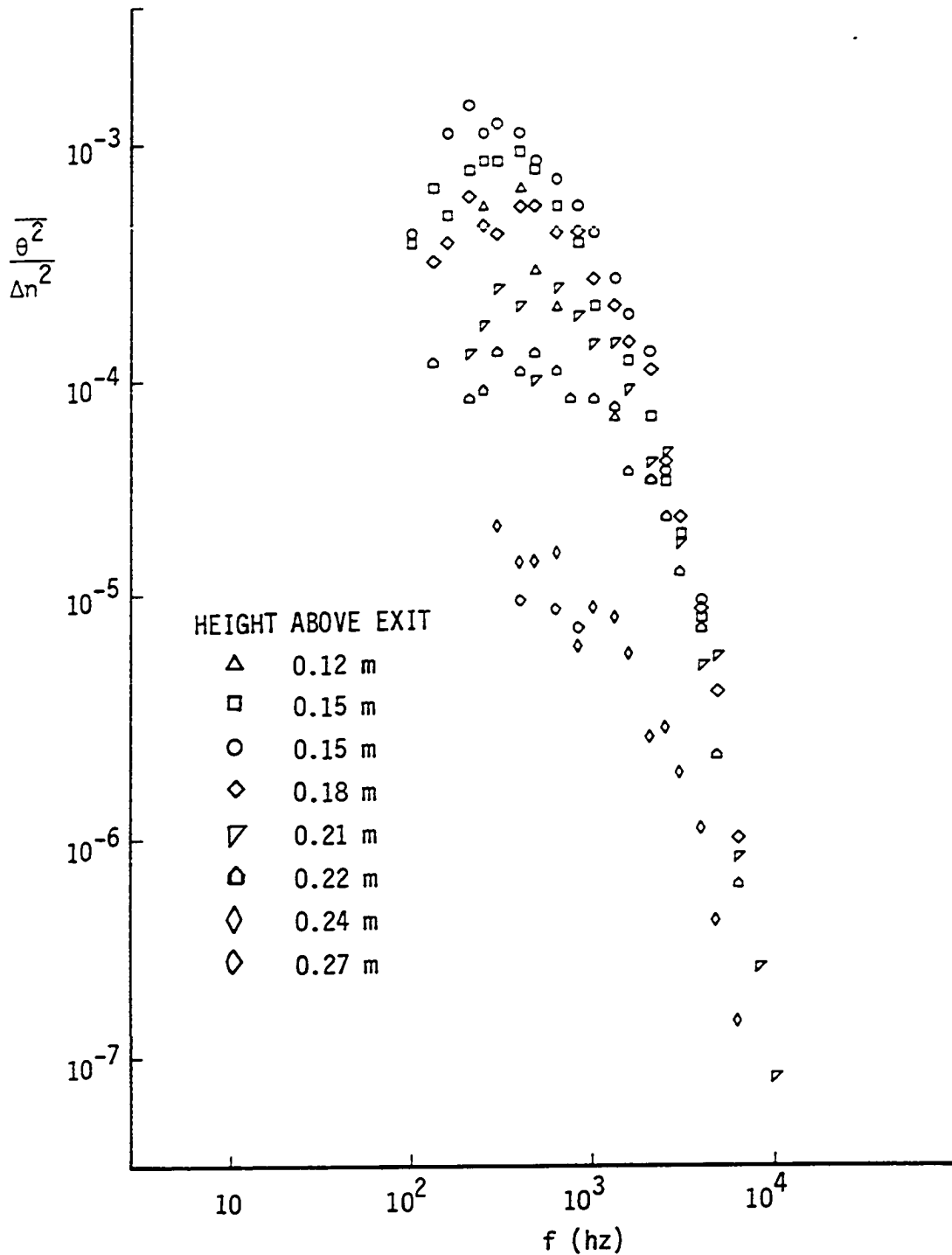


Figure V-6-B. Summary Plot of the Flame Signal Energy Spectra for the 8 m/s Approach Speed with Frequencies Below 30 hz Deleted.

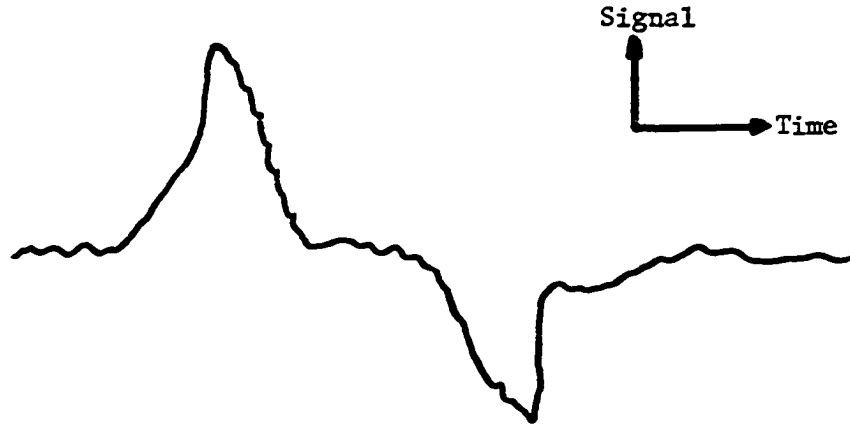
flames for the heights where measurable cross covariances could be obtained. The difference between the lowest elevation at which a cross covariance could be measured and the highest elevation where a covariance could be measured divided by the convection speed was a representative total burning time of fuel within the flame. The measured burning times of the two flames are 16.7 ms and 15.4 ms for the 4.5 m/s flame and the 8 m/s flame, respectively. The step sizes between measurement points in the flames are about 20% of the total variation, so the observed burning times for the two speeds agree within the accuracy of the measurement. The convection speed was the dominating speed in determination of the flame size but was not the only relevant speed. Without proposing any form of the dependence, the flame size can also be expected to be a function of the turbulent fluctuating speed and the laminar flame speed.

The levels of the signals in Figure V-6 build from the lowest height reaching a maximum at about 0.14 m in the 4.5 m/s flame and 0.15 m in the 8 m/s flame. From the maximum, the level decays until virtually no signal remains. This characteristic provides a natural method of dividing the flame. The region below the maximum was the growth region; the region above was the decay region. The flames will be discussed in terms of these two regions.

B. Reaction Zone Modeling

1. Signal shape observations

An effort was initiated to relate the signals directly to a flame process. After some time it was obvious that the most commonly observed signals exhibited spikes as shown in the following sketch.



The duration of the spikes was always much less than the time between successive spikes. The signals were usually much too active to observe a single signal as depicted above but at the infrequent times of low signal level, the signal shape was observed. With this knowledge, it was often possible to view the signal as the sum of several overlapping single signals of varying sizes. The same type signals were observed in the output of both detectors. In rare instances, the assumed basic signal shape occurred simultaneously in both. This indicated that the disturbances which created the signals were roughly symmetric with respect to the burner centerline. The shape of the signals indicated that the changes occurred in a small distance. A search for a

disturbance geometry which could exist in the flame and which was consistent with the observed signals was begun.

2. Flame model development

The constraints on the flame model at the beginning were as follows: The geometry must produce similar signals in both assemblies. The flame model must produce a sharp spike followed by a region of low signal level followed by a sharp spike of opposite sense relative to the first spike. The geometry must be something which could occur in a turbulent flow.

Continuous convoluted flame surfaces were considered and rejected. Continuous flame surfaces could produce the observed signal shapes, but the frequency of occurrence of the signals placed unrealistic constraints on both the shape and motion of the flame front¹. A disperse flame model was sought. The flame front could either be a distorted plane extending over a portion of the flame region or it could be a closed surface. Cross sections of the two cases are shown in Figure V-7. The distorted plane geometry was similar to Damkholer's wrinkled laminar flame. The primary difference was that the wrinkled laminar flame was assumed to be one continuous surface, separating reactants and products of combustion, and the above planar model was assumed to exist as multiple planes in the flame region. These could be visualized as planar fragments of a ruptured flame front. One immediate objection to the planar model was that unless each plane

¹If the biaxial detectors had been available at that time, the process of elimination would have been much easier and more certain. Explanation of this is contained in a succeeding section.

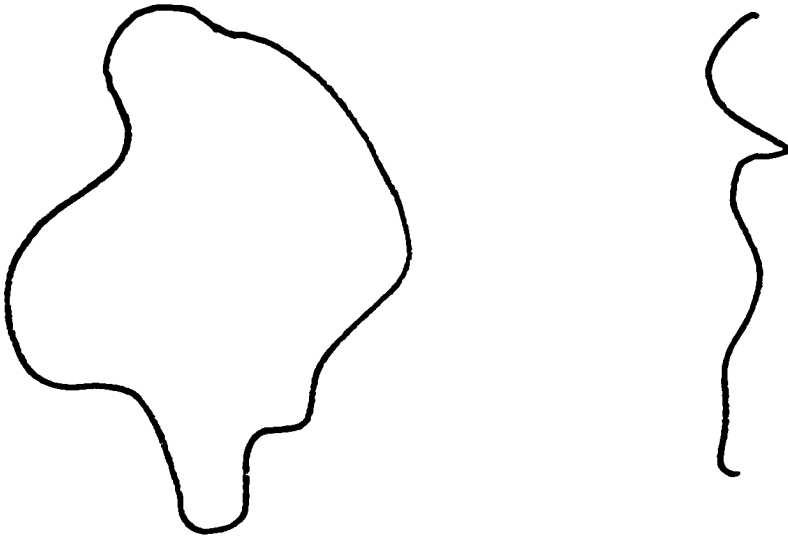


Figure V-7. Schematic representation of two types of disperse flame geometries

spanned the entire region, it must terminate in the reactants. If the planar combustion wave terminates in the reactants, hot products of combustion would be in direct contact with reactants. This was believed unlikely.

The closed surface model was pursued. This surface could enclose reactants and be converging or enclose products and be expanding. A spherical geometry was used to model the closed surface mathematically. The following assumptions were made to simplify the mathematical model: The interior of the sphere was a uniform region of refractive index n_2 . The surface of the sphere was a discontinuity in refractive index. The surroundings of the sphere were uniform with refractive index n_1 . n_1 and n_2 were both approximately 1 and their difference was much less

than one. The beam was square in cross section and was much smaller than the sphere diameter. The beam intensity distribution was uniform.

The assumed geometry with exaggerated beam deflections is shown in Figure V-8. With these restrictions, the signals produced by the detectors is shown in Figure V-9. The entire derivation is reproduced in the Appendix. The mathematical model predicted a signal which was a strong function of the relative sizes of the beam and the sphere. Two equations were required to describe the signal. The first equation predicted the signal when the entire beam was influenced by the sphere and the second equation predicted the signal when only part of the

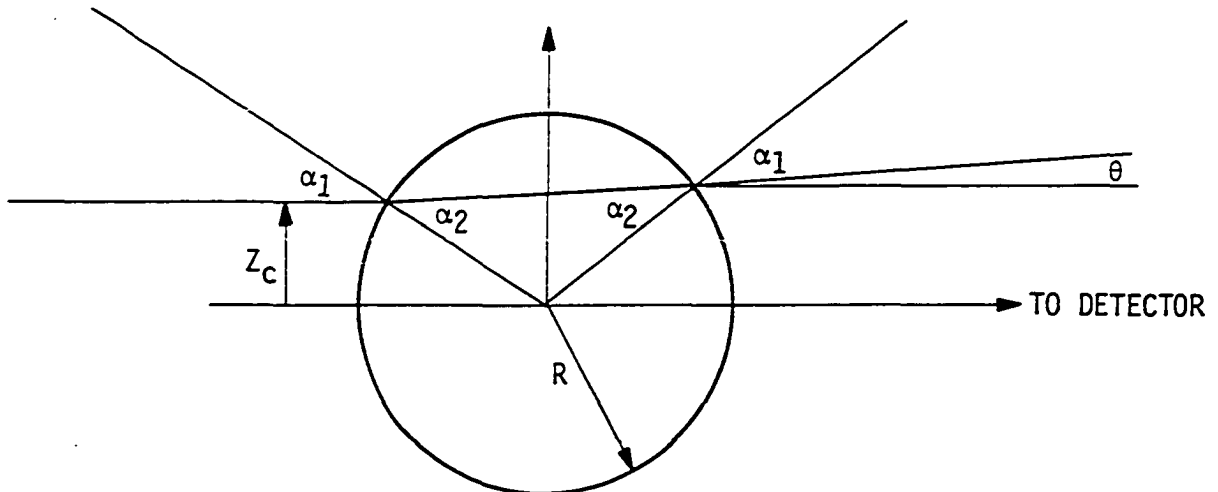


Figure V-8. Spherical Flame Front Geometry with Exaggerated Beam Deflections.

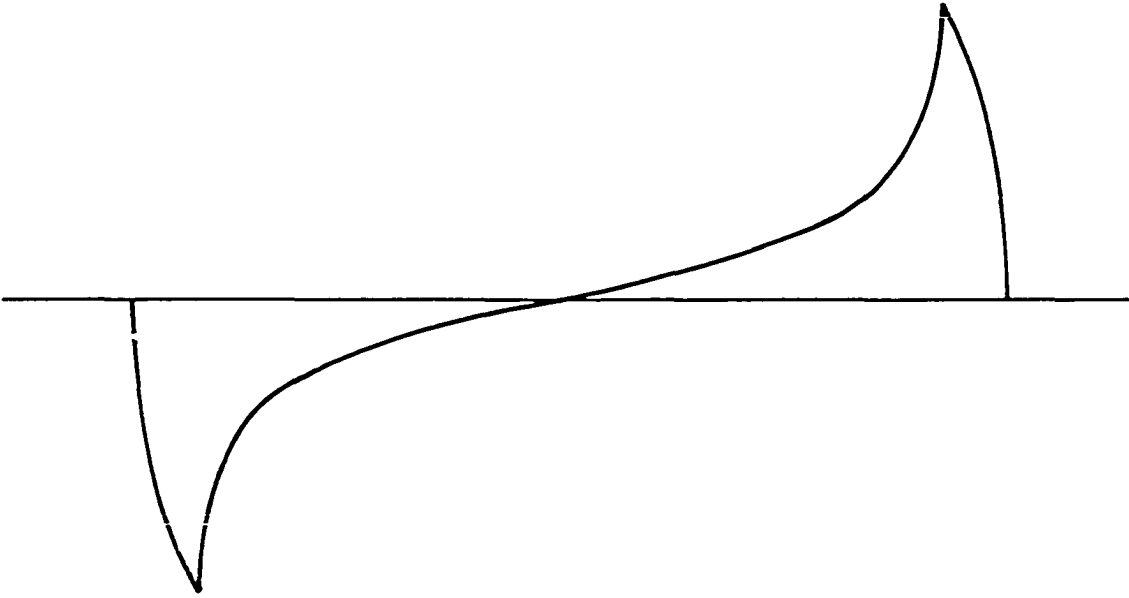


Figure V-9. Signal Shape Predicted by the Mathematical Model.

beam intersected the sphere. The signal predicted was continuous at the juncture where the edge of the beam touched the edge of the sphere. The predicted signal was normalized by dividing by the experimental parameters which determined the signal magnitude and sign. The resulting equations for the simple model were

$$e(z_c)/(SA\Delta n) = \frac{R}{\delta} \left[\left(1 - \left(\frac{z_c}{R} - \frac{\delta}{R}\right)^2\right)^{1/2} - \left(1 - \left(\frac{z_c}{R} + \frac{\delta}{R}\right)^2\right)^{1/2} \right] \quad (V-5-A)$$

$$0 \leq z_c \leq R - \delta$$

$$e(z_c)/(SA\Delta n) = \frac{R}{\delta} \left(1 - \left(\frac{z_c}{R} + \frac{\delta}{R}\right)^2\right)^{1/2} \quad (V-5-B)$$

$$R - \delta \leq z_c \leq R + \delta$$

where R was the radius of the sphere, δ was the effective half width of the beam, z_c was the distance from the beam center to the sphere center, Δn was the change in refractive index, S was the sensitivity of the detector and A was the distance from the burner centerline to the detector. The equations were dimensionless, representing the angular deflection of the beam by a spherical flame volume (or kernel) located at the burner centerline. The product, SA Δn , represents the system specific parameters in the simple model. The ordinates of the plots (Figures V-3 through V-6) were divided by this quantity squared. S and A were easily measured but Δn was calculated, assuming complete reaction. The technique suggested by Weinberg (35) was used to calculate the refractive index of propane. Δn was the refractive index of stoichiometric propane and air evaluated at typical atmospheric temperature and pressure minus the refractive index of nitrogen, water vapor, and carbon dioxide evaluated at the same pressure and at the adiabatic flame temperature. The value of Δn calculated was 0.324 E-03. This value was imprecise because the final temperature was less than the adiabatic flame temperature, and the products of combustion were not as assumed in the ideal case. The use of this value led to no contradictions in subsequent analysis. Information required for a better estimate was not available.

The effective half width of the beam δ was the normalizing parameter for the spherical geometry. A value for δ was required to

determine a simple model signal level for a specified radius, or to determine a physical size for a particular ratio of R/δ . The laser beam used in the experimental apparatus had a two-dimensional Gaussian intensity distribution. The beam assumed in the simple model was square with a uniform intensity distribution. The effective beam half width sought was the width of the square uniform beam which produced simple model signals most like the experimental beam for comparable geometries.

If a sphere of known size and known refractive index change were passed through the experimental apparatus, the signal produced could be compared with the simple model signals for various ratios of R/δ . The known value of R and the ratio of R/δ which produced the best match would define the effective beam half width. An attempt was made to determine Δn experimentally. The difference between refractive indices of helium and air is comparable with the anticipated refractive index change for a burning kernel. It was decided to observe the signals created by the passage of helium bubbles through the laser beam. These signals were to be compared with the simple model predictions. Experimental difficulties precluded determination of δ in this way. The bubbles once formed had a short lifetime, due to evaporation of the bubble film. As the film evaporated, the surface irregularities produced signals as large as, or larger than the signal produced by the helium sphere. These problems could not be overcome and the attempt was ultimately abandoned. The value chosen for δ in the simple model was 0.9 mm. This value was the best available estimate.

The sampling volume as discussed in Section III-C must be rede-

fined in view of the simple model of the flame kernels. The kernels were assumed to be much larger than the beam diameters. In this case, it was possible for a kernel to affect the two assemblies differently. It was also possible for the kernels to affect both assemblies in like or different manner without affecting the intersection of the beams. Correlation of the two signals emphasized the common parts of the signals, but since the signal producing kernels were larger than the common sampling volume, the covariance contained contributions from outside the common sampling volume. In this case the sampling volume was defined by the size of the kernel rather than the size of the beam intersection. However, the signal level was still related to the beam size.

C. Model Verification

1. Signal shape comparisons

The signal predicted by the simple model for an arbitrary but realistic kernel diameter is shown in Figure V-9. A photograph of a detector output is reproduced in Figure V-10. The oscilloscope trace is a signal that closely resembles the predicted trace. The similarity indicated that the simple model is consistent with the a priori requirements. Much stronger type of support was the prediction of a previously unobserved phenomenon which could be checked against the data.

The signal shapes shown previously were based on the assumption that the kernel center passed through the beam center. The net



Figure V-10. Photograph of Detector Output.

deflection of the beam was in the z direction. If it was assumed that the sphere center passed some distance from the beam center, the beam deflection would be along the line joining the beam center and the sphere center. This deflection had components in both the streamwise and lateral directions. This meant that there was an output or signal in both directions from the biaxial crystals. The shape of the two signals as predicted by the simple model is shown in Figure V-11. The signals correspond to the same assumed size as the kernel used to generate Figure V-9. The shape of the signal depicting the z or streamwise beam displacement is similar to Figure V-9, but the shape of the signal depicting the lateral beam displacement is different. The streamwise and lateral signals generated by the flame are shown in Figure V-12. The similarity between the predicted and

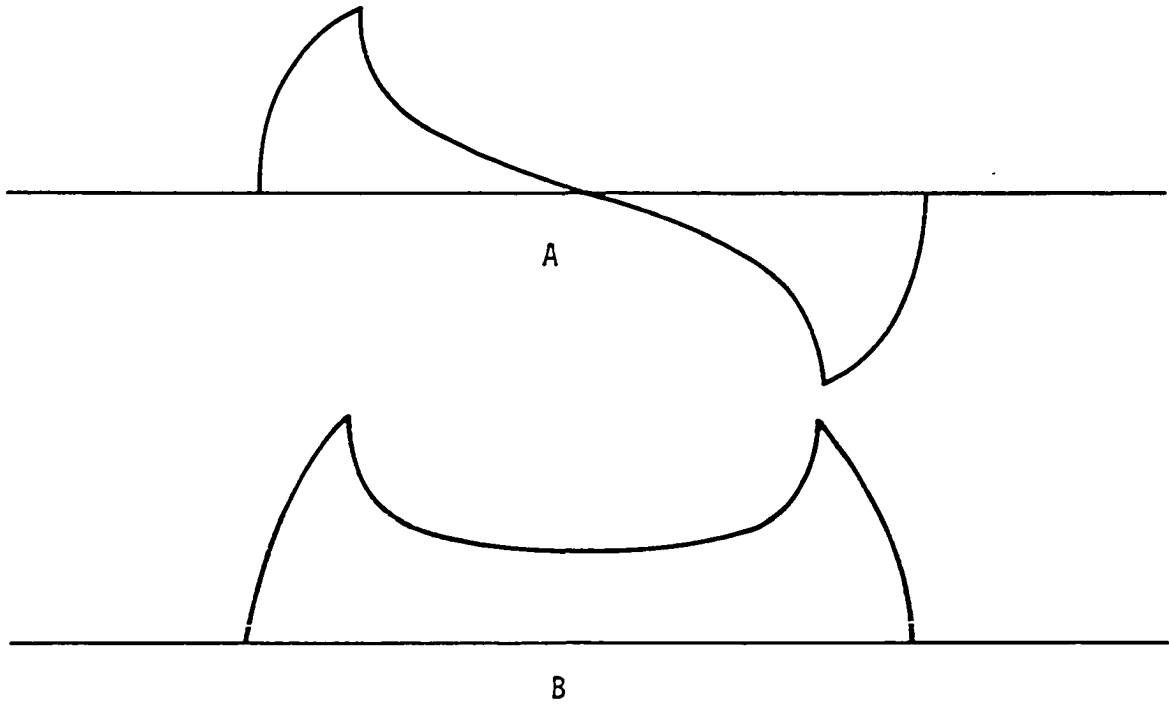


Figure V-11. Streamwise (A) and Lateral (B) Signal Shapes Predicted by the Mathematical Model for the Same Kernel As Was Assumed to Generate Figure V-9.

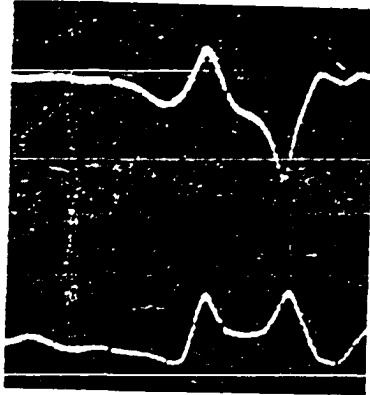


Figure V-12. Streamwise (Upper Trace)
and Lateral (Lower Trace)
Generated by the 4.5 M/S Flame.

observed signals gives strong support to the geometry of the model of the kernels. This was the first instance where the simple model was used to successfully predict a flame generated signal which had not previously been observed. Observation of either component, streamwise or lateral, was sufficient to define the radius of curvature of the surface about one axis. Observation simultaneously of both signals was sufficient to define the radius of curvature of the surface about two orthogonal axes. Only by requiring specific orientations of the burning kernels could any nonspherical geometry produce the observed signals. Spherical geometry is generalized to include ellipsoids of moderate

ellipticity. Uncertainties in the experimentally observed signals made small ellipticities undetectable. The geometry of the kernels would therefore appear to be generally spherical.

2. Flame front motion

The direction of the initial deflection as a kernel entered the beam was determined by the product $SA\Delta n$. A was always positive and the sign of S was determined by the way detectors were connected to the data recording system. The sign of Δn could be determined from the initial deflection of the beam, since the signs of all other parameters were known. The oscilloscope trace reproduced in Figure V-13 was observed with the detector connected such that upward initial deflection corresponded to a negative Δn . Negative Δn indicates that the beam passes from a region of higher refractive index to a region of lower refractive index as it enters the kernel. This means that the temperature is higher inside the kernel and that the flame front is expanding. In all cases when care was exercised to note the polarity of the connections, the deflection indicating an expanding flame front was observed.

The Abel integral inversion (51) has been used, in the past, to determine radial variations from measurements made along a ray (52, 53, and others) with the assumption that the variation in properties is axially symmetric. When a burning kernel passes centrally through the beam, it satisfies the axi-symmetric constraint. The Abel inversion is, therefore, an appropriate technique for evaluating the refractive index variations which produces the observed signals. The density

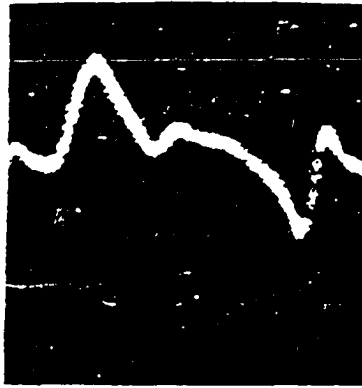


Figure V-13. Flame Generated Signal Indicating a Negative Δn .

variation was related to the refractive index variation by the same procedure as was used to determine an appropriate Δn for the simple model. The Abel inversion normally involves an integral of the derivative of an experimentally observed quantity. The derivative is a source of large uncertainty when the Abel inversion is applied to experimental data. The technique developed by L. N. Wilson for a Schlieren application eliminated the need for evaluation of the derivative. This results from the fact that the Schlieren signal is proportional to a derivative of the refractive index. Two signals corresponding to known radial refractive index variations were used to test the technique.

The first test signal was the signal predicted by the simple model for a sphere of 21 mm diameter. This size was chosen because it represented a size which was observed in the flame and because the assumptions of the simple model were justified. The signal is shown in Figure V-14. The results of the Abel inversion are shown in Figure V-15. Application of the Abel inversion reproduced the assumed density profile. The maximum density change observed agreed with the assumed maximum to four significant digits. The simple model assumptions are least justified at the edge so the observed slight dip in the profile is not surprising. The gradient at the right edge of the profile was the response of the finite size beam to a discontinuity in refractive index. The dashed line represents the radius at which the density change is half the maximum density change. This radius was used as the experimentally determined sphere radius. The agreement between the assumed radius and the observed radius was excellent.

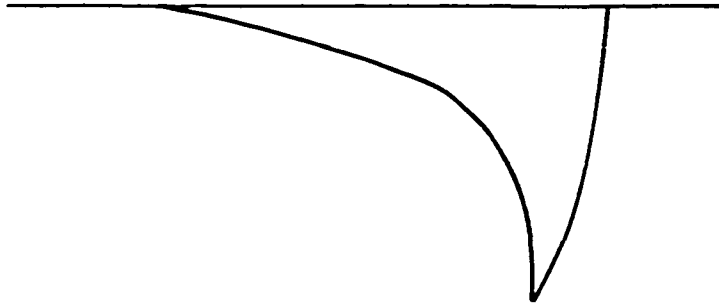


Figure V-14. Half of Simple Model Signal Corresponding to Kernel of 21 mm Diameter.

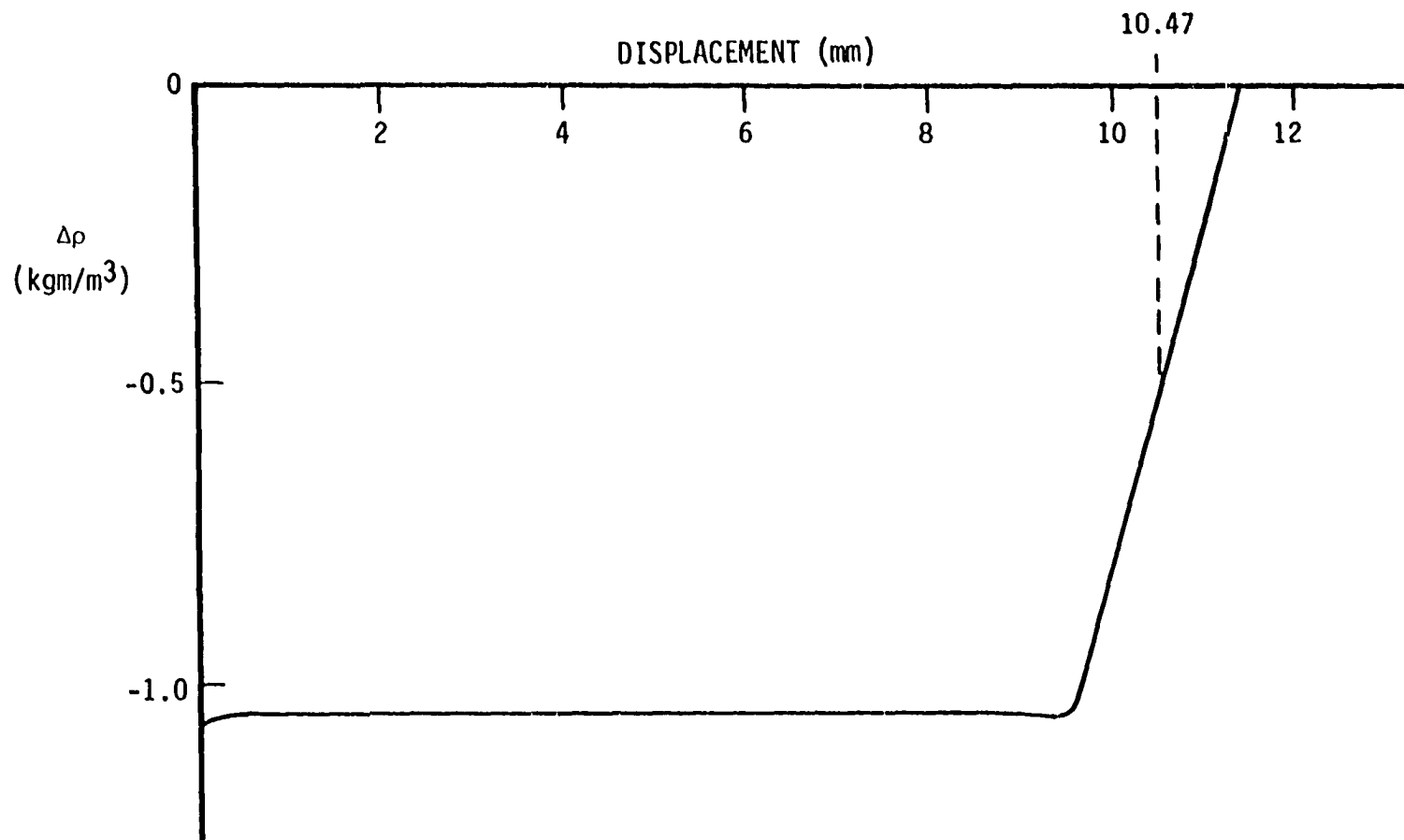


Figure V-15. Abel Inversion of Simple Model Signal Shown in Figure V-14 Showing Density as a Function of Radius.

The second test signal used was the signal produced by passing a helium bubble through the beam. The problems of bubble distortion and light dispersion by the film limited the accuracy of the signal (see Section V-B-2). The best available signal is shown in Figure V-16. The density profile produced by the Abel inversion is shown in Figure V-17. The density profile is relatively constant over a large part of the profile. The maximum density change is about 12% less than the known change for a helium bubble at laboratory conditions. This was attributed to the noncentral passage of the bubble through the beam. The noncentral passage also contributed to the nonuniformity of the profile. The inversion for small values of r is extremely sensitive

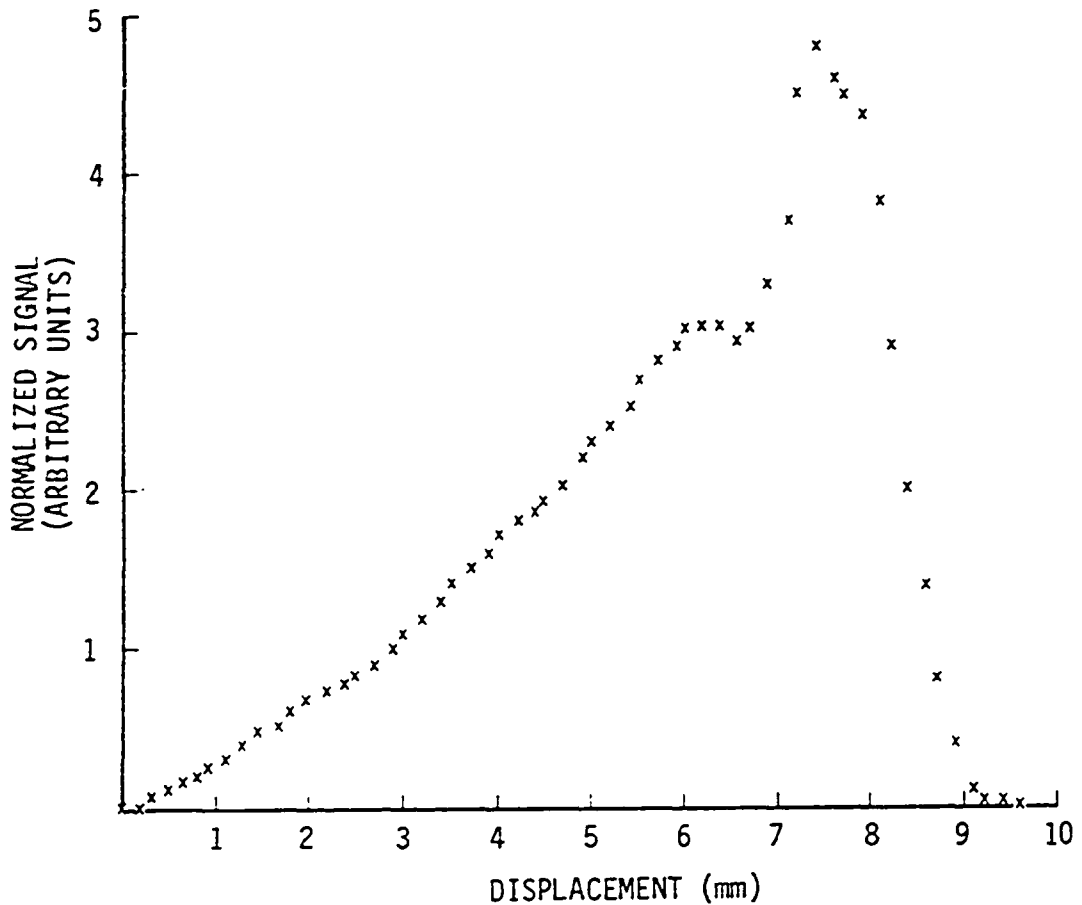


Figure V-16. Signal Generated by Passing a Helium Bubble Through the Laser Beam.

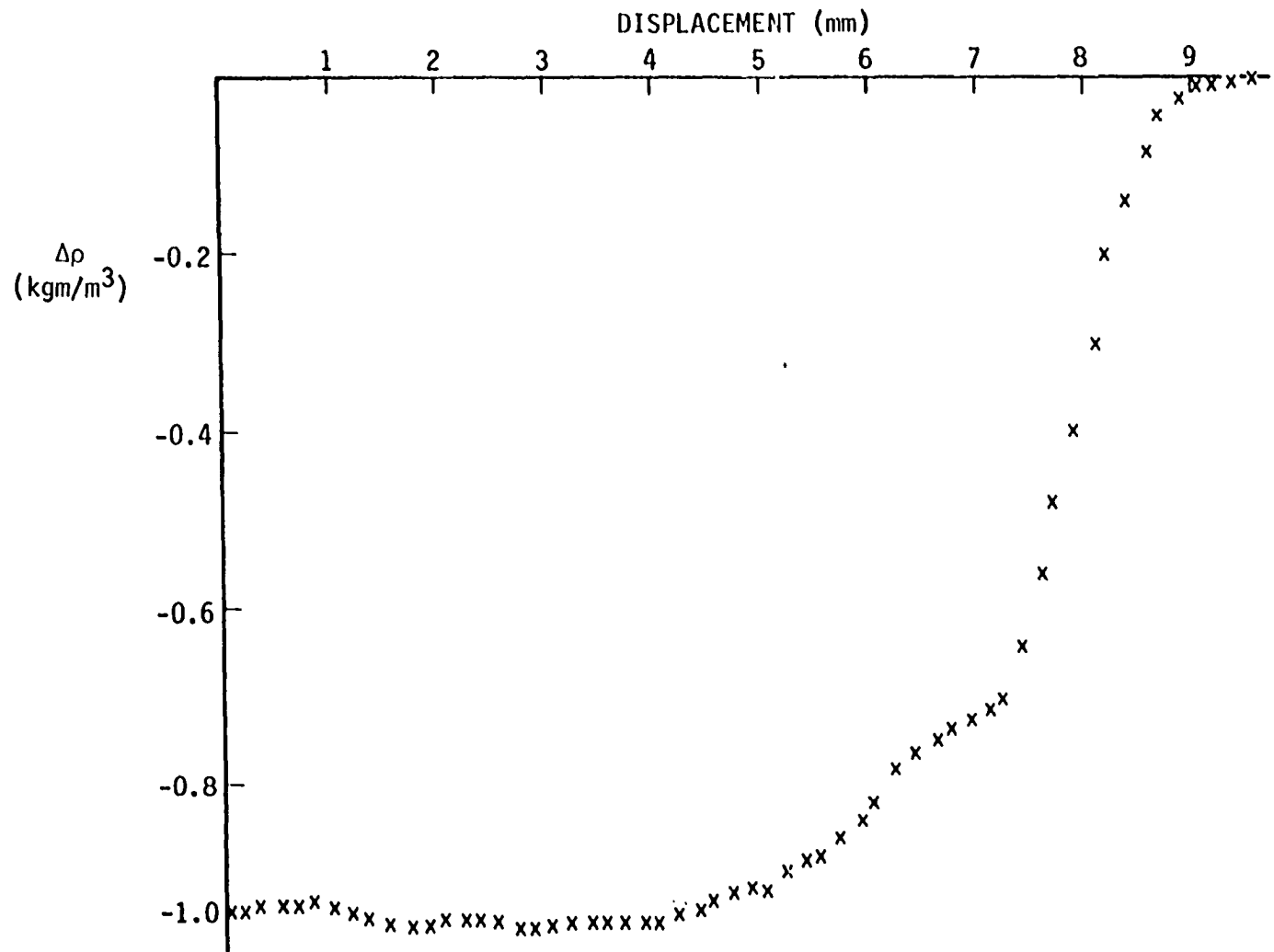


Figure V-17. Abel Inversion of the Signal Shown in Figure V-16 Showing Density as a Function of Radius.

to the signal level near the zero crossing where the signal level was lowest. The beginning of the density gradient was less distinct than was anticipated, again because of signal uncertainty.

The flame generated signal used with the Abel inversion is shown in Figure V-18. The initial conditions for this flame were stoichiometric propane and air at temperature 294°K and pressure 0.986 E+05 Pa. The approach speed was 4.5 m/s. Complete combustion was assumed. The pressure was assumed constant and the adiabatic flame temperature was used as the final temperature. The detector moment arm used was the distance from the burner centerline to the detector. The sensitivity was measured



Figure V-18. Flame Generated Signal Chosen for Application of the Abel Inversion. Signal Generated in 4.5 m/s Approach Speed Flame at a Height of 0.12 m Above the Exit Plane.

in the usual manner. The density profile calculated by the Abel inversion is shown in Figure V-19. The magnitude of the maximum density change is approximately what was expected, based on the assumptions. The uncertainty in the moment arm is ± 30 mm or about $\pm 7.5\%$. The lateral signal which accompanied this streamwise signal indicated that the kernel center passed very near if not through the beam. The final temperature was not the adiabatic flame temperature but an error of several hundred degrees in the final temperature would have little effect on the magnitude of the density change. The difference between the observed and calculated density changes was less than the known uncertainties. The Abel inversion indicated that the kernel was an expanding flame front. The density change was relatively constant over a large portion of the profile. The gradient region was well defined in contrast to the helium bubble density profile shown in Figure V-17.

The convection speed was used to determine the size of the kernel. The convection speed was determined statistically and thus has an inherent uncertainty resulting in an uncertainty in the size of the kernel. The radius of the kernel determined in this way was 14 mm. The signal shown in Figure V-18 produced a density profile which was typical of the best obtainable from flame generated signals.

The fundamental frequency of the signal produced by a flame kernel is directly proportional to its convection speed and inversely proportional to the size of the kernel. As a kernel is convected downstream, the fundamental frequency of its signal will decrease as its diameter increases. It was impossible to observe individual kernels,

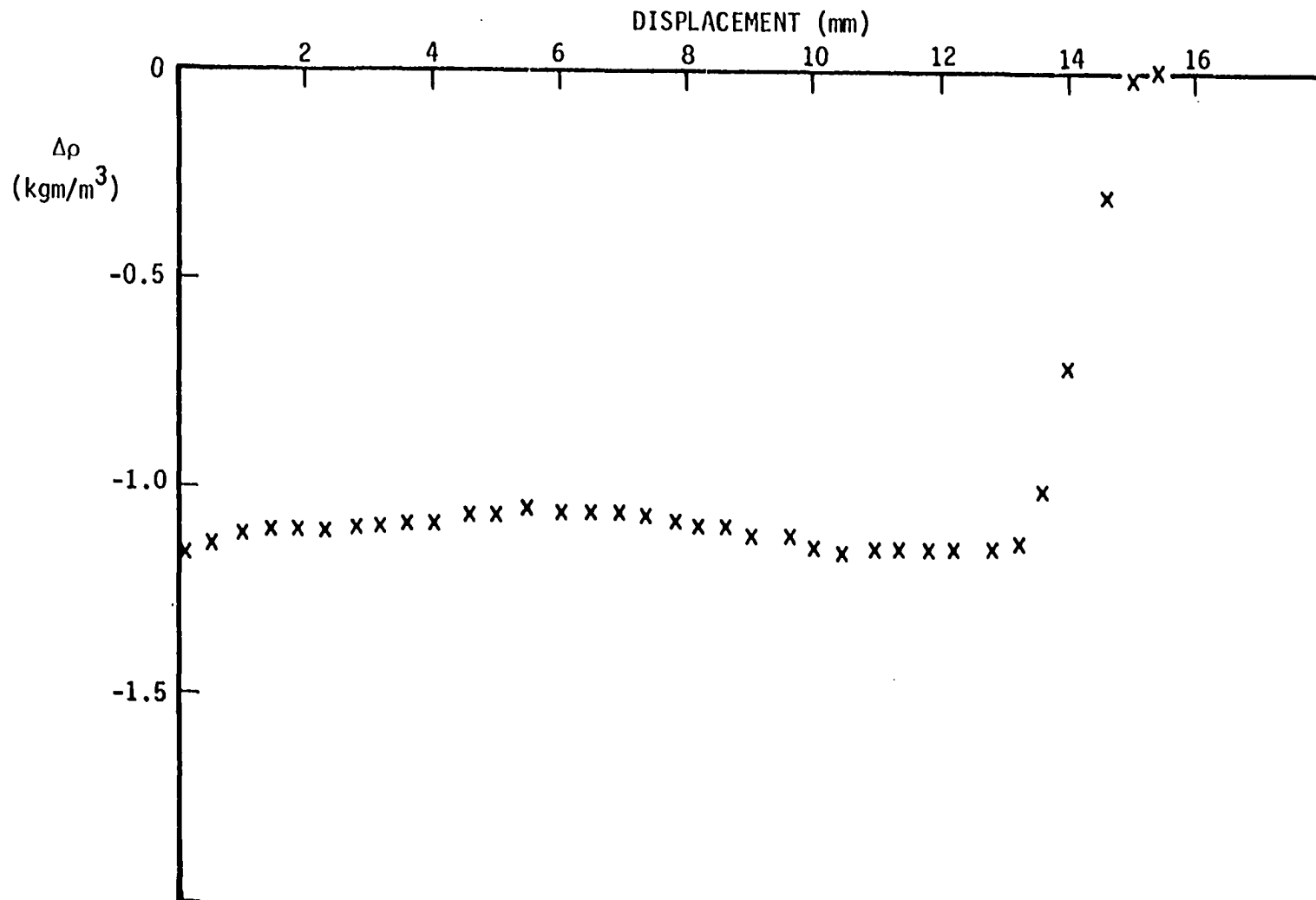


Figure V-19. Density Profile Calculated from the Flame Generated Signal Using the Abel Inversion.

but it was possible, statistically, to observe many kernels as they were convected downstream. An experiment was devised to show the growth in size, or decrease in frequency of individual kernels as they were convected downstream. Beam A was positioned 14 cm above the exit of the burner and beam B was positioned 20 mm above beam A. Two filters were used on each input channel of the correlator resulting in an attenuation of 48 db per octave giving a narrower bandwidth and better spectral resolution. Absolute levels of covariance were not required for the analysis so the amplifiers were set to produce a reasonable input signal level and were not readjusted. Low levels of covariance were expected so the correlator was allowed to run continuously until a measurable covariance was obtained (about ten minutes). In each step the same section of tape recorded data was analyzed. The signal from assembly A was filtered at 600 Hz and the signal from assembly B was filtered at a different frequency in each step of the analysis. The simple model predicted peak signal levels which were proportional to the square root of the size and therefore proportional to the reciprocal of the square root of the frequency and the covariances were corrected for the variable peak signal size. The covariances were also corrected for the variable bandwidth of the filters used on channel B of the correlator input. The net correction at each frequency was proportional to $f^{1/2}$. The covariances were divided by the covariance obtained with signal B filtered at 600 Hz. The results with and without the correction are shown in Figure V-20.

The ratio of covariances from Figure V-20 was largest at about 525 Hz. This indicates that signal B filtered at about 525 Hz had

RATIO OF COVARIANCES

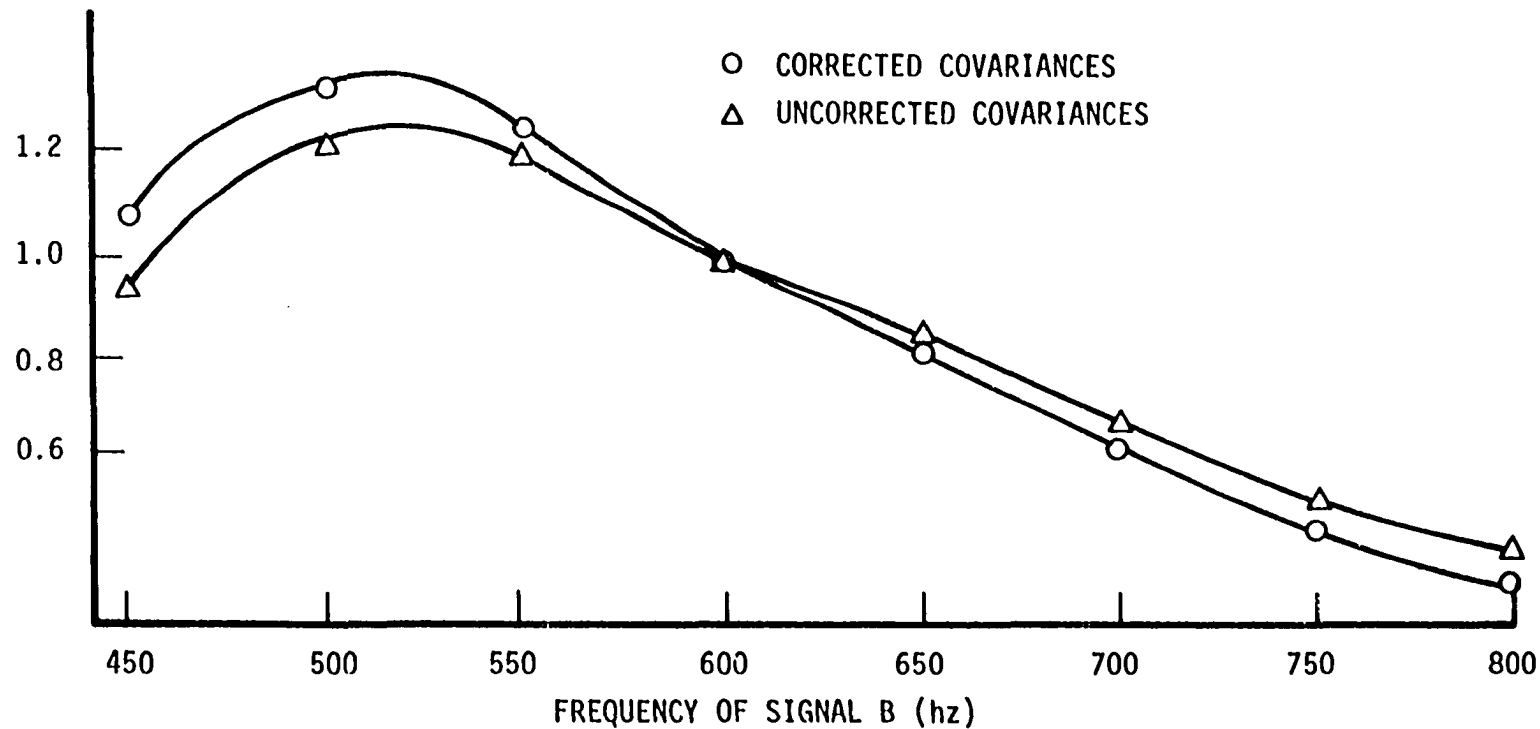


Figure V-20. Corrected and Uncorrected Ratios of Cross Covariances of Flame Generated Signals. Signal A Observed at 0.14 m Above Exit and Filtered 600 hz. Signal B Observed at 0.16 m Above the Exit and Filtered at Various Frequencies. 4.5 m/s Approach Speed Flame.

more in common with signal A filtered at 600 Hz than when signal B was filtered at any other frequency. Considering only kernels which produce a 600 Hz signal in assembly A, the most likely frequency signal in assembly B was 525 Hz. This could occur only if the diameter of the kernel was larger when it passed beam B than when it passed beam A. Each kernel did not necessarily increase in diameter as it moved from beam A to beam B, but the covariances observed were strong support for the hypothesis that most kernels were expanding.

A fundamental frequency of 600 Hz corresponded to a diameter of about 5 mm based on the simple model. A kernel of larger diameter could produce a signal of 600 Hz if its center did not pass through beam A. When the kernel encountered beam B, it could produce a signal of any frequency less than or equal to its fundamental frequency. The frequency depended upon the location of kernel center relative to the beam. This fact accounted for the covariances observed at frequencies above and below 525 Hz.

D. Qualitative Signal Observations

An instantaneous Schlieren photograph of 4.5 m/s approach speed flame is shown in Figure V-21. The single beam signals representing the streamwise and lateral (or Z and Y) beam displacements are also shown. The lowest trace, observed at 10 cm above the burner exit shows large amplitude signals but relatively little activity. Low in the flame region, the reactants surrounding the flame kernels are relatively cool giving a maximum value of Δn and accounting for the

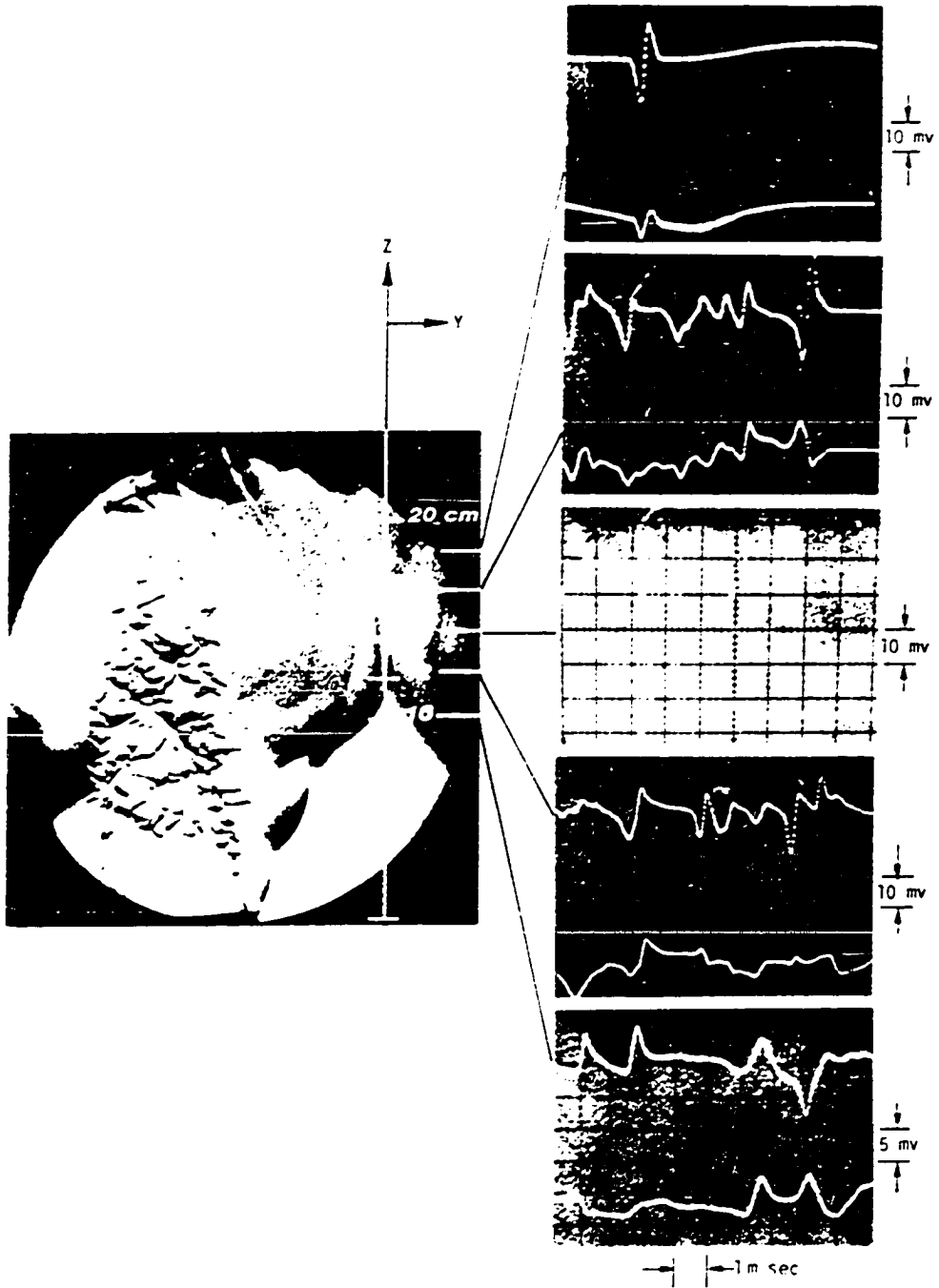


Figure V-21. Instantaneous Schlieren Photograph of 4.5 m/s Approach Speed Flame and Examples of the Streamwise (Upper Trace) and Lateral (Lower Trace) Signals Observed at Various Heights Above the Exit Plane.

large amplitudes. These signals originate in the periphery of the flame. In the right portion of the photograph are an excellent pair of signals corresponding to a kernel passing noncentrally through the beam.

At 12 cm above the exit, the signal traces show increased signal activity which leads to significant overlap of signals. This overlap was the result of more than one kernel interacting with the beam at any given time. The result of this overlap was a signal which, in general, did not resemble the simple model signal predictions.

The traces observed at 14 cm above the exit show a significant overlap and a high level of activity. The traces from the three intermediate heights, 12, 14, and 16 cm, were similar. The similarity was sufficient that on the basis of one trace, differentiation among the three was impossible. By studying numerous examples, distinctions did arise. These distinctions will be mentioned, although they are not necessarily obvious.

The traces taken at 14 cm represent the most active signals in both the streamwise and lateral directions. Signals like those predicted by the simple model in Section V-B-2 were virtually impossible to observe. The peak level of the signals was comparable to the levels observed in the lower part of the flame but the signals occurred more frequently resulting in a higher mean square signal.

The traces taken at 16 cm show a slight decrease in peak signal level and activity. The signals were in most ways equivalent to the signals observed at 12 cm. The pair of signals shows the streamwise and lateral displacement of the beam caused by the off-center passage of a flame kernel.

The traces taken at 18 cm clearly show a change in character of the signal. Their maximum amplitude is small and there are long times when low signals or no signals were present. This was indicative of the later stages of combustion. Any kernels that might still persist in this region were in a hot environment, reducing the Δn across the flame front and hence the signal level. In this region, the simple model derived for the initial stages of combustion was less appropriate. The expanding kernels have grown together leaving odd-shaped unburned regions in their place. The remaining unburned volumes continue to be consumed but their shapes will be far from spherical.

Only low levels of covariance could be obtained at greater heights above the exit. Individual traces indicated that the only signals consistently observed above this level were a result of the billowing in the periphery of the flame region.

E. Model Based Data Analysis

1. Simple model analysis

The model of the combustion process developed in Section V-B was used to transform the flame generated signals into equivalent physical processes. This was done by analyzing the signals calculated using the simple model in a manner equivalent to the analysis of the flame generated signals. The simple model signals were auto-correlated and the correlations were Fourier transformed. These transforms produced two parameters which were used in the data analysis. The first parameter of interest was the characteristic wavelength of the signal. This wave-

length was the wavelength which corresponded to the peak of the transform. The convection speed divided by the characteristic wavelength was taken as the frequency of the signal. Since the simple model signals were of finite duration and were not pure sine waves, the transforms had nonzero magnitudes at nearly all frequencies, or wavelengths, particularly at harmonics of the frequency of the peak.

The second parameter was the total "energy" or mean square amplitude of the simple model signal. This was determined by applying the appropriate filter transfer function to the transform and integrating over all frequencies. The simple model thus provided a method of relating a frequency observed in the flame generated signal to a physical size and a method of determining the contribution of a single kernel to the total correlation. A more detailed description of the simple model analysis is contained in Appendix A.

2. Data reduction using simple model analysis

The spectra were transformed from the frequency domain to the wavelength domain. They were then transformed to the size (L) domain. The transform equations used were

$$U_c = f\lambda$$

$$f = U_c/\lambda$$

$$G(\lambda) = G(f) \left| \frac{df}{d\lambda} \right|$$

$$\frac{df}{d\lambda} = - U_c/\lambda^2$$

$$= - f^2/U_c$$

$$G(\lambda) = G(f)(f^2/U_c)$$

$$\text{and } G(L) = G(\lambda) \left| \frac{d\lambda}{dL} \right|. \quad (\text{V-6})$$

L was not known as an analytic function of λ . $\frac{d\lambda}{dL}$ was approximated by $\Delta\lambda/\Delta L$ obtained from the simple model analysis. These consecutive transformations yielded the signal level as a function of the kernel size. It now remains to relate a distribution of kernel sizes to the spectra observed in the flame.

The output of the correlator, when not set to integrate continuously, was normalized to an integration time of one second. The covariance was the average product but was also the rate of accumulation of the mean square level of the signal. The signal level for single kernels as a function of size was known from the simple model analysis and the signal level accumulated in one second as a function of size was known from the flame measurements. The ratio of these two then, should be the equivalent number of kernels per second which were detected by the correlation of the two signals. This was the kernel passage rate through the beam intersection. It is stressed that the resulting number was the number of simple model kernels which would have produced the observed signal correlation. The numbers so obtained did not account for the contribution to the correlation of signals generated by noncentral crossing of kernels of size larger than L . The contribution from kernels which do not execute identical interactions with the two beams is also included. The contributions to the correlation from nonidentical interactions and noncentral crossings depended on the exact signal shape much more strongly than did the contribution of the central crossing.

The detailed signal shape depends on the precise geometry of the kernels. Information was not available to define the geometry for analysis of the contributions of the noncentral crossings.

The kernel passage rates as a function of diameter, $\dot{N}(L)$, for the growth and decay regions of the two flames are shown in Figures V-22-A, B, C, and D. The distinction to be noted is not between the two flames but between the two regions of each flame. The passage rate increases from the base of the flame to a maximum at about 15 to 18 cm for the 8 m/s flame and about 14 cm for the 4.5 m/s flame. The kernel passage rate decreases rapidly above the height of the maximum. The data from the highest measurement location bear little resemblance to the data from the lower heights.

If the kernel passage rate distribution is divided by the convection speed and then is summed over the range of sizes, a measure of the centerline activity is obtained. This sum,

$$A_f(H_z) = \sum_{L_{\min}}^{L_{\max}} \dot{N}(L)(L)(\Delta L)/U_c, \quad (V-7)$$

represents the fraction of the time a kernel was interacting with the beam intersection. The activity fraction $A_f(H_z)$ was calculated at each measurement station. The results are shown in Table V-1 for the two approach speeds. The variation in the activity fraction was monotone on each side of the maximum. The maximum in each case was less than 0.25. Reasons for this will be explained later.

The plots of Figure V-22 are biased toward the larger kernels, since a small kernel must pass almost centrally through the beam to contribute to the signal but a large kernel can pass with its center

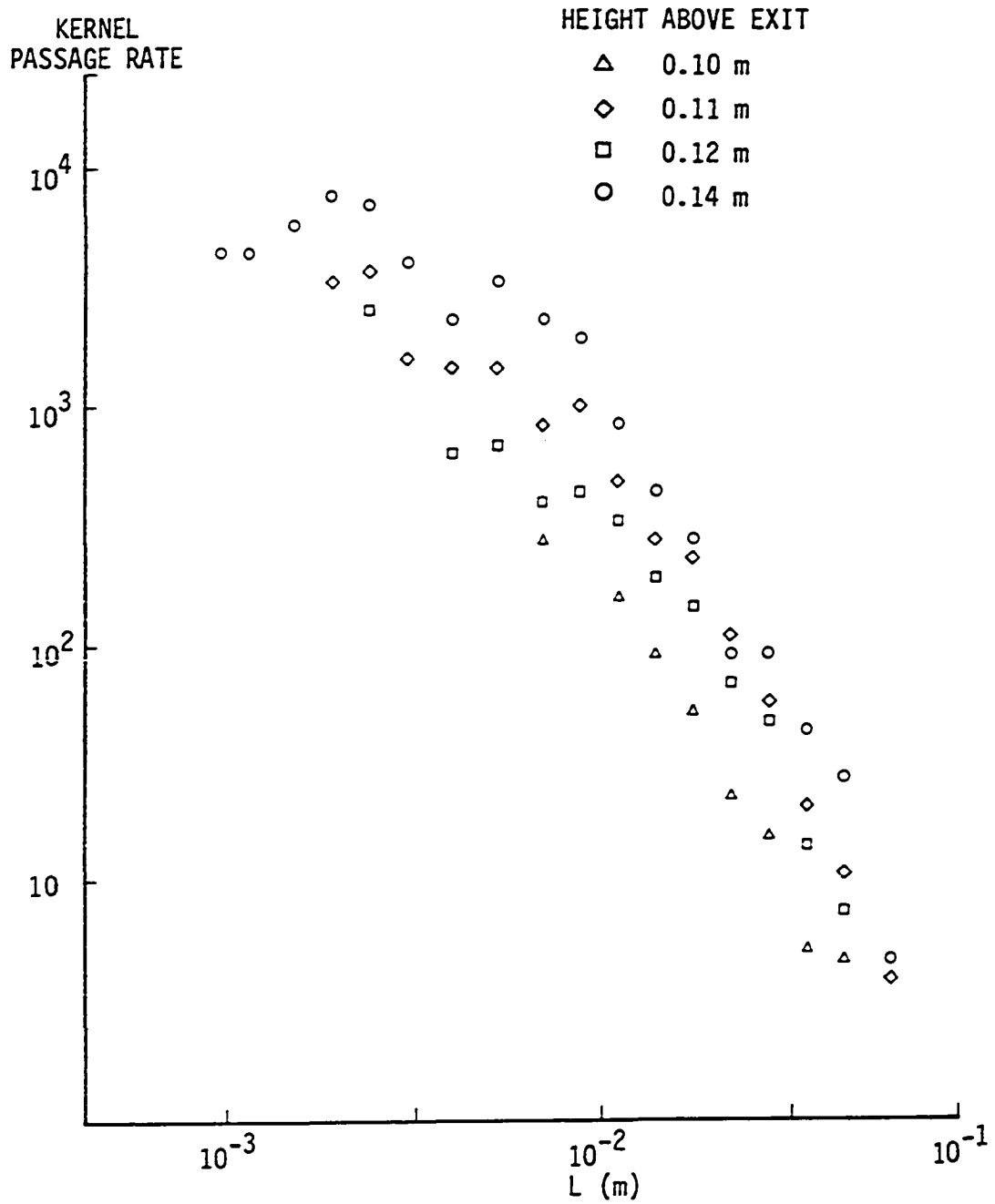


Figure V-22-A. Kernel Passage Rates as a Function of Kernel Diameter in the Growth Region of the 4.5 m/s Approach Speed Flame.

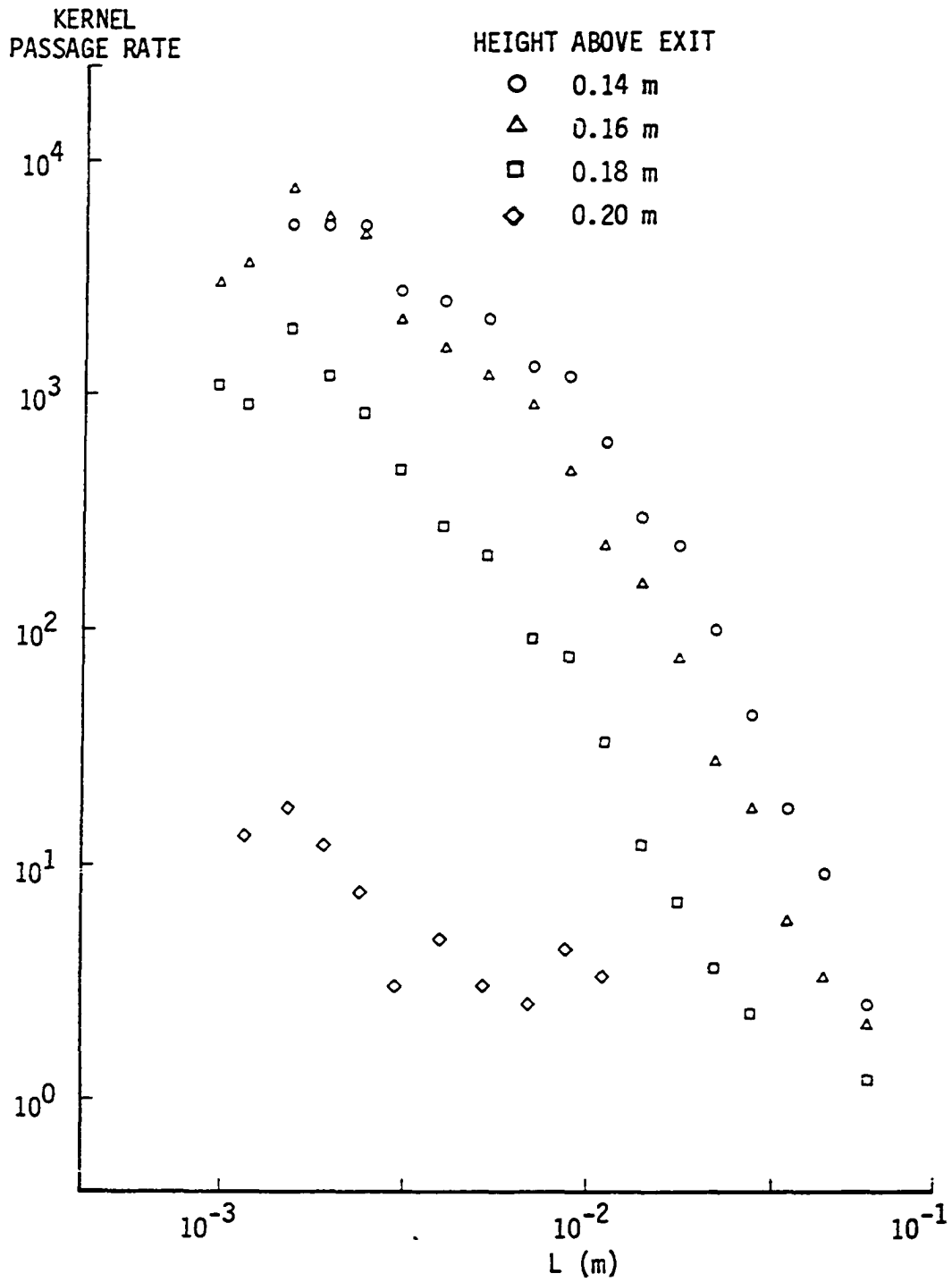


Figure V-22-B. Kernel Passage Rate as a Function of Kernel Diameter in the Decay Region of the 4.5 m/s Approach Speed Flame.

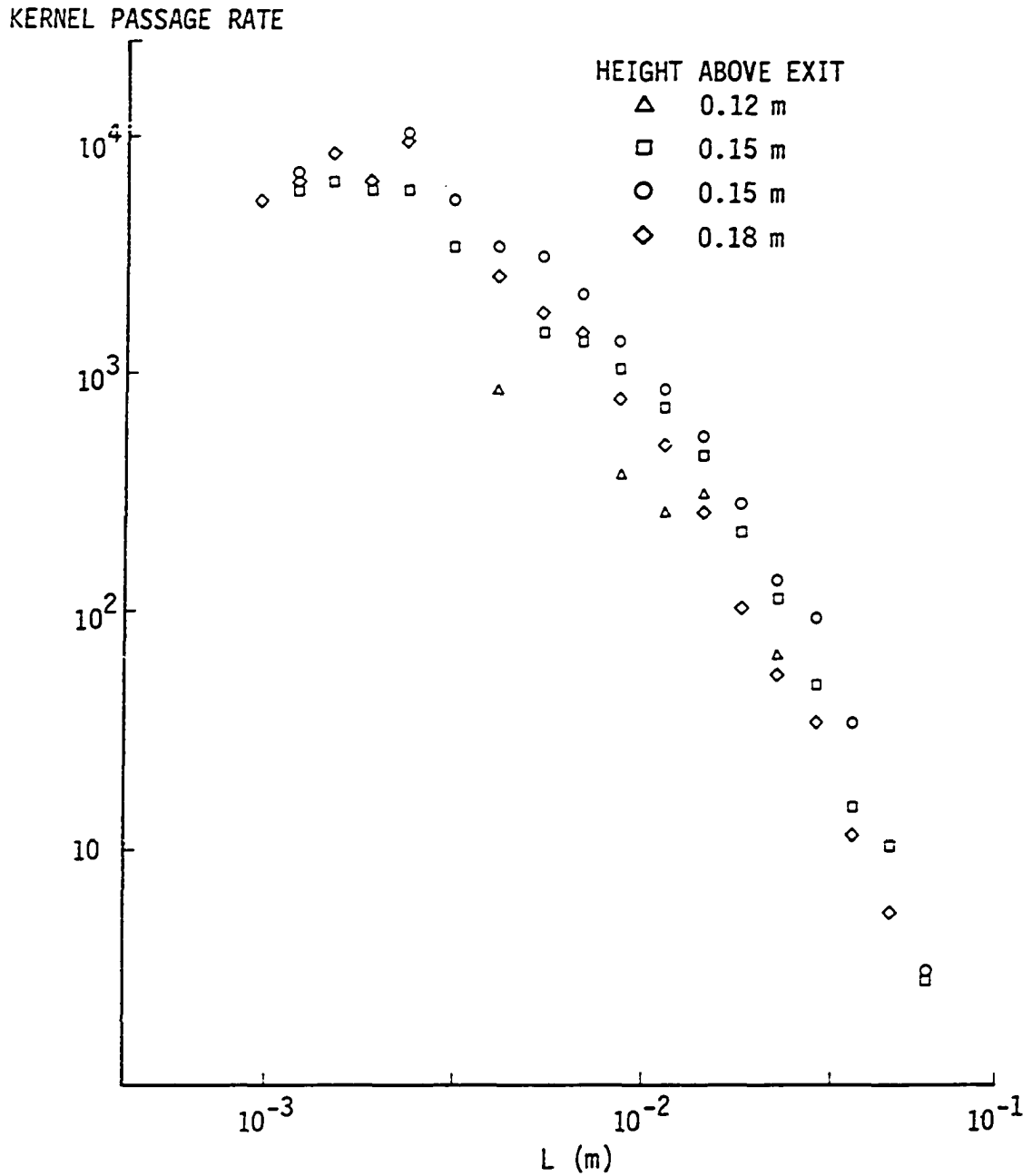


Figure V-22-C. Kernel Passage Rate as a Function of Kernel Diameter in the Growth Region of the 8 m/s Approach Speed Flame.

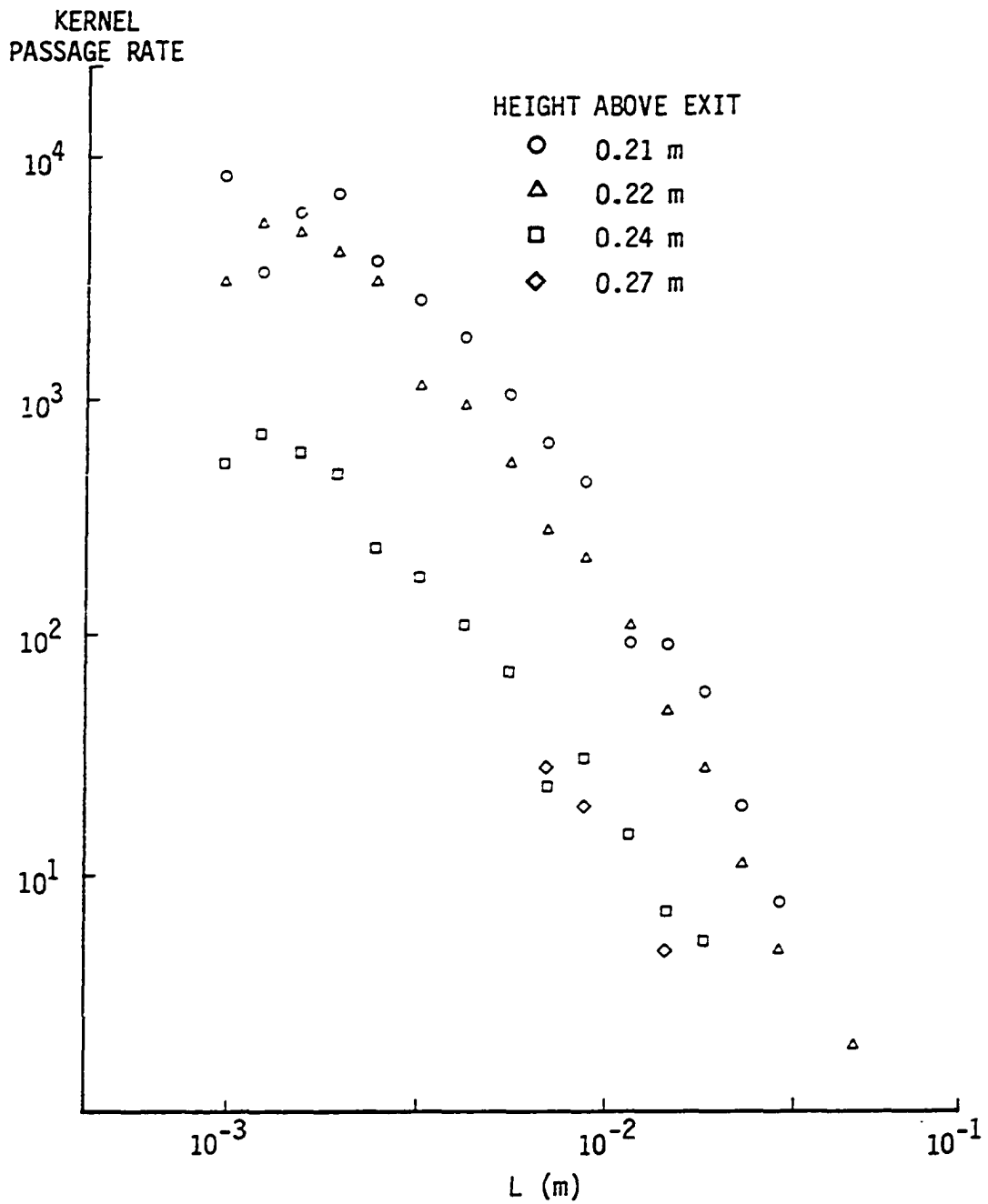


Figure V-22-D. Kernel Passage Rate as a Function of Kernel Diameter in the Decay Region of the 8 m/s Approach Speed Flame.

Table V-1. Activity fraction as a function of height

Activity fraction				
4.5 m/s		8 m/s		
Height	$A_f(H_z)$	Height	$A_f(H_z)$	
0.10	0.0169	0.12	0.0006	
0.11	0.0147	0.15	0.075	
0.12	0.076	0.15	0.081	
0.14	0.169	0.18	0.190	
0.14	0.130	0.21	0.081	
0.16	0.096	0.22	0.016	
0.18	0.0147	0.24	0.0099	
0.20	^a	0.27	0.0003	

^aInsufficient data.

several beam diameters from the beam and still generate a signal. An interaction cross section was defined to compensate for the bias in the kernel passage rate. The derivation of the interaction cross section was based on the simple model and is presented in the Appendix. The cross section was calculated for each kernel diameter in the range of interest. The area of the interaction cross section was found to be about $\pi/20 L^2$. The kernel passage rate was divided by the interaction cross section producing a kernel flux distribution as a function of kernel size.

The kernel fluxes are shown in Figure V-23. The flux increased in the growth region, reached a maximum, and decreased rapidly in the decay region. The flux distributions for the two flames in their

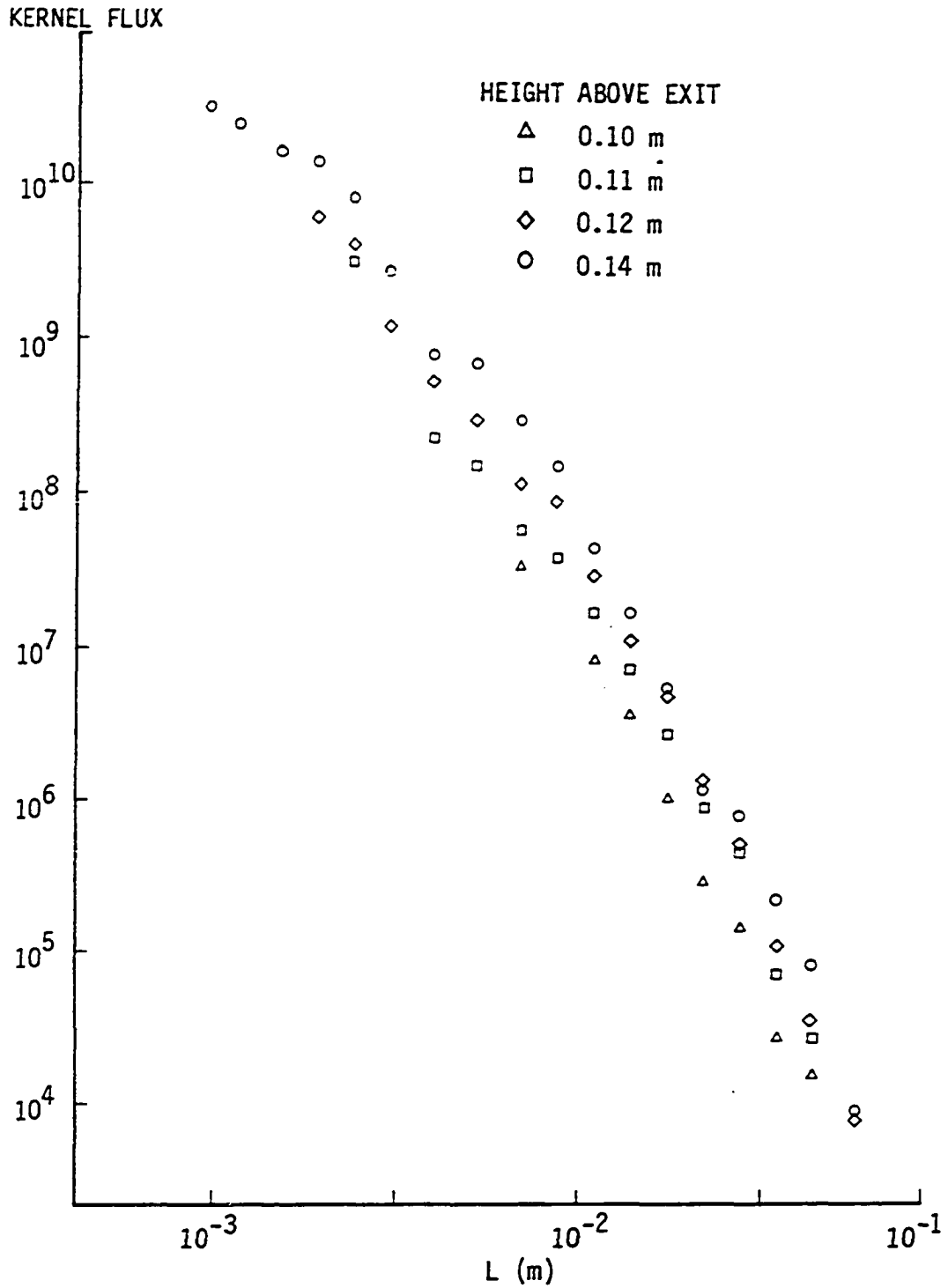


Figure V-23-A. Kernel Flux Distribution for the Growth Region of the 4.5 m/s Approach Speed Flame.

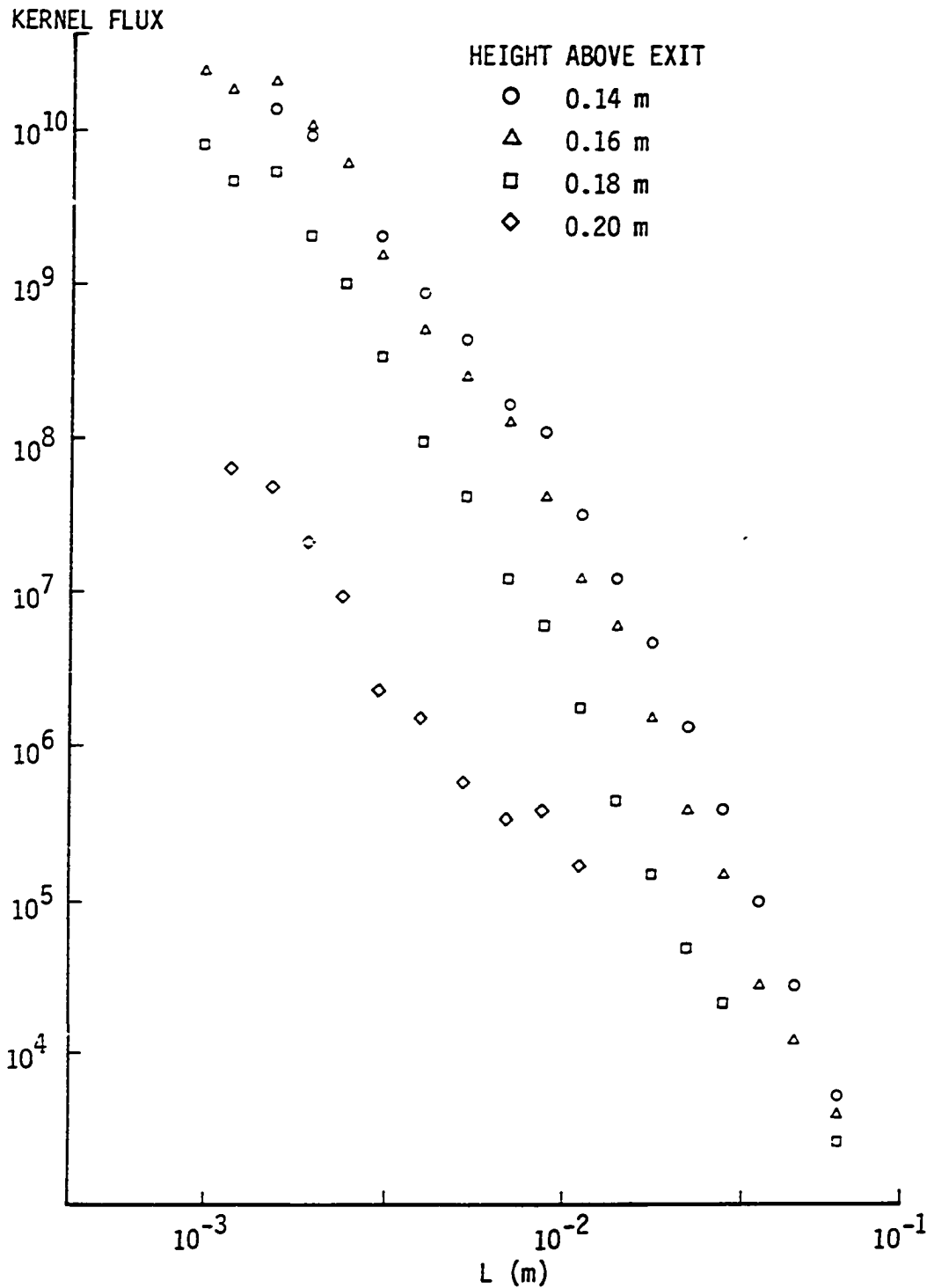


Figure V-23-B. Kernel Flux Distribution for the Decay Region of the 4.5 m/s Approach Speed Flame.

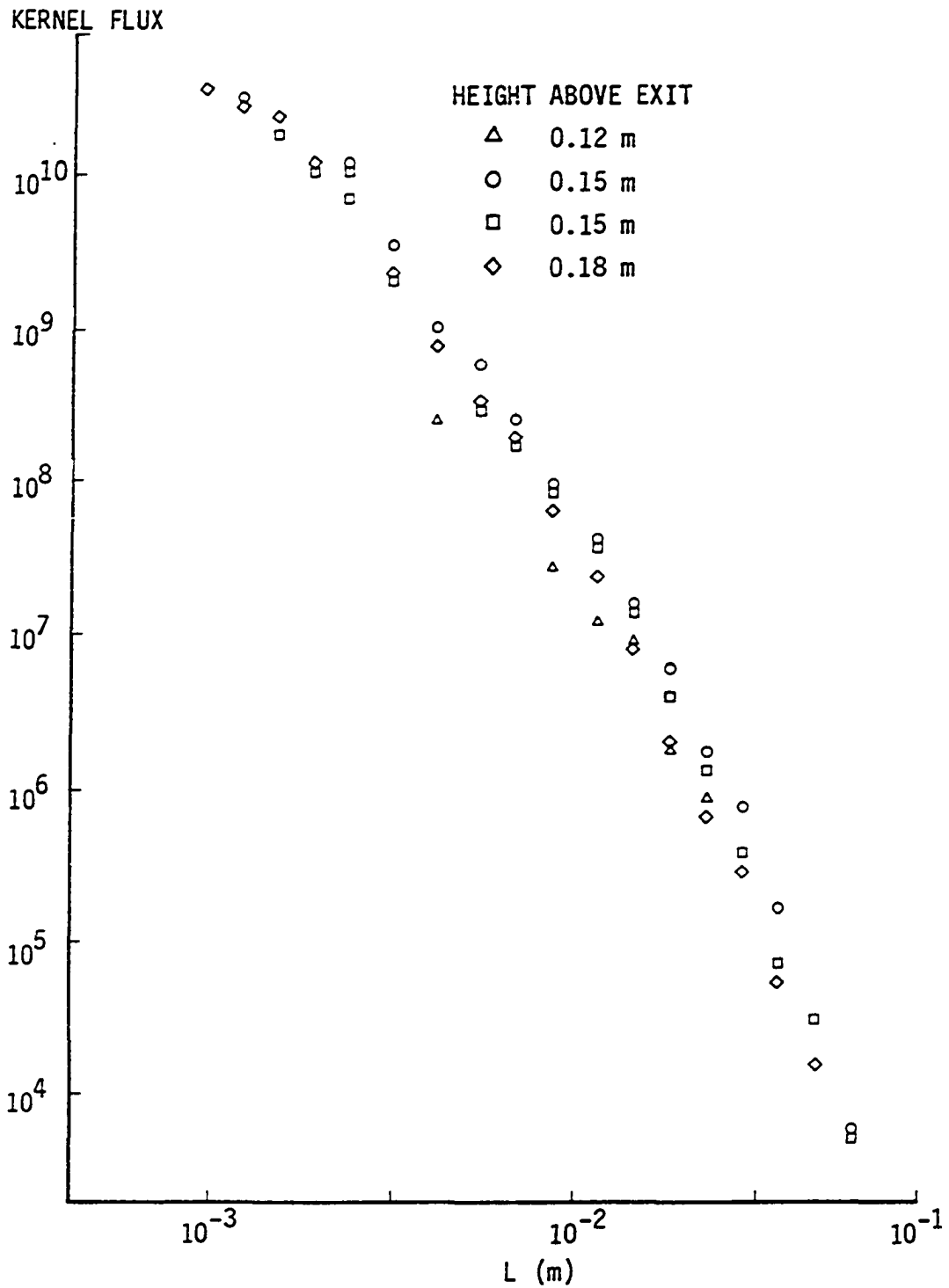


Figure V-23-C. Kernel Flux Distribution for the Growth Region of the 8 m/s Approach Speed Flame.

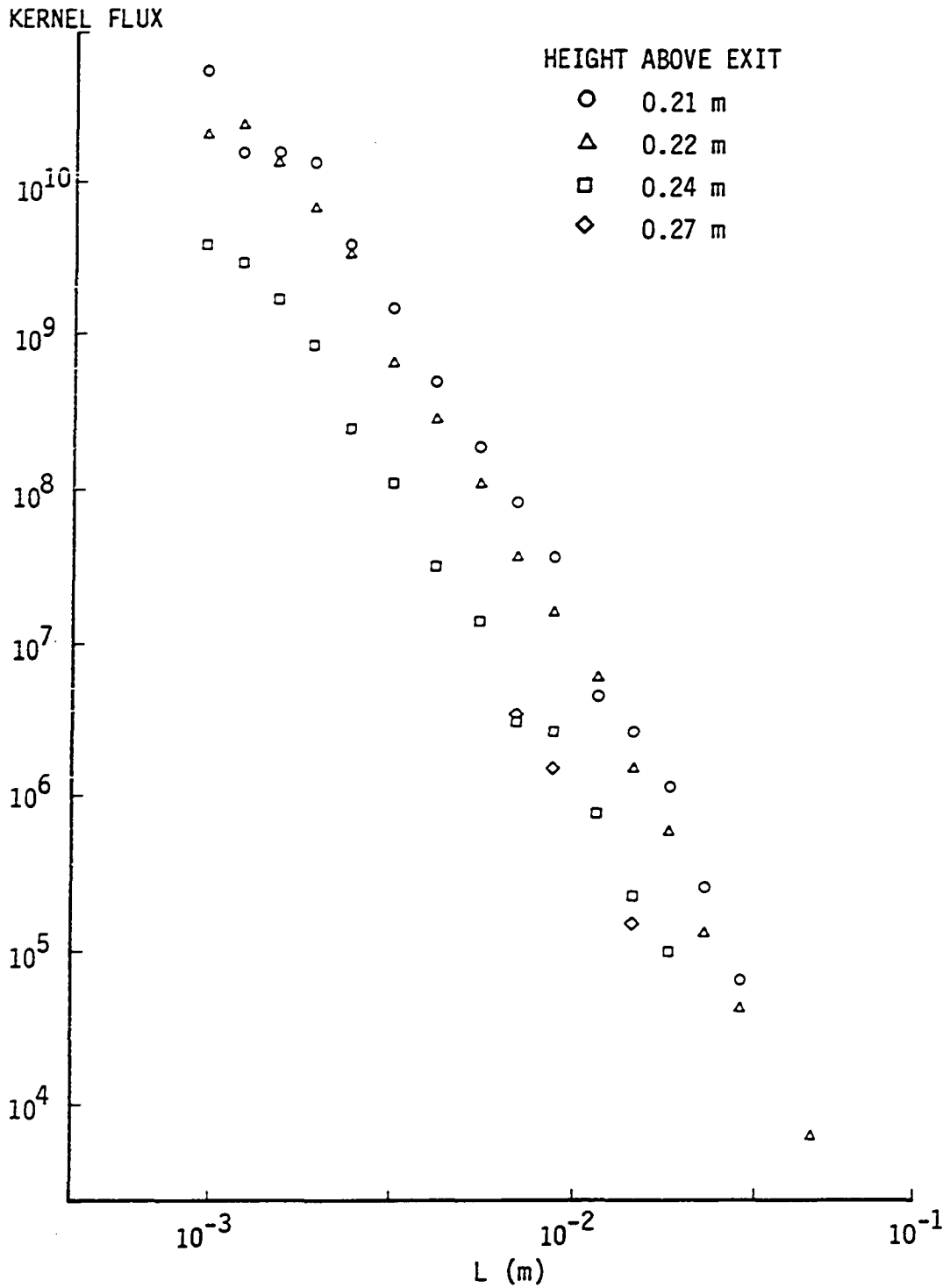


Figure V-23-D. Kernel Flux Distribution for the Decay Region of the 8 m/s Approach Speed Flame.

most active region are replotted in Figure V-24.

The activity fraction defined above was a means of comparing the total signal levels at various locations in the flames. Another method of observing the same trends in the data is shown in Figure V-25, where the fluxes of four sizes of kernels were plotted as a function of height above the exit. The fluxes are maximum at about the same height as the activity fraction.

Since the flux was the result of a kernel number density distribution, $K(L)$, past the measurement station, the equivalent kernel number density was obtained by dividing the flux by the appropriate convection speed. The kernel number densities as a function of size are plotted for the growth regions and decay regions of the two flames in Figures V-26-A, B, C, and D. The number density distributions corresponding to the data plotted in Figure V-24 were combined and curve fit by the method of least squares. The best correlation of the data and the equation was obtained using the equation

$$K(L) = 0.588L^{-3.656} \quad (V-8)$$

The data from the range of diameters $1.8 \text{ mm} < L < 32 \text{ mm}$ were used in the curve fit. This was the range of sizes where the assumptions of the simple model were justified. The correlation of the equation and the combined data, C'_{ed} , was 0.988. Other forms of the equation were tested, exponential, polynomial, and logarithmic, but all required more terms to approach the correlation obtained with the above form. The data of Figure V-24 were transformed and replotted in Figure V-27.

The data from each measurement station in both flames were fit

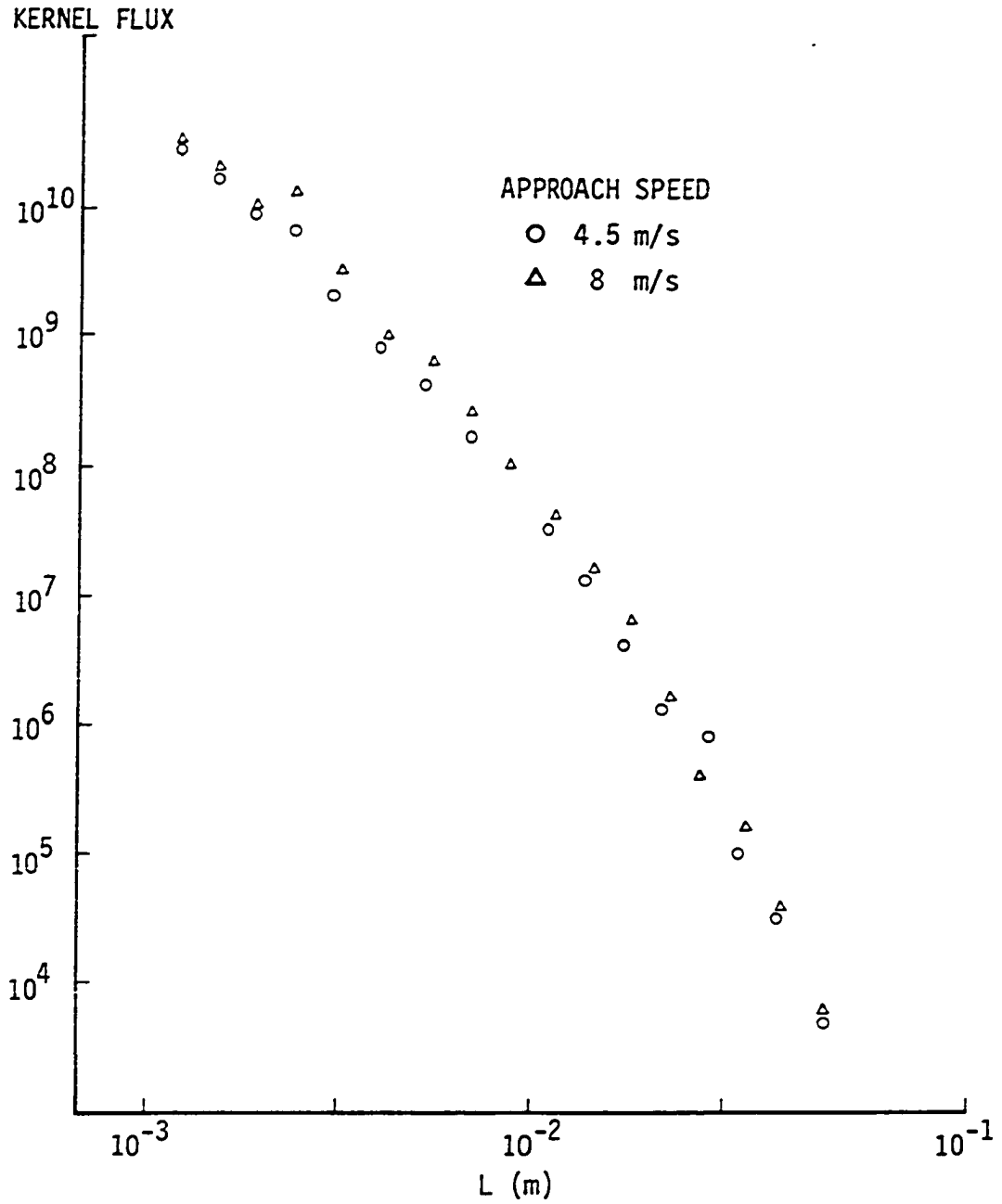


Figure V-24. Kernel Flux Distributions for the Most Active Region of the 4.5 m/s and 8 m/s Approach Speed Flames.

KERNEL FLUX

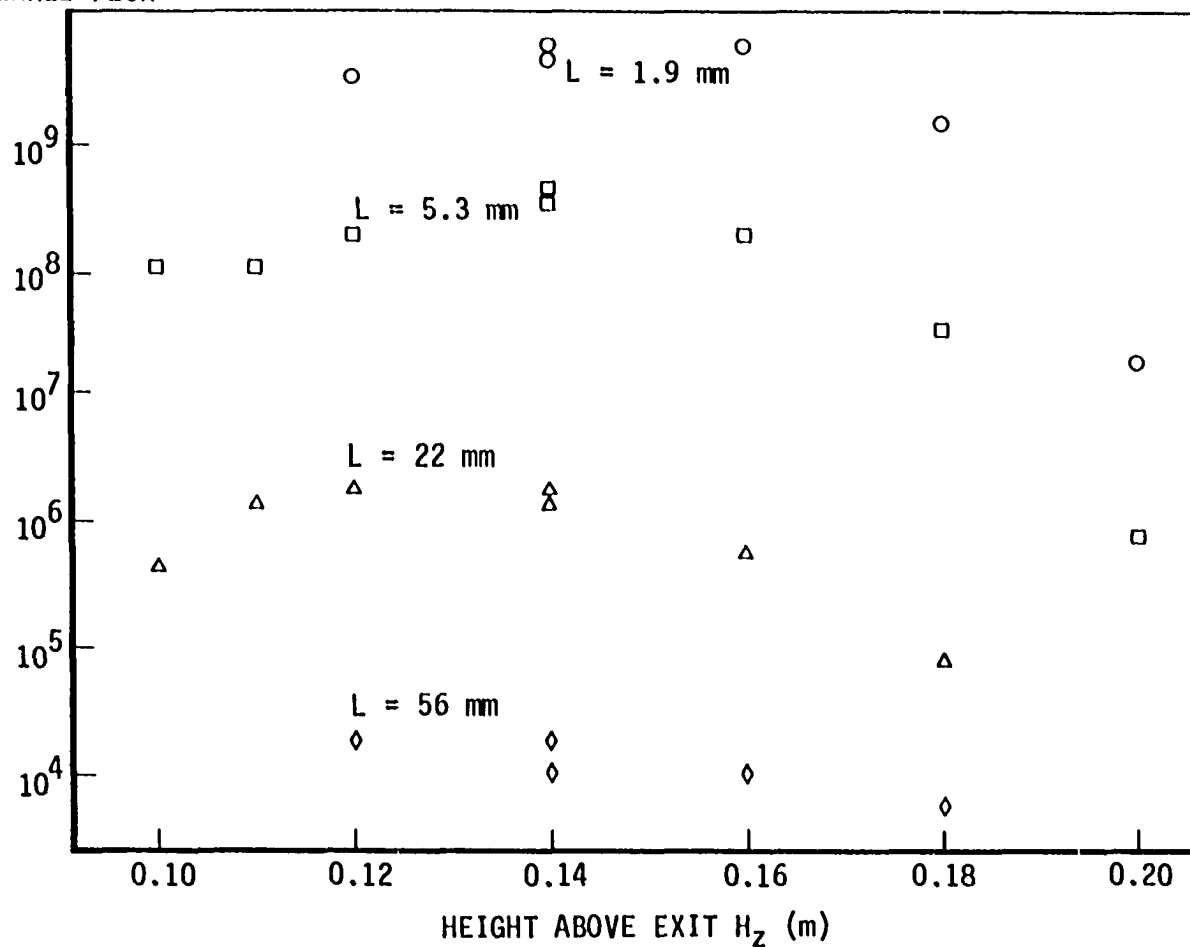


Figure V-25. Fluxes of Four Specific Size Kernels as a Function of Height Above the Exit Plane for the 4.5 m/s Approach Speed Flame.

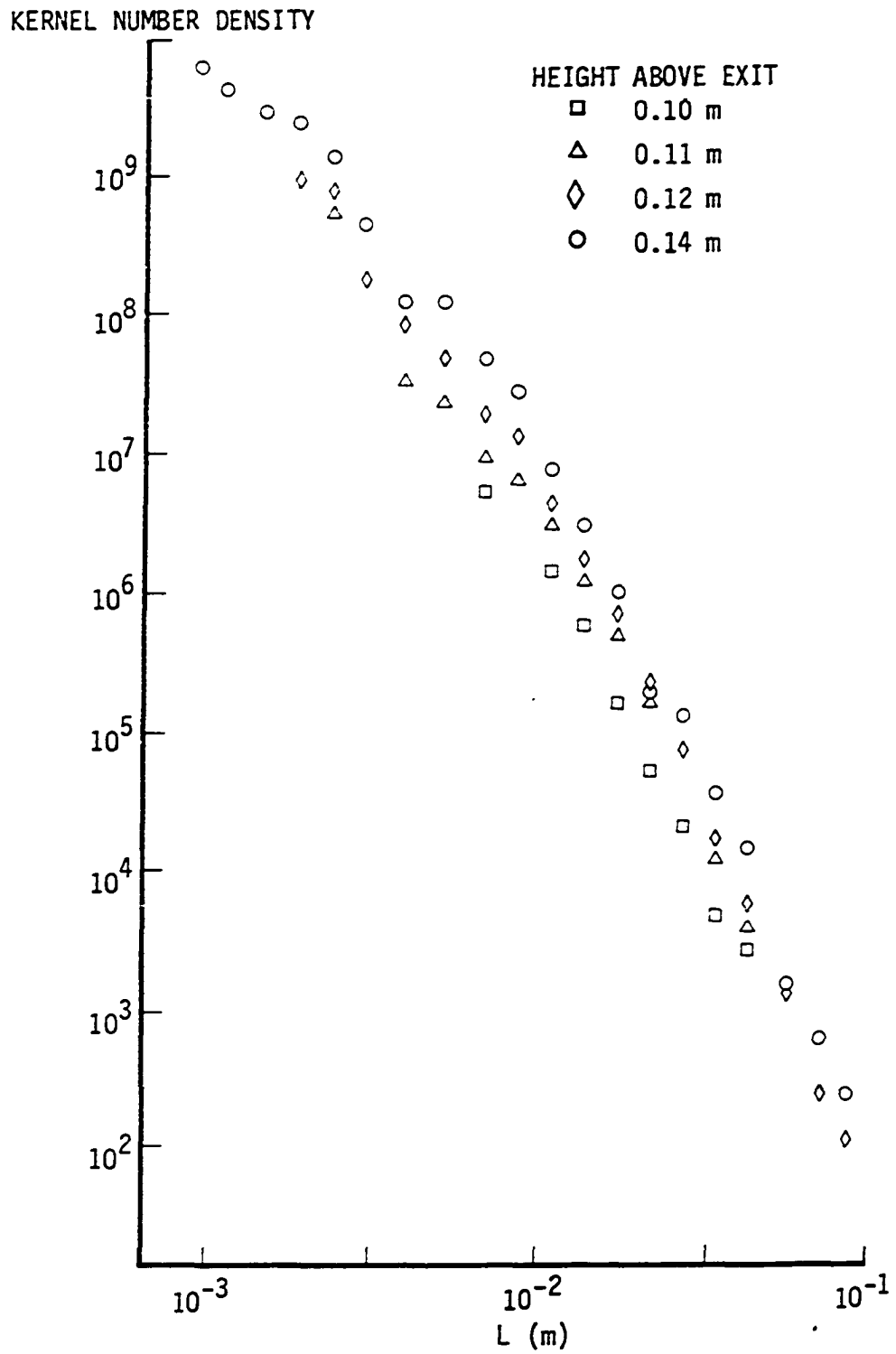


Figure V-26-A. Kernel Number Density Distribution as a Function of Size for the Growth Region of the 4.5 m/s Approach Speed Flame.

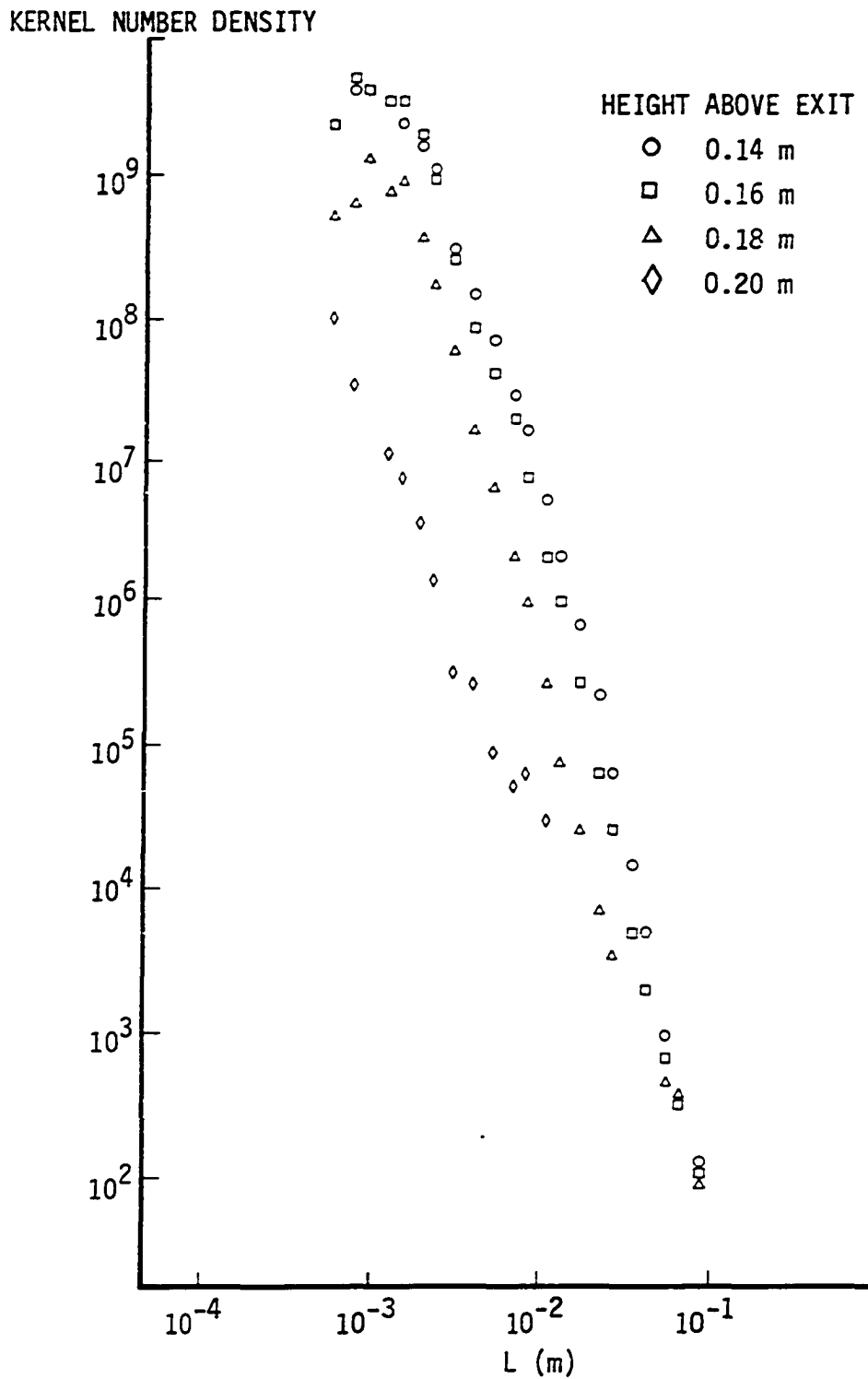


Figure V-26-B. Kernel Number Density Distribution as a Function of Size for the Decay Region of the 4.5 m/s Approach Speed Flame.

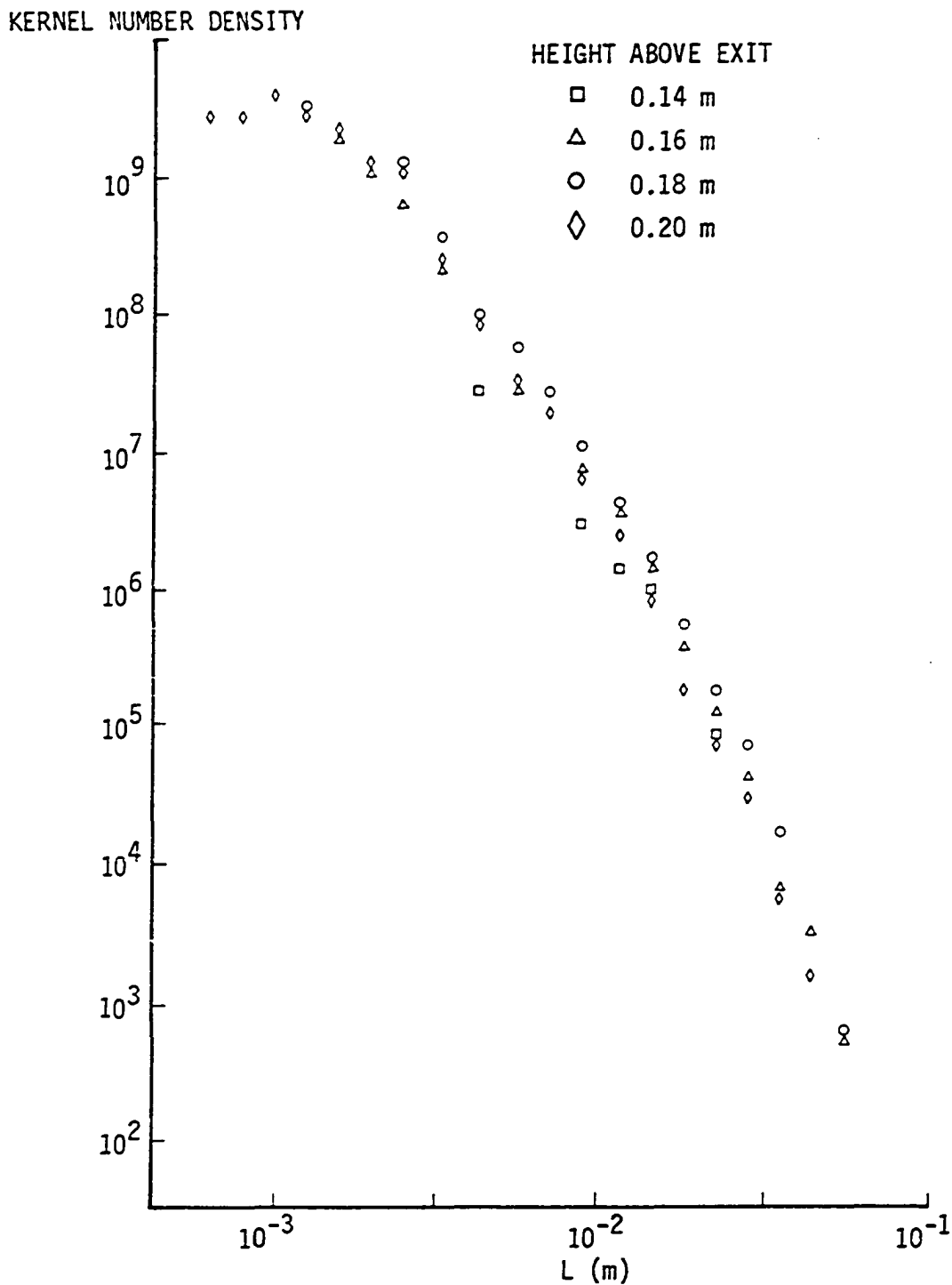


Figure V-26-C. Kernel Number Density Distribution as a Function of Size for the Growth Region of the 8 m/s Approach Speed Flame.

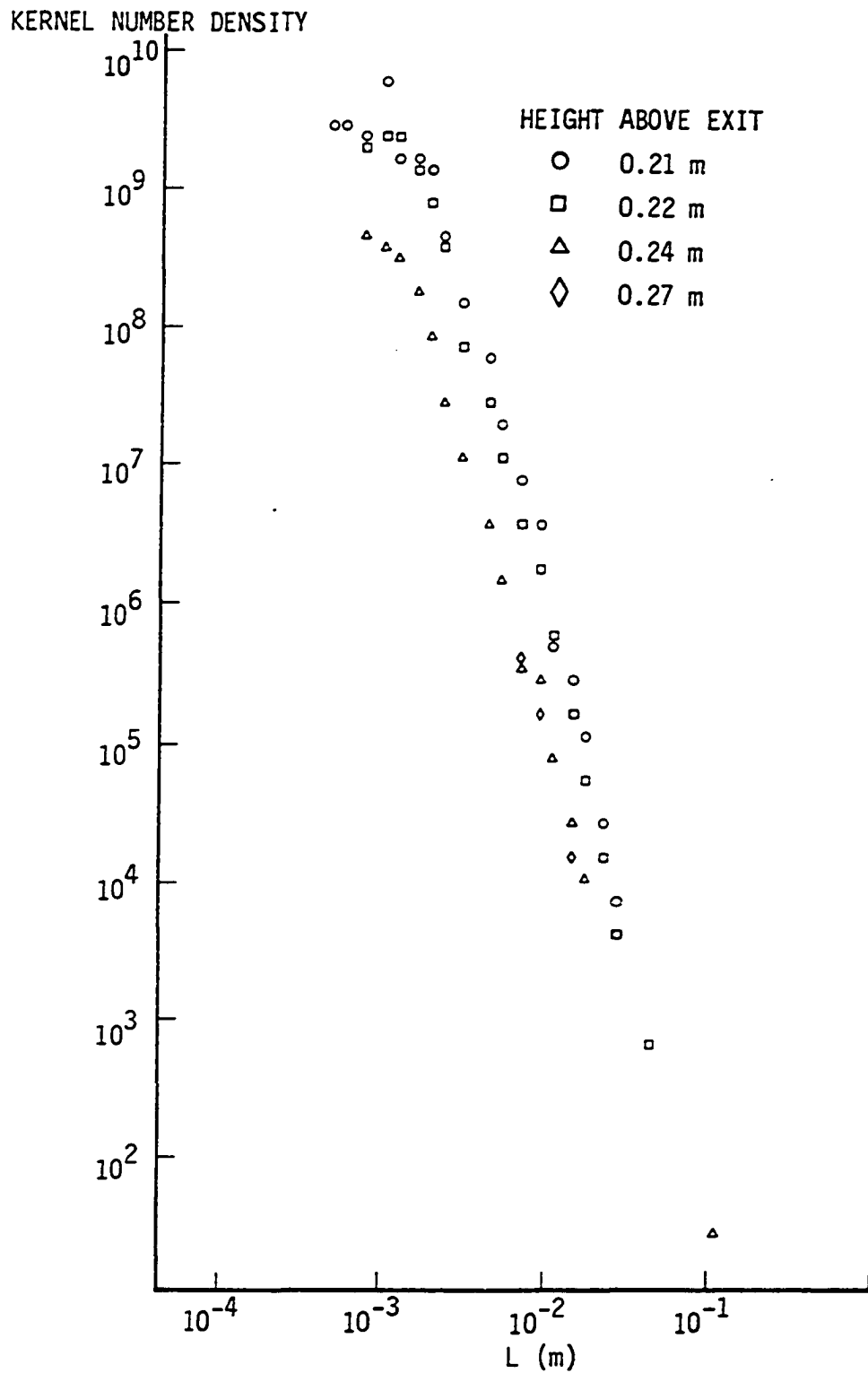


Figure V-26-D. Kernel Number Density Distribution as a Function of Size for the Decay Region of the 8 m/s Approach Speed Flame.

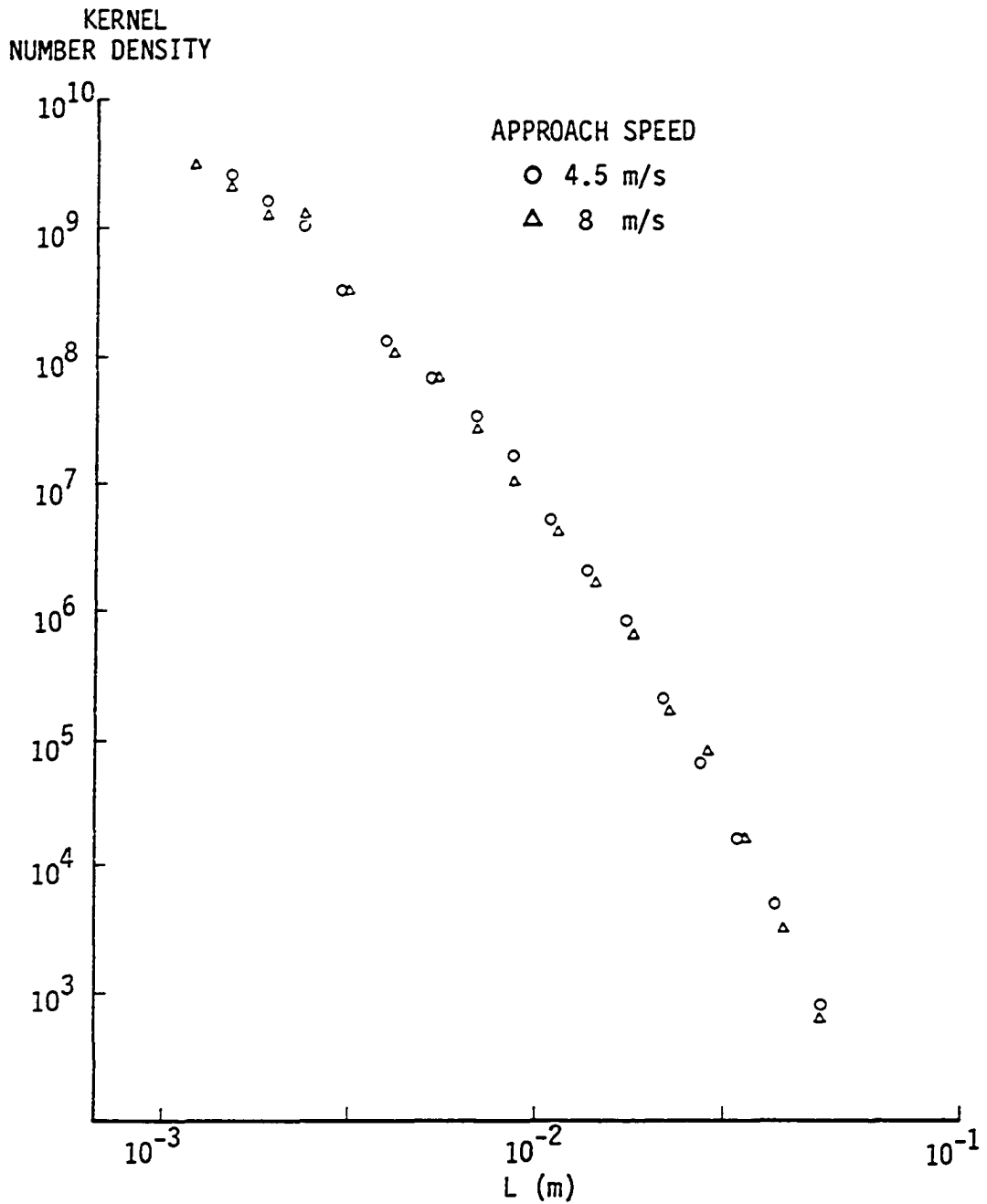


Figure V-27. Kernel Density Distributions as a Function of Kernel Diameter for the Most Active Region of the 4.5 m/s and 8 m/s Approach Speed Flames.

with an equation of the form

$$K(L) = AL^{-B} \quad (V-9)$$

The constants A and - B and the correlation coefficients are summarized in Table V-2 for each case. The volume fraction, $V_f(z)$, is included in Table V-2 for convenience. The volume fraction is explained in a following paragraph.

According to the simple model, most of the kernels would be small in the initial stages of combustion. The number density would decrease rapidly with increasing size. The rate at which the number density decreased as size increased would be less as more kernels grow to larger sizes. As kernels grow together, leaving only small irregular-shaped unburned pockets, the trend would reverse. With increasingly few large kernels remaining in the upper region, the decrease in density with increasing size would be more rapid. The correlation levels were too low to accurately assess trends in the final stages. The parameter - B from Table V-2 is plotted in Figure V-28 as a function of height for the 4.5 m/s flame. The data show the trends expected. This was not proof of the model but was supportive of its applicability.

The kernel density distribution times the volume of the kernel integrated over the size L gives the volume fraction occupied by the kernels. This number $V_f(z)$ can be calculated analytically based on the curve fit for density.

Table V-2. Summary of Kernel number density parameters

4.5 m/s approach speed flame				
Height	A	- B	C'_{ed}	$V_f(H_z)$
0.10	0.00983	4.11	0.994	0.026
0.11	0.457	3.40	0.989	0.041
0.12	0.709	3.40	0.988	0.063
0.14	0.467	3.63	0.982	0.106
0.14	0.257	3.66	0.986	0.076
0.16	0.0162	4.09	0.991	0.039
0.18	0.0007	4.34	0.995	0.006
0.20	0.149	2.63	0.994	0.0005
8 m/s approach speed flame				
Height	A	- B	C'_{ed}	$V_f(H_z)$
0.12	0.367	3.34	0.975	0.025
0.15	0.250	3.65	0.990	0.072
0.15	0.178	3.65	0.989	0.050
0.18	0.247	4.02	0.990	0.041
0.21	0.0019	4.38	0.991	0.020
0.22	0.00122	4.36	0.994	0.011
0.24	0.00131	3.96	0.995	0.002
0.27	_a	_a	_a	_a

^aInsufficient data.

-B FROM EQUATION V-9

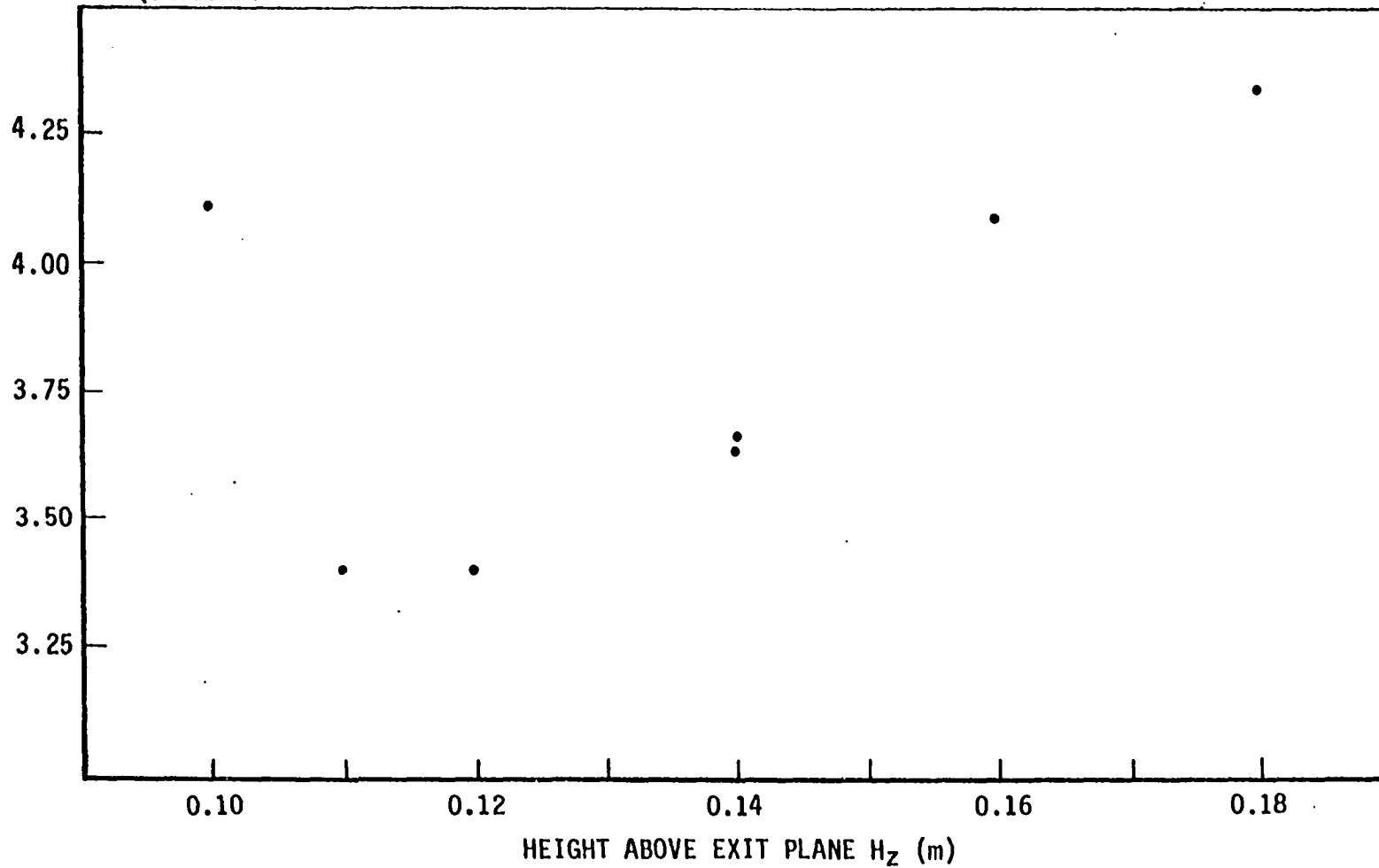


Figure V-28. Exponent -B from the Curve Fit of the Kernel Density Distribution as a Function of Kernel Diameter for Heights Where Data Were Obtained in the 4.5 m/s Approach Speed Flame.

$$\begin{aligned}
 V_f(H_2) &= \frac{\pi}{6} \int_{L_{\min}}^{L_{\max}} K(L)L^3 dL \\
 &= \frac{A\pi}{6} \frac{L^{-B+4}}{-B+4} \Bigg|_{L=L_{\min}}^{L=L_{\max}}
 \end{aligned}
 \tag{V-10}$$

where A and B are the constants listed in Table V-2. The volume fraction is tabulated in Table V-2 for each flame position.

The kernel passage rate was multiplied by the kernel size and summed to find the activity fraction. The kernel density was multiplied by the volume of the kernels and integrated to find the volume fraction. The density was derived from the passage rate using only scaling fractions and geometric parameters. Both are normalized. The explanation of the magnitude of either volume fraction or activity fraction is equally applicable to the other. The volume fraction has a maximum value of less than 0.25. This is probably somewhat less than the true value for the following reasons. A value of 0.324 E-03 was assigned to Δn . Δn is one of the normalizing parameters in the simple model signal. In the correlation, the signals are multiplied so the influence of Δn is second order in all model based statistical analysis. The value of Δn used corresponds to the change in refractive index from reactants at laboratory temperature and pressure to the refractive index of ideal products at the same pressure but at the adiabatic flame temperature. Heat transfer from the flame to the unburned reactants undoubtedly occurs, raising the temperature of the reactants before reaction. The change in refractive index was insensitive to changes of

several hundred degrees in the final temperature because the assumed final temperature was 2350°K. The change in refractive index is strongly dependent on the initial low temperature of about 294°K. A change of only 100°K in the reactant temperature would change the refractive index by more than 30%. The Δn could be too large by a factor of 1.5 due to the heating of the reactants alone. The volume fraction could easily increase by a factor of 2 if the proper Δn were known. The peak value would then be less than 0.5. This is entirely plausible. Reaction is known to continue well past the level of the peak value so the reaction was not complete at that point. That meant that the true maximum volume fraction was less than one. In the terminal stages of combustion, the remaining unburned pockets are undoubtedly at a much higher temperature than the initial temperature and due to heat losses, the surroundings are much below the adiabatic flame temperature. The assumed value of Δn could easily be too large by a factor of 2 in the upper region of the flames. Since the volume fraction is less than 0.05 in this region, a factor of 4 would not give unrealistic values.

The effective beam half width was assumed to be 0.9 mm. The signal level was a strong function of size for small size kernels. Any difference between the true effective beam size and the assumed size would be reflected in the data. The value used was the best available estimate, so no assessment of the error it may have caused can be made.

The simple model was used throughout the flame. In the latter stages of combustion, the signals were produced by the converging combustion of the pockets of gas which remained after the kernels grew

together. As discussed above, the value of Δn in this region was undoubtedly less than the assumed value. The geometry was probably not spherical so the shapes and magnitudes of the signals were not as predicted by the simple model. The duration of the signal was still indicative of the size of the pockets so the frequency to size correspondence was mostly preserved. The model was less accurate in the upper part of the flame but it was not totally inappropriate. Information necessary to form a better model was not available. The character of the latter stages of the combustion was determined by the initial stages and was of less interest from the standpoint of the fluid mechanics of turbulent combustion. Little effort was dedicated to modeling the latter stages for these reasons.

F. Concluding Flame Signal Observations

1. Off centerline observations

All statistical data discussed to this point were recorded on the burner centerline. In the preliminary stages of the study off centerline data were analyzed. The beams were displaced equal distances from the centerline so that their paths through the flame region would be statistically identical. The spectra were reduced in the same manner as the centerline spectra. The results indicated that moving the beam intersection away from the centerline in the active region of the flame produced the same kinds of changes as moving downstream on the centerline. This was expected since the combustion begins at a lower height off centerline than on centerline. Sufficiently detailed analysis may

have yielded some relationship among flame angle, off-center distance, downstream distance, and conceivably other parameters. The analysis was not pursued for the following reasons: (1) the observed signal to noise ratio was worse for an off-center beam intersection than for a center-line intersection because both beams passed through regions of more intense reaction than the region of their intersection. The required correlation time would increase and the uncertainty would be larger. The same was true in the growth regions of the flames. (2) A mean shear was present off centerline. The mean shear was zero on the centerline. The turbulent intensity was relatively uniform in the center of the flow but was nonuniform in the shear layer. These two flow field differences would have had some unknown but possibly significant effect on the geometry of the flame front. The effect of the mean curvature of the flame front would be greatest in the off-center region.

The resolution limit of the crossed-beam Schlieren system was determined by the size of the beams. The smallest kernel physically possible was probably comparable to the quenching distance. The beams were much larger than the quenching distance. Practically, this meant that the breakup of the flame front could not be studied.

2. Kernels outside the model size range

Many of the plots presented in this chapter included data from kernel sizes comparable to the beam diameters. There are many possible sources of these data. First, the data could have been the response of the crossed-beam Schlieren system to kernels of small sizes. A second source of the signals corresponding to the small sizes was the

response of the instrument to off-center interactions of kernels of larger sizes. A kernel can produce a signal whose characteristic size (or wavelength) was any size less than or equal to its true size. This is explained more completely in the Appendix. A third possibility was that the high frequency signals were the higher harmonics of the fundamental frequency of a larger kernel. Another likely source of small size signals is the response of the finite beam to a flame front which is smaller than the beam diameter. In any case, the signals were generated by disturbances smaller than the minimum size which could be resolved by the system.

A number of the plots also include data corresponding to sizes larger than the diameter of the burner. Flame kernels larger than half the diameter of the burner are unlikely. The larger size (lower frequency) signals are believed to be due to the billowing of the heated air at the periphery of the flame. This billowing is obvious in Figure V-21.

G. Data Uncertainty

1. Flow system uncertainty

The flow velocities were monitored with rotometers in each line. The air flow meter was calibrated with a hot wire anemometer before the study.

The propane flow meter was calibrated for oxygen flow. The calibration was converted according to standard procedures. Both flow meters were monitored continuously during all data acquisition. The maximum

uncertainty in the flow velocities was about 2%. This was also the maximum variation during any session since the 2% was the limit of the accuracy of reading of the scales. The two velocities were sufficiently different that a variation of 2% was not significant. The variation of the velocity profiles was more than the uncertainty in the velocity in both cases. The turbulence level was nominally 4% in both cases. The variation in intensity is shown in Figure IV-12. The purpose of the study was the effect of turbulence on a flame rather than the variation of the effect of turbulence as scale length or intensity were varied. The variation shown in Figure IV-12 was not critical.

The equivalence ratio was nominally one. The maximum variation was 4% since it was determined by the flow velocities. The 4% uncertainty in equivalence ratio was not detrimental since most flame characteristics are slowly varying at stoichiometric composition. No study was made of the effect of varying the equivalence ratio.

2. Instrumentation uncertainties

The laser beams were individually positioned for each case. The locations of the beam centers were known with a maximum uncertainty of less than 1 mm without the flame. When the beams were set to intersect, the centers were coincident with a uncertainty of less than 1 mm. The beams were also positioned within 1 mm of the burner axis. The beams were not repositioned to correct the displacement caused by the mean deflection with the flame on since the mean deflection was much smaller than the root mean square deflection. The fluctuating beam

deflections made it impossible to maintain the intersection of the beams at the desired height on the centerline. The measurements were made in increments of 1 cm in the streamwise direction so an uncertainty of 1 mm in position should have little effect on the analysis. This was shown by the slow continuous variation of the reduced data throughout the active region of the flame.

The detector responses were linear with amplitude. Any deviation from linearity was undetectable. No systematic variation in laser power was detected during the study and it was assumed that the beam diameters and divergences were also constant. The effects of any undetected laser power variation and the effect of the decrease of detector battery voltage were eliminated by the spot calibration which was performed each time data was recorded.

The tape recorder, when operating properly, faithfully reproduced the input signals. The erase mode reduced the level of the signals on the tape more than 50 dB so reuse of the tape produced no uncertainty in the data.

The filters as used had a nominal insertion loss of 6 dB. This loss was compensated for in the data analysis. The claimed accuracy of the frequency settings was 5%. This uncertainty contributed to uncertainty in the data in two ways. The first source of error was a result of the division of the covariances by the bandwidth of the filters. The bandwidth of the filters was proportional to the frequency so any error in frequency was reflected in the filter bandwidth. In addition, the data would be analyzed at the wrong value of the independent variable (frequency or wavenumber).

The second source of uncertainty due to errors in the frequency settings was a result of the variation in bandwidth and insertion loss which accompanies unequal high pass and low pass frequency settings. An error of 5% in each setting causes an error of 20% in the insertion loss and an error of 45% in the bandwidth. The two errors occur together so the maximum error was 75%. Coincident errors of the maximum amount in opposite directions as would be required to produce an error of 75% were unlikely. A more realistic estimate of the total uncertainty due to filter settings was 25%. Any operator error adds to the error produced by the uncertainty of filter settings. The procedure adopted in this study minimizes the operator error. The filter dials were set at the desired frequency once and the decade multipliers were switched to filter the signals at the set frequency in each decade. This procedure would also emphasize the error at any set frequency since the error would be present at the particular dial setting in each decade. This would make the error easier to detect.

3. Analysis uncertainties

The correlator was repaired and calibrated prior to final data reduction. The only error assumed due to the correlator was a result of digitizing the signals. The least count of the correlator output was 0.005 volts. The smallest reading observed was greater than 0.06 volts. The maximum uncertainty was 8%.

The period of analysis of continuous data should be many times the period of the slowest varying component of interest. The statistical uncertainty of results decreases as the analysis period

increases. The data analyzed in this study were continuous. The filtered data which were correlated were not continuous in the normal sense. The filtered data contained periods of no signal. The period of analysis required for valid statistical results was not determined by the period of the filtered signal but rather the period of the occurrence of the signal. The required period was estimated by observing the rate of growth of the covariance. The analyzer provided a means of summing individual covariance calculations. The covariances used in analysis were obtained by averaging sufficient individual covariance calculations. The covariances used in analysis were obtained by averaging sufficient individual covariances that the effect of the intermittent nature of the signal was reduced. The statistical uncertainty was difficult to determine due to the nature of the signals. It was believed to be less than a factor of two.

The computer programs written to calculate the final results from the data would not create random errors. Any errors would be consistent systematic errors. All parts of the programs were checked by comparison with manual calculations. Errors found were corrected prior to final data reduction. The data used as input to the programs were checked. No error was attributed to the machine calculations.

The errors of analysis due to deficiencies of the simple model have been discussed. No estimate can be made of the errors involved because no better or more accurate model exists.

The largest sources of uncertainty were the filters and the correlation. The maximum uncertainty in the reported data is believed to be less than a factor of three. A detailed analysis was repeated at

one location in each flame. The volume fractions and activity fractions which represent a total signal analysis differed by less than a factor of two in corresponding analyses. A factor of two at any point may appear large but the data to which it applies vary over about seven orders of magnitude (see for instance Figure V-27) so the factor of two is less than 5%. Reduction of this would require better equipment and much more analysis time. The effort involved could be better spent in additional original analysis rather than more precise analysis of the present data.

VI. SUMMARY, CONCLUSIONS, AND RECOMMENDATIONS

A. Summary

1. Instrument improvement

The instrumentation system used in this study was similar to the systems used by Wilson and Damkevala (38), Martin (39), and Parks (40). The instrument cage used in this study was designed to allow greater ranges of observations than had previously been possible. The compactness, ease of precision adjustment, and rigidity of the cage were beneficial in this study.

The linear biaxial crystals which replaced the photodiodes previously used were the most significant improvement. They replaced the converging lens, knife edge, and photodiode in each assembly. The linear range was extended by a factor of more than 20. This allowed the signal to be linearly related to beam deflection. The biaxial crystals allowed simultaneous observation of the beam deflection in two orthogonal directions. This was a major factor in the verification of predicted signal shapes.

The major disadvantages were reduced sensitivity and reduced allowable light intensity. The sensitivity was reduced from nominally 1100 v/m to 18 v/m. The observed beam deflections were large enough to eliminate any problems which might have been anticipated due to the reduced sensitivity. The reduced maximum allowable light intensity was a more serious problem. Lasers with peak intensities below the maximum allowable intensity were not commercially available. This necessitated external attenuation of the beams. All attenuators

tested increased beam diameter and divergence. This increased the resolution limit and reduced the signal level produced.

The advantages of the extended linear range and biaxial sensitivity far outweigh the disadvantages. The biaxial crystals should be given first consideration in all future studies.

Low pass filters were added to the laser power supplies which significantly reduced the common 120 Hz noise signal in the lasers. With the added filters, the laser noise was acceptable in all cases.

2. Model development and verification

A physical model was developed to describe the reaction zone. A simplified mathematical model was derived from the physical model. The salient features of the simple model are reproduced in the Appendix. The geometry of the physical model was confirmed by comparison of the model predicted signals with the flame generated signals. The motion of the flame front was determined by three separate tests. They were comparison of initial beam deflection, Abel inversion of flame generated signals, and observation of kernel growth. The physical model was a closed expanding flame surface. The simple model was a spherical expanding flame kernel.

B. Conclusions

The instrumentation system was well suited to turbulent flame studies. The improvements enhanced its capabilities and versatility.

Development, verification, and subsequent use of a physical model

of the flame region were the most significant accomplishment of this study. The limitations of the existing model were determined.

C. Recommendations

1. Instrumentation improvement

Light beams of smaller diameter should be used in future studies. This would allow accurate observation of smaller disturbances in the flame. Ultimately, the breakup of the laminar flame front could be observed. Any decrease in beam diameter would increase the signal level. Beams with uniform intensity distributions would simplify the modeling of the beam interaction with the kernel.

Biaxial crystals capable of withstanding higher peak light intensities should be sought. Their advantages would be higher signal levels and possibly elimination of the necessity of beam attenuation. The beam should be attenuated after it emerges from the flame if crystals compatible with available laser intensity cannot be found. The ideal attenuator would transmit only the laser light. If the ideal attenuators can be found, the total light power incident could be monitored. The voltage difference proportional to beam displacement could be divided by the voltage sum which is proportional to incident power. This normalization would eliminate the effect of power fluctuations on the signal. Tests in the present study indicated that about 30% of the total light power incident was flame generated. The flame generated light was uniformly distributed. The remaining 70% was the attenuated laser beam. If the flame and laser light were both attenuated at the

crystal face, the contribution by the flame to the total would be less than 3%. The signal could be normalized with little error under these conditions. Equipment to perform the addition and division was not available for this study but can be purchased for subsequent studies.

Mounting the detectors farther from the burner centerline would increase the signal level and reduce the contribution of the flame to the total light power incident on the crystals. The resulting apparatus would be less compact and more susceptible to vibrations.

The amplifiers, correlator, and tape recorder were adequate. Any means available to speed the spectral analysis would allow more flame conditions to be studied. The only part of the data analysis system which caused concern were the filters. The uncertainty introduced by the filters was discussed in Section V-F-2. The present filters required setting of both high pass and low pass frequencies with no certainty that the two were the same. Band pass filters should be obtained so that only one adjustment is required. Such filters could be calibrated, reducing the uncertainty in the results.

The performance of the flow system was satisfactory. No recommendations for improvement are made.

2. Recommendations for future research

If light sources of small enough size can be obtained, the flame front breakup could be studied. The effect of scale length and turbulent intensity could be determined and a physical model developed to describe the flame front breakup. Such a model would be invaluable in future

combustion system design. The effect of heat release rate on the fluid mechanics of combustion could be determined by studying different reactants.

The limitations of the physical model derived for this study could be investigated. The effects of slightly nonspherical geometries could be determined, for instance. A more productive endeavor might be to determine the effect of noncentral beam kernel interactions on the cross covariances. The basis of this is included in the Appendix for the simple model used in this study.

The most challenging area for future work would be to develop a theory of turbulent flame structure leading from a laminar flame to the type reaction region observed in this study. Such a theory could undoubtedly be verified by experiment and used to guide future experiments.

VII. REFERENCES

1. G. Damkohler. "The effect of turbulence on the flame velocity in gas mixtures." NACA TM 1112, 1947.
2. K. I. Shchelkin. "On combustion in a turbulent flow." NACA TM 1110, 1947.
3. B. Karlovitz, D. W. Dennison, Jr., D. H. Knapschafer, and F. C. Wells. "Studies on turbulent flames." Fourth Symposium (International) on Combustion. Baltimore: The Williams and Wilkins Co., 1953.
4. K. Wohl, L. Shore, H. Von Rosenberg, and C. W. Weil. Fourth Symposium (International) on Combustion. Baltimore: The Williams and Wilkins Co., 1953.
5. H. C. Hottel, G. C. Williams, and R. S. Levine. "The influence of isotropic turbulence on flame propagation." Fourth Symposium (International) on Combustion. Baltimore: The Williams and Wilkins Co., 1953.
6. A. C. Scurlock, and J. H. Grover. "Propagation of turbulent flames." Fourth Symposium (International) on Combustion. Baltimore: The Williams and Wilkins Co., 1953.
7. F. W. Bowditch. "Some effects of turbulence on combustion." Fourth Symposium (International) on Combustion. Baltimore: The Williams and Wilkins Co., 1953.
8. D. R. Ballal and A. H. LeFebvre. "Turbulence effects on enclosed flames." ACTA Astronautica, 1 (1974), 471-483.
9. G. E. Andrews, D. Bradley, and S. B. Lwakabamba. "Measurement of turbulent burning velocity for large turbulent Reynolds numbers." Fifteenth Symposium (International) on Combustion. Pittsburgh: The Combustion Institute, 1974.
10. G. E. Andrews, D. Bradley, and S. B. Lwakabamba. "Turbulence and turbulent flame propagation - A critical appraisal." Combustion and Flame, 24 (1975), 285-304.
11. V. Sriramulu, K. S. Padiyar, and U. S. P. Shet. "Correlation of turbulent burning velocity data for enclosed flames." Combustion Science and Technology, 19 (1978), 71-72.
12. V. N. Vilyunov. "Critical description of turbulent combustion rate." Combustion, Explosion, and Shock Waves, 11 (1975), 43-47.

13. V. R. Kuznetsov. "Certain peculiarities of movement of flame fronts in a turbulent flow of homogeneous fuel mixtures." Combustion, Explosion, and Shock Waves, 11 (1975), 487-493.
14. M. Summerfield, S. H. Reiter, V. Kebely, and R. W. Mascolo. "The physical structure of turbulent flames." Jet Propulsion, 24, No. 4 (1954), 254-255.
15. M. Summerfield, S. H. Reiter, V. Kebely, and R. W. Mascolo. "The structure and propagation mechanism of turbulent flames in high speed flow." Jet Propulsion, 25, No. 8 (1955), 377-384.
16. N. M. Howe, Jr., and C. W. Shipman. "A tentative model for rates of combustion in confined turbulent flames." Tenth Symposium (International) on Combustion. Pittsburgh: The Combustion Institute, 1965.
17. P. Basu and D. Bhaduri. "Structure of premixed turbulent flame." Combustion and Flame, 18 (1972), 303-305.
18. P. A. Libby. "On turbulent flows with fast chemical reactions. Part I: The closure problem." Combustion Science and Technology, 6 (1972), 23-28.
19. C. H. Gibson and P. A. Libby. "On turbulent flows with fast chemical reactions. Part II: The distribution of reactants and products near a reacting surface." Combustion Science and Technology, 6 (1972), 29-35.
20. D. B. Spalding. "Mathematical models of turbulent flames; a review." Combustion Science and Technology, 13 (1972), 3-25.
21. D. B. Spalding. "Mixing and chemical reactions in steady confined turbulent flames." Thirteenth Symposium (International) on Combustion. Pittsburgh: The Combustion Institute, 1971.
22. K. N. C. Bray and J. B. Moss. "A unified statistical model of the premixed turbulent flame." Acta Astronautica, 4 (1977), 291-319.
23. M. Champion, K. N. C. Bray, and J. B. Moss. "The turbulent combustion of a propane air mixture." Acta Astronautica, 5 (1978), 1063-1077.
24. F. C. Lockwood and I. E. A. Megahed. "Extinction in turbulent reacting flows." Combustion Science and Technology, 19 (1978), 77-80.

25. F. C. Lockwood. "The modeling of turbulent premixed and diffusion combustion in the computation of engineering flows." Combustion and Flame, 29 (1977), 111-122.
26. S. B. Pope. "The probability approach to modelling of turbulent reacting flows." Combustion and Flame, 27 (1976), 299-312.
27. S. B. Pope. "The implications of the probability approach for turbulent combustion models." Combustion and Flame, 29 (1977), 235-246.
28. K. H. Parker and O. Guillon. "Local measurements in a turbulent flame by hot wire anemometry." Thirteenth Symposium (International) on Combustion. Pittsburgh: The Combustion Institute, 1971.
29. C. M. Ho, K. Jakus, and K. H. Parker. "Temperature Fluctuations in a turbulent flame." Combustion and Flame, 27 (1976), 113-123.
30. F. E. Bundy and H. M. Strong. "Measurements of flame temperature, pressure, and velocity." High Speed Aerodynamics and Jet Propulsion. Princeton, N.J.: Princeton University Press, 1954.
31. F. A. Williams. "Turbulent flames." Experimental Methods in Combustion Research. New York: Pergamon Press, 1962.
32. R. M. Fristrom. "Chemical evolution of the combustion process." Experimental Methods in Combustion Research. New York: Pergamon Press, 1961.
33. G. H. Dieke. "Spectroscopy of combustion." High Speed Aerodynamics and Jet Propulsion. Princeton, N.J.: Princeton University Press, 1954.
34. W. T. Reid. "Flame photography." High Speed Aerodynamics and Jet Propulsion. Princeton, N.J.: Princeton University Press, 1954. 389-405.
35. F. J. Weinberg. Optics of Flames. London: Butterworths, 1963.
36. J. Grummer, J. M. Singer, J. K. Richmond, and J. R. Oxendine. "Photographic studies of turbulent flames." Industrial and Engineering Chemistry, 49 (1957), 305-312.
37. M. J. Fisher and F. R. Krause. "The crossed-beam correlation technique." Journal of Fluid Mechanics, 28 (1967), 705-717.

38. L. N. Wilson and R. J. Damkevala. "Statistical properties of turbulent density fluctuations." Journal of Fluid Mechanics, 43 (1970), 291-303.
39. R. A. Martin. "Studies of scalar turbulence in air downstream of a heated grid." Ph.D. dissertation, Iowa State University, Ames, Iowa, 1975.
40. F. B. Parks. "An optical cross correlation technique for turbulent density measurements in flames." Ph.D. dissertation, University of Missouri, Columbia, Missouri, 1973.
41. B. Lewis and G. vonElbe. Combustion, Flames, and Explosions of Gases. New York: Academic Press, 1951.
42. J. N. Bradley. Flame and Combustion Phenomenon. London: Methuen and Co., 1969.
43. A. G. Gaydon and H. G. Wolfhard. Flames, Their Structure, Radiation, and Temperature. London: Chapman and Hall Ltd., 1953.
44. R. Strehlow. Fundamentals of Combustion. Scranton, Pa.: International Text Book Co., 1968.
45. A. M. Kanury. Introduction to Combustion Phenomenon. New York: Gordon and Breach Science Publishers, 1975.
46. I. Glassman. Combustion. New York: Academic Press, 1977.
47. R. M. Fristrom and A. A. Westenberg. Flame Structure. New York: McGraw Hill, 1965.
48. J. S. Bendat and A. G. Piersol. Measurement and Analysis of Random Data. New York: John Wiley and Sons, Inc., 1966.
49. J. O. Hinze. Turbulence. New York: McGraw Hill, 1959.
50. A. Ballantyne and K. N. C. Bray. "Investigation into the structure of jet diffusion flames using time resolved optical measuring techniques." Sixteenth Symposium (International) on Combustion. Pittsburgh: The Combustion Institute, 1977.
51. K. Yosida. Lectures on Differential and Integral Equations. New York: Interscience Publishers, Inc., 1960.
52. M. P. Freeman and S. Katz. "Determination of a radiance coefficient profile from the observed asymmetric radiance distribution of an optically thin medium." Journal of the Optical Society of America, 53 (1963), 1172-1179.

53. R. South. "An extension to existing methods of determining refractive indices from axisymmetric interferograms." AIAA Journal, 8 (1970), 2057-2059.

VIII. APPENDIX: MATHEMATICAL MODEL

A. Derivation of Mathematical Model

1. Central beam-kernel interaction

The mathematical model was based on the physical model of the flame region. The physical model was a disperse flame with closed flame surfaces. A spherical flame surface was assumed since it was the simplest geometry to model mathematically. The flame front was much thinner than the diameter of the beam and the exact processes occurring in the flame front were unknown. For these reasons, the flame surface was modeled as a discontinuity in refractive index. Initially, only beam-kernel interactions where the center of the beam passed through the center of the sphere were considered. The three-dimensional problem was replaced by a two-dimensional problem. Snell's Law, $n_1 \sin(\alpha_1) = n_2 \sin(\alpha_2)$, was applied at the sphere surface. The geometry and important nomenclature are shown in Figure VIII-1. All deflections were in the plane formed by the ray and the radius vector. The region of the interaction between the entering ray and the circle is shown in Figure VIII-2-A. An expanded view of the entering and exiting ray are shown in Figure VIII-2-B where the entering ray has been reflected about the Z axis for comparison.

$$n_1 \sin(\alpha_1) = n_2 \sin(\alpha_2)$$

$$\sin(\alpha_2) = \frac{n_1}{n_2} \sin(\alpha_1)$$

$$\sin(\alpha_1) = Z/R$$

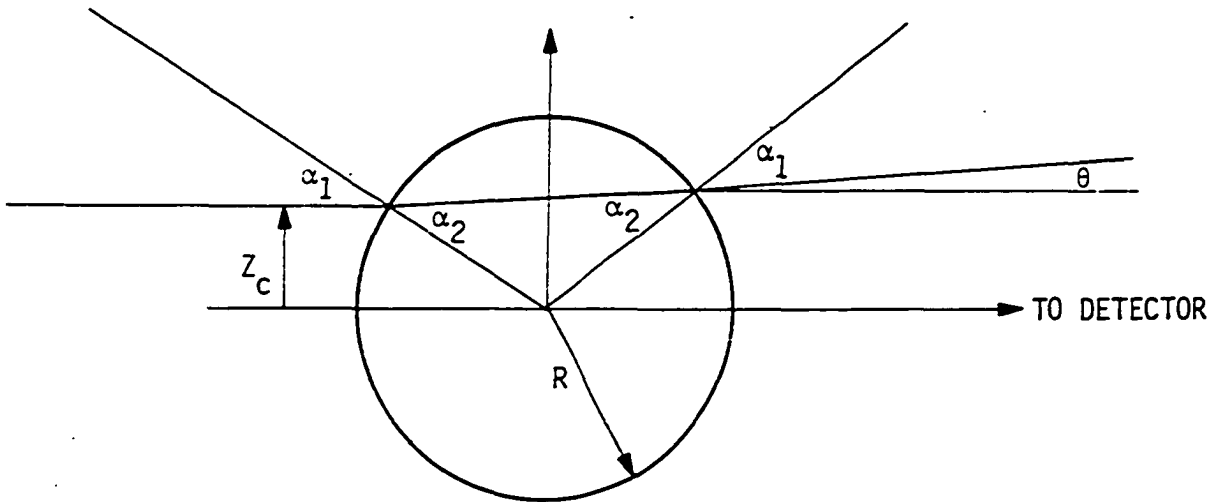


Figure VIII-1. Geometry and Nomenclature of the Mathematical Model of the Burning Kernels.

$$\sin(\alpha_2) = n_1 Z / n_2 R$$

$$\theta = 2(\alpha_2 - \alpha_1) = 2(\sin^{-1}(n_1 Z / n_2 R) - \sin^{-1}(Z/R))$$

$$\cos(\alpha_2) = (n_2 - n_1) Z / (R n_2 \theta / 2)$$

$$\theta = 2 \Delta n Z / (R n_2 \cos(\alpha_2)) \text{ but}$$

$$\cos(\alpha_2) = (R^2 - (\frac{n_1}{n_2} Z)^2)^{1/2} / R \text{ thus}$$

$$\theta = 2 \Delta n Z / (R n_2 (R^2 - (\frac{n_1}{n_2} Z)^2)^{1/2} / R)$$

$$= 2 \Delta n Z / (n_2 R^2 - n_1^2 Z^2)^{1/2}$$

Since $n_1 \sim 1$ and $n_2 \sim 1$

$$\theta = 2 \Delta n Z / (R^2 - Z^2)^{1/2}$$

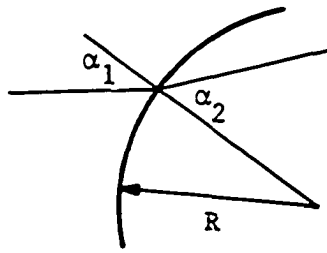


Figure VIII-2-A. Region of Interaction Between the Incoming Ray and The Spherical Kernel.

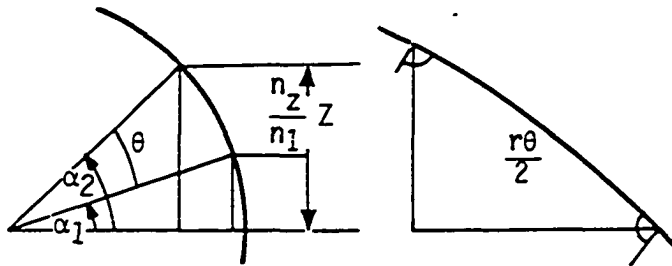


Figure VIII-2-B. Expanded View of the Interactions of the Kernels and the Ray at the Entering and Exiting Surfaces.

n_1 and n_2 were approximately 1 so the deflection at each interface was small. The total deflection, $2(\alpha_2 - \alpha_1)$ was assumed to occur at the center of the sphere.

The quantity of interest was the output of the detector. Assume the sensitivity of the detector to beam displacement was $S'(v/m/mw)$ and the distance from the detector to the burner centerline was $A(m)$. The displacement of the beam was $A \tan(\theta)$. The power of the ray was $I da$ where I was the intensity of the beam in w/m^2 and da was the area of the element of the beam. The signal for a single element of the beam was

$$de = \frac{AS'2\Delta n Z I da}{(R^2 - Z^2)^{1/2}}$$

The signal for the whole beam was the integral of the signal over the area of the beam as indicated in Figure VIII-3. For a Gaussian beam intensity distribution, $I = I_0 e^{-\beta^2/2\sigma^2}$ and the height $Z = Z_c - \beta \sin \phi$. Thus, the signal was

$$de = \frac{AS'2\Delta n(Z_c - \beta \sin \phi) I_0 e^{-\beta^2/2\sigma^2}}{(R^2 - (Z_c - \beta \sin \phi)^2)^{1/2}} \beta d\beta d\phi$$

For $\phi \neq \pi/2$, or $3\pi/2$, the deflection was not entirely in the Z direction. The Z component of the deflection was

$$\frac{Z_c - \beta \sin \phi}{[(Z_c - \beta \sin \phi)^2 + (\beta \cos \phi)^2]^{1/2}}$$

The signal equation was

$$de = \frac{AS'2\Delta n(Z_c - \beta \sin \phi) I_0 e^{-\beta^2/2\sigma^2}}{(R^2 - (Z_c - \beta \sin \phi)^2)^{1/2} [(Z_c - \beta \sin \phi)^2 + (\beta \cos \phi)^2]^{1/2}} \beta d\beta d\phi$$

(VIII-1)

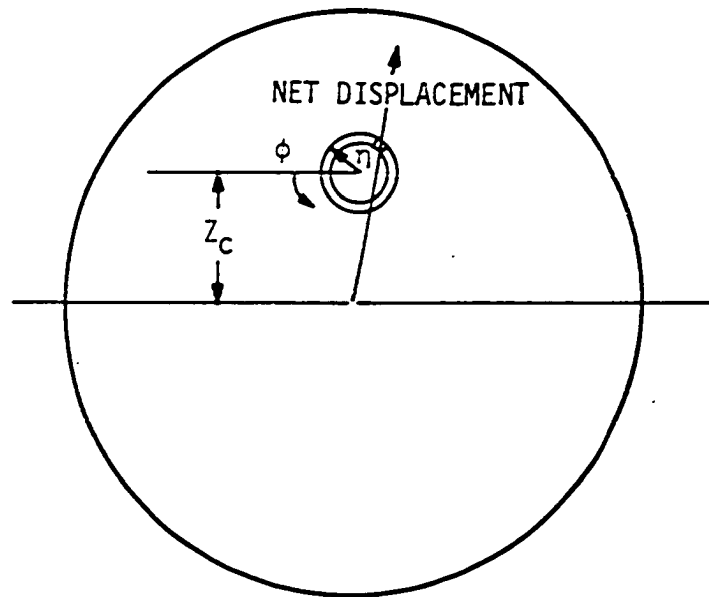


Figure VIII-3. Geometry of the Beam-Kernel Interaction Viewed Along the Beam Axis for a Finite Size Beam.

which cannot be analytically integrated.

Assume the beam to be square of dimension 2δ and of uniform intensity. Consider only spheres with radius much larger than δ .

The signal equation simplifies to

$$de = \frac{I_2 \Delta n S' Z A 2 \delta dZ}{(R^2 - Z^2)^{1/2}} \quad (\text{VIII-2})$$

and

$$e(Z_c) = I_2 \Delta n S' A \delta \int_{Z_c - \delta}^{Z_c + \delta} \frac{Z dZ}{(R^2 - Z^2)^{1/2}} \quad (\text{VIII-3})$$

where $4\delta^2 I_2$ was the power of the beam and $4\delta^2 I_2 S' = S$. Thus,

$$\begin{aligned} e(Z_c) &= \frac{SA \Delta n}{\delta} \int_{Z_c - \delta}^{Z_c + \delta} \frac{Z dZ}{(R^2 - Z^2)^{1/2}} \\ &= SA \Delta n \left(\frac{R}{\delta}\right) \left[\left(1 - \left(\frac{Z_c}{R} - \frac{\delta}{R}\right)^2\right)^{1/2} - \left(1 - \left(\frac{Z_c}{R} + \frac{\delta}{R}\right)^2\right)^{1/2} \right] \end{aligned} \quad (\text{VIII-4})$$

This equation is valid when the entire beam is influenced by the sphere.

When the edge of the beam reaches the edge of the sphere, the upper limit of integration becomes $Z = R$ and

$$e(Z_c) = SA \Delta n \left(\frac{R}{\delta}\right) \left(1 - \left(\frac{Z_c}{R} - \frac{\delta}{R}\right)^2\right)^{1/2} \quad (\text{VIII-5})$$

The assumptions used to derive the simple model were:

1. Uniform spherical region in otherwise uniform surroundings,
2. $n_1, n_2 \sim 1$,
3. Surface of sphere was a discontinuity, and
4. Sphere radius was much larger than beam diameter.

If the assumptions were reasonable, the simple expressions accurately represented the physical process. Assumption 4 was the least rigorously satisfied in the analysis. Equation VIII-1 could not be integrated but an accurate approximation could be achieved numerically. This was done for selected ratios of R/δ . The results showed that the simple model was adequate. Specifically,

1. The computer approximation and the simple model agree well for $R/\delta > 5$,
2. The simple model predicts a peak signal of $e/SA\Delta n = 2(R/\delta - 1)^{1/2}$ and the computer model predicts a peak signal of $e/SA\Delta n = 2(R/\delta)^{1/2}$, and
3. The simple model predicts a peak at $Z = R - \delta$ while the computer model predicts a peak at about $Z = R - \delta/2$.

The simple model was used because its accuracy was believed adequate. A typical calculated signal is shown in Figure VIII-4.

2. Noncentral beam-kernel interaction

For a spherical kernel, the deflection of each ray was in the plane formed by the incoming ray and the radius to the point of intersection. The deflection along the radius vector was resolved into components in the Y and Z directions for noncentral beam-kernel interactions. The signal generated in the streamwise (Z) and one lateral (Y) direction were predicted by the simple model. The streamwise component of the signal was $e_z = (Z/r)e$ and the lateral component was $e_y = (Y/r)e$ where r was the radius to the point of intersection as shown in Figure VIII-5. The streamwise component of the signal was

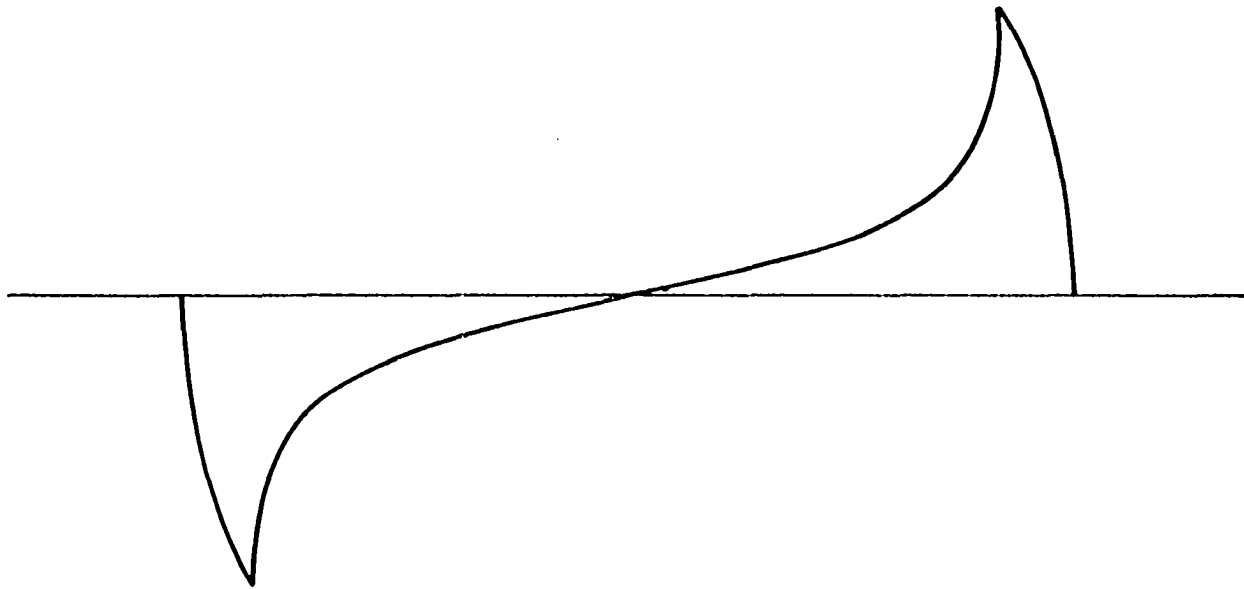


Figure VIII-4. Streamwise Signal Predicted by the Simple Model
for a Representative Ratio of R/δ .

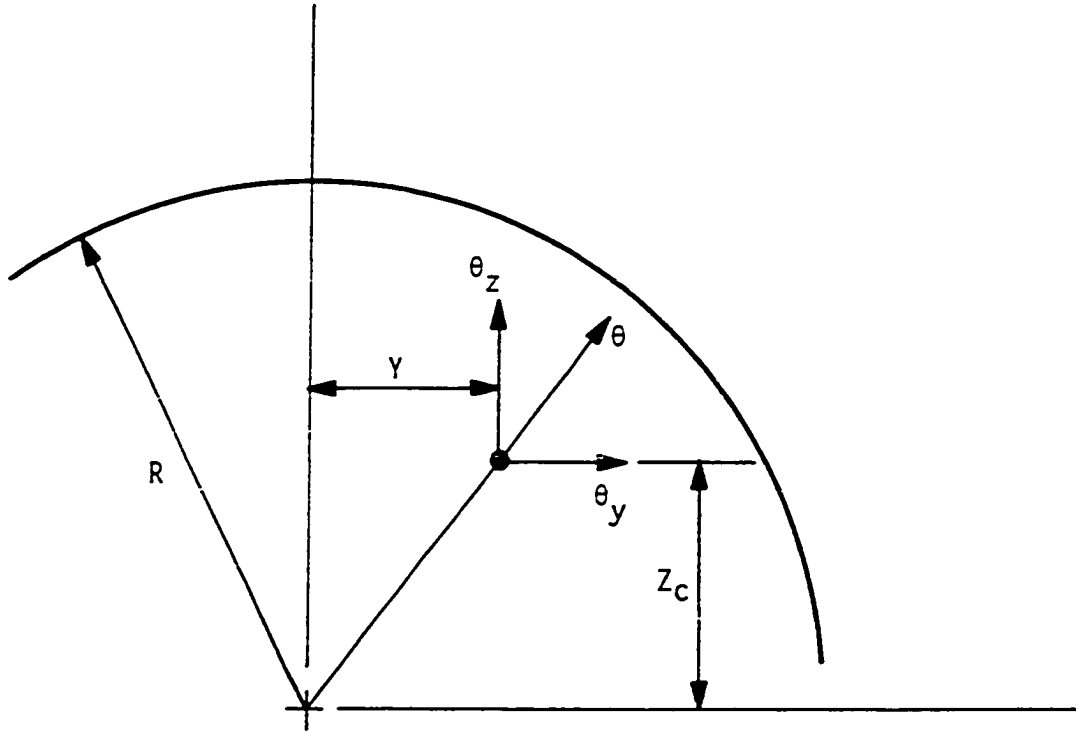


Figure VIII-5. Geometry of Beam-Kernel Interaction of a Non-Central Interaction Viewed Along the Beam Axis.

anti-symmetric about the $Z = 0$ axis and the lateral component was symmetric about the $Z = 0$ axis. The streamwise and lateral components of the signal depicted in Figure VIII-4 are shown in Figure VIII-6 for a lateral displacement of $Y/R = 0.707$. The two signals representing orthogonal components of beam deflection provide much more information about the geometry of the kernels than a single signal.

B. Statistical Analysis of Signals

1. Correlation

The simple model signals were analyzed in a manner comparable to the flame generated data. The first step was the correlation of the signals. The correlation as a function of displacement could be related to a function of delay time by Taylor's hypothesis. This was done to make the correlation and Fourier transforms correspond to the definitions given in Section III-C. The correlation was

$$C'_{aa}(\tau) = \frac{1}{2T} \int_{t-T}^{t+T} e_a(t) e_a(t + \tau) d\tau$$

Although an equation describing the signal was known, the product of two signal equations could not be analytically integrated. The discrete approximation of the covariance was substituted. In this case,

$$C'_{aa}(m\Delta t) = \frac{1}{N} \sum_{i=1}^N e_i e_{i+m} \quad (\text{VIII-6})$$

where the summation is carried out over one complete signal. The

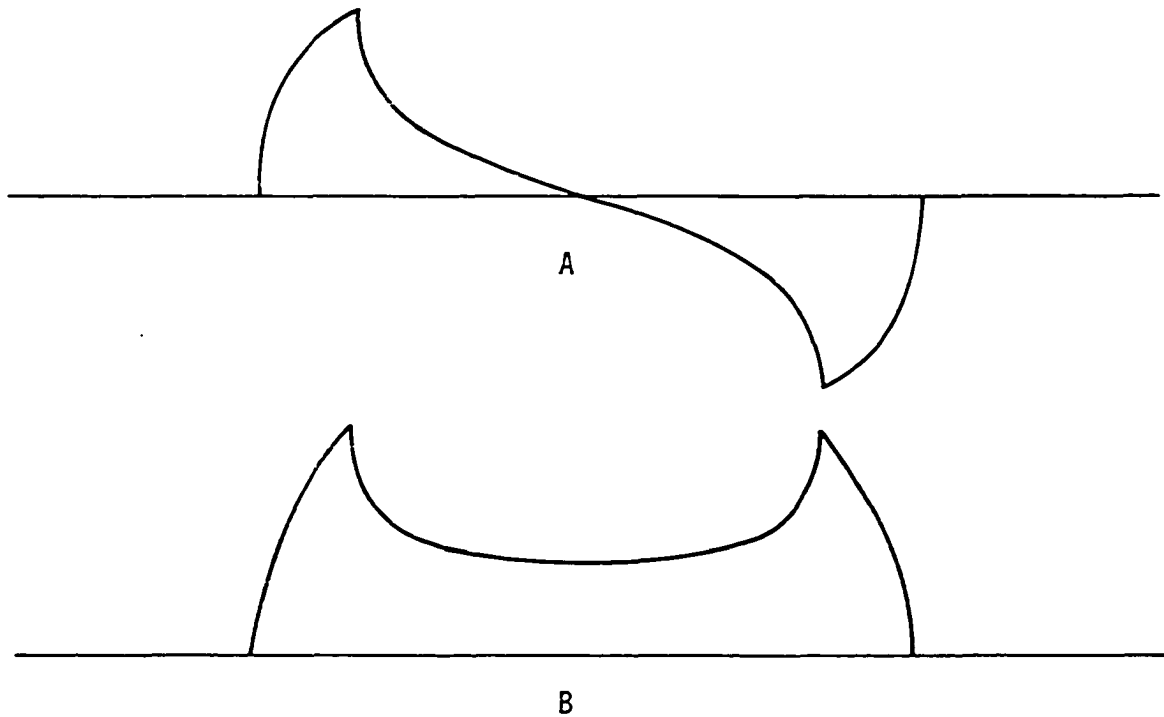


Figure VIII-6. Streamwise (A) and Lateral (B) Signals Predicted by the Simple Model for Kernel Size Assumed to Generate Figure VIII-4. Lateral Displacement Corresponds to $Y/R = 0.707$.

discrete representation was sufficiently accurate since as many points as were desired were available. The covariance for positive delays is shown in Figure VIII-7 for $R/\delta = 10$. Only positive delays are shown since the covariance is symmetric.

2. Fourier transformation

The Fourier transform of the covariance was required to establish the spectral components of the simple model signal. Since the covariance was symmetric, only the cosine transform was needed. Because the analytic form of the covariance was not available, a discrete approximation of the transform was used. Frequency components from zero to about seven times the fundamental frequency were evaluated. The cosine transform of the preceding covariance is shown in Figure VIII-8. The ordinate of the covariance and transform was $(e/SA\Delta_n)^2$ or $(\theta/\Delta_n)^2$. Δ_n was left as an unspecified parameter. The flame generated signals were divided by an assumed value of Δ_n to make the data consistent with the simple model analysis.

The total signal energy contribution was calculated by applying the appropriate filter transfer function to the transformation and summing over all frequencies of interest. This total energy was used in analysis of flame data.

Simple model data were generated for various ratios R/δ . The specification of an equivalent δ was required to provide the scale factor for all physical variables.

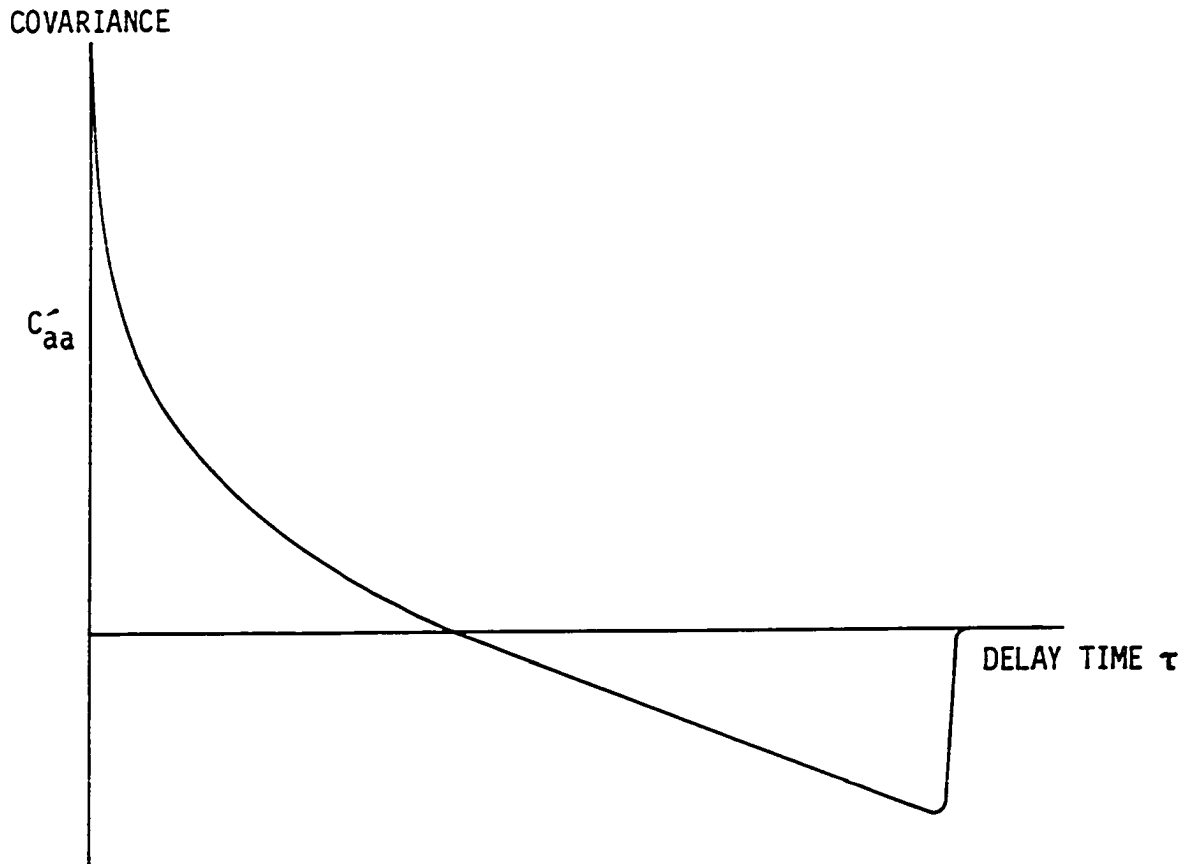


Figure VIII-7. Covariance (θ Mean Square) of Simple Model Signal for the Case $R/\delta = 10$.

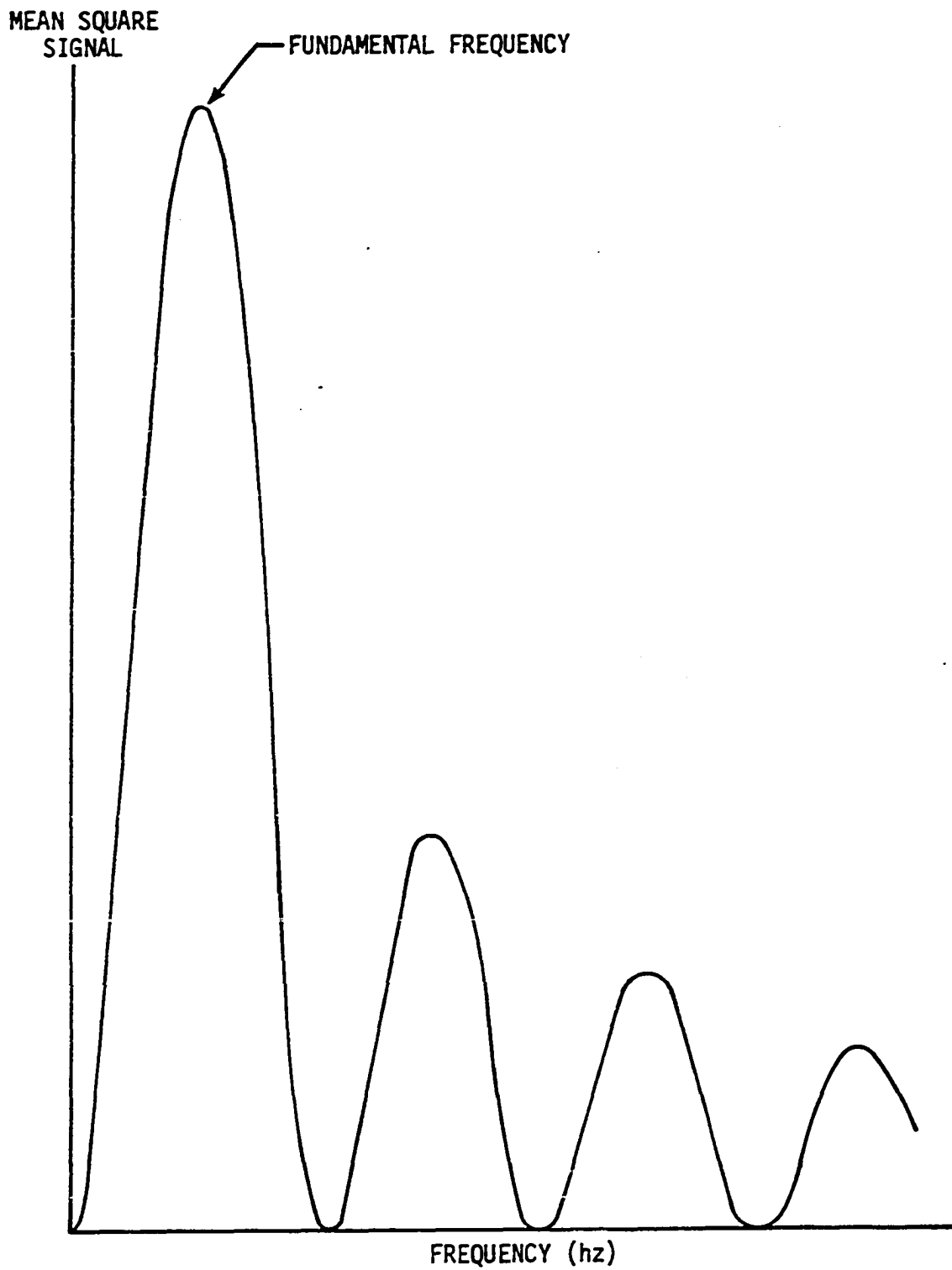


Figure VIII-8. Cosine Transform of Covariance of Simple Model Signal Shown in Figure VIII-6.

C. Derivation of Frequency Change
Due to Flame Front Motion

1. Converging flame front

If the discontinuity which separated the interior of the sphere from its surroundings was a flame front, the size of any kernel would change with time. If the size of a kernel changes, the fundamental frequency of its signal changes. The fundamental frequency of an expanding kernel decreases with increasing time while the fundamental frequency of a converging kernel increases with increasing time, the relationship between size and frequency was determined in the manner discussed in the previous section.

Assume a kernel of size $L(0)$ with a surface converging at a rate of V m/s. The size at any time will be $L(t) = L(0) - 2Vt$, or $L(\Delta Z) = L(0) - 2V\Delta Z/U_c$ where U_c is the mean convection speed. The speed of the front V is presumably a function of the size L , and the thermodynamic state of the kernel. The magnitude of the frequency change depends on the unknown parameter V .

Assume

$$\lambda \sim 2L$$

$$U_c = f\lambda = f2L$$

$$f = U_c/2L$$

$$f(0) = U_c/2L(0)$$

$$f(\Delta Z) = (U_c/2)(1/L(\Delta Z)) = (U_c/2)/(L(0) - 2V\Delta Z/U_c)$$

$$= f(0)U_c^2/(U_c^2 - 4V\Delta Zf(0))$$

$$\Delta f = f(\Delta Z) - f(0)$$

$$= f(0)U_c^2/(U_c^2 - 4V\Delta Zf(0)) - f(0)$$

$$f^2(0)4V\Delta Z/(U_c^2 - 4V\Delta Zf(0))$$

2. Diverging flame front

Assume the flame front is diverging and that the speed of the front relative to the unburned gas which surrounds it is V . The gas which burns at the front is constrained to be within the sphere. The rate of advance of the front relative to the center of the sphere is $(\rho_r/\rho_p)V$ where ρ_r is the density of the reactants and ρ_p is the density of the products of combustion. The size at any time becomes $L(t) = L(0) + 2(\rho_r/\rho_p)Vt$ or as above $L(\Delta Z) = L(Z) + 2(\rho_r/\rho_p)V\Delta Z/U_c$.

Assume

$$\lambda \sim 2L$$

$$f(0) = U_c/2L(0)$$

$$f(\Delta Z) = U_c/2L(\Delta Z)$$

$$= U_c/(U_c/f(0) + 2(\rho_r/\rho_p)V\Delta Z/U_c)$$

$$\Delta f = f(\Delta Z) - f(0)$$

$$= U_c/(U_c/f(0) + 2(\rho_r/\rho_p)V\Delta Z/U_c) - f(0)$$

$$= -4f^2(0)V\Delta Z/(U_c^2 + 4f(0)V\Delta Z(\rho_r/\rho_p)) \quad (\text{VIII-7})$$

The magnitude of the frequency change depends upon two unknown parameters, V and ρ_r/ρ_p , so the quantitative accuracy of the prediction is dubious. The most important facet of the prediction was not the magnitude but the direction of the frequency change. The fundamental frequency of the signal generated by a kernel with a converging flame front increases with time and the fundamental frequency of the signal generated by a kernel with a diverging flame front decreases with time. This fact was used in determining the flame front motion of the flame kernels.

D. Noncentral Beam-Kernel Interactions

1. Probability analysis

Most of the analysis in this paper dealt with the signals produced by central beam-kernel interactions. The probability of noncentral beam-kernel interactions and a few of the consequences of these will be discussed next.

For a kernel of size L to generate a signal in one assembly, its center must pass less than a distance $L/2$ from the beam center. The signal generated will be smaller, in peak magnitude and duration, the farther the kernel center passes from the beam. This can be seen in Figure VIII-9 where the Z component of the signal shown in Figure VIII-6 is superimposed on the signal shown in Figure VIII-5. Consider only kernels which generate signals in both assemblies. The kernel center must pass through the square of side L centered at the beam intersection with sides parallel to the beams as shown in Figure VIII-10.

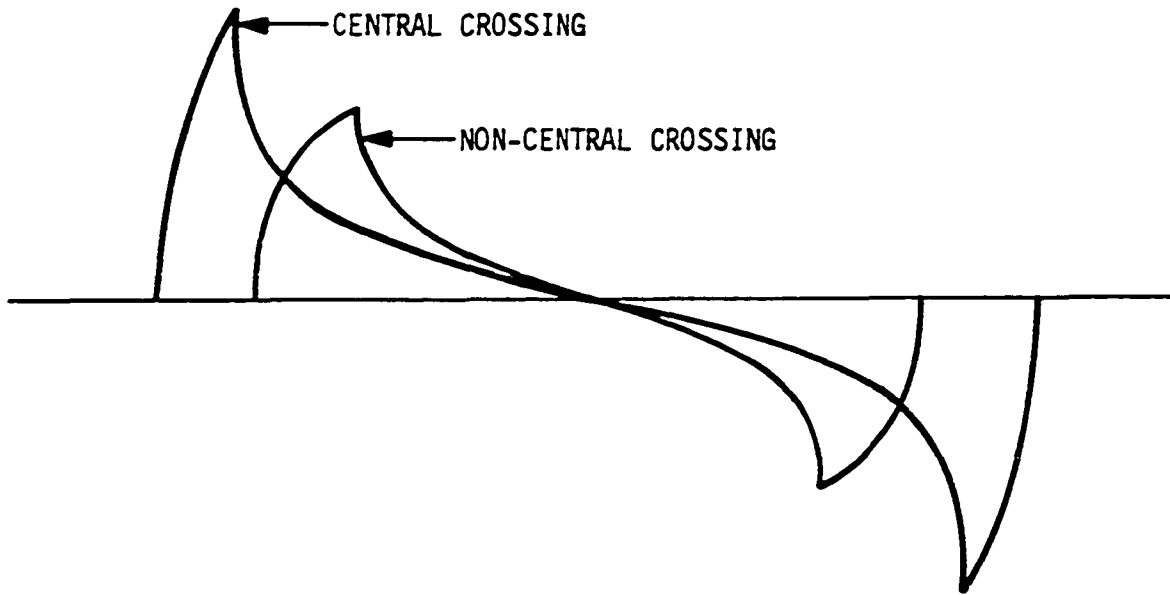


Figure VIII-9. Comparison of Simple Model Generated Streamwise Signal Components for Central and Non-Central Beam-Kernel Interaction.

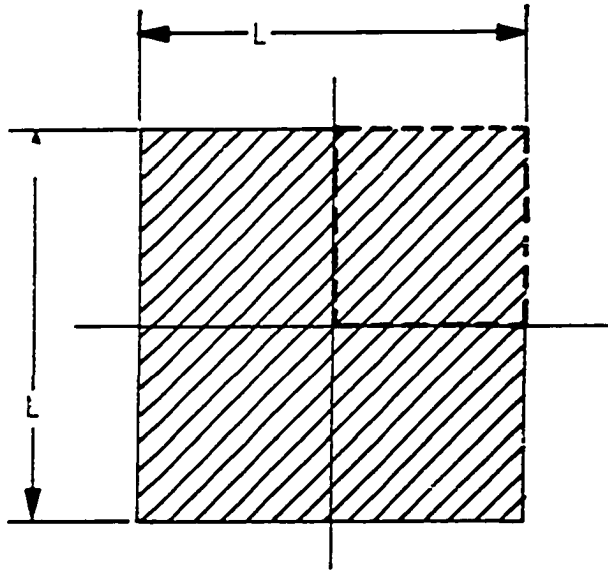


Figure VIII-10. Area Surrounding the Beam Intersection Through Which a Kernel Center Must Pass to Generate a Signal in Both Assemblies.

By symmetry, only one quadrant need be considered. The kernel center has no preferred location so all points in the square $0 < a < L/2$, $0 < b < L/2$ were equally likely. Mathematically, $P(a, b) = 4/L^2$. The apparent length of a signal was determined solely from the geometry of the interaction. The geometry and nomenclature used to determine the apparent length of a signal are shown in Figure VIII-11.

Recall

$$\frac{L_o^2}{4} = \frac{L_a'^2}{4} + a^2 \text{ or } L_o^2 = L_a'^2 + 4a^2 = L_b'^2 + 4b^2$$

$$P(L_a', L_b') = P(a, b) \begin{vmatrix} \frac{\partial a}{\partial L_a'} & \frac{\partial a}{\partial L_b'} \\ \frac{\partial b}{\partial L_a'} & \frac{\partial b}{\partial L_b'} \end{vmatrix}$$

$$a^2 = \frac{L_o^2 - L_a'^2}{4}$$

$$b^2 = \frac{L_o^2 - L_b'^2}{4}$$

$$a = \frac{1}{2} (L_o^2 - L_a'^2)^{1/2}$$

$$b = \frac{1}{2} (L_o^2 - L_b'^2)^{1/2}$$

$$\frac{\partial a}{\partial L_a'} = \left(\frac{1}{2}\right) \left(\frac{1}{2}\right) \frac{(-2L_a')}{(L_o^2 - L_a'^2)^{1/2}} \quad \frac{\partial b}{\partial L_a'} = 0$$

$$\frac{\partial a}{\partial L_b'} = 0 \quad \frac{\partial b}{\partial L_b'} = \left(\frac{1}{2}\right) \left(\frac{1}{2}\right) \frac{(-2L_b')}{(L_o^2 - L_b'^2)^{1/2}}$$

therefore

$$P(L_a', L_b') = \frac{4}{L_o^2} \begin{vmatrix} \frac{L_a'}{2} & 0 \\ \frac{L_b'}{2} & \frac{L_b'}{2} \\ 0 & \frac{L_b'}{2} \\ \frac{L_b'}{2} & 0 \end{vmatrix}$$

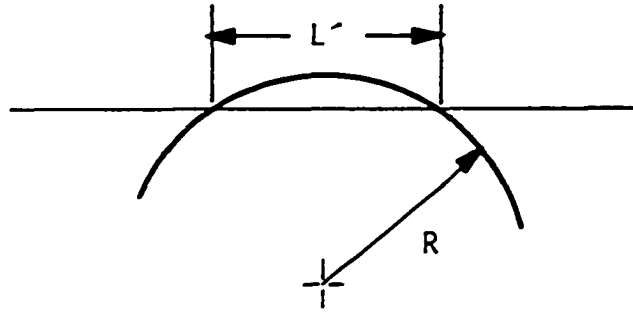


Figure VIII-11. Geometry and Nomenclature Used to Describe the Apparent Length of the Signal.

$$= \frac{L'_a L'_b}{L_o^2} \left| \frac{1}{(L_o^4 - L_o^2 L_a'^2 - L_o^2 L_b'^2 + L_a'^2 L_b'^2)^{1/2}} \right|$$

Let $\eta_a = \frac{L'_a}{L_o}$ $\eta_b = \frac{L'_b}{L_o}$

$$P(\eta_a, \eta_b) = \frac{\eta_a \eta_b}{(1 - \eta_a^2 - \eta_b^2 + \eta_a^2 \eta_b^2)^{1/2}}$$

$$a = 0, \eta_a = 1 \quad b = 0, \eta_b = 1$$

$$a = L_o, \eta_a = 0 \quad b = L_o, \eta_b = 0$$

It is easily verified that the probability is properly normalized.

The probability, $P(L, L)$, of identical size signals from the two assemblies was zero. This reflects the fact that the area of the two lines through the square which correspond to identical interactions was zero. If the lines are replaced by finite width bands, which corresponds to the signals being approximately but not exactly the same size, the probability was no longer zero. The total area of the square was L^2 . The area of the lines was $\epsilon(2\sqrt{2}L - 2\epsilon)$ where ϵ was the width of the lines. The probability was the ratio of these areas or $P(L, L) = 2\sqrt{2}\epsilon/L - 2(\epsilon/L)^2$. For any finite ratio of ϵ/L , the probability was not zero.

2. Interaction cross section

The interaction cross section was defined as the area centered at the beam intersection through which the kernel center must pass to generate a signal more like its true size than the next largest size. Assume the size corresponding to a particular frequency is L_1 and that

the size corresponding to the next higher measured frequency is L_2 . Define, somewhat arbitrarily, the size $(L_1 + L_2)/2$ to be the dividing point between signals which were more like L_1 and signals which were more like L_2 . The maximum distance \tilde{R} from the beam intersection which the center of a kernel of size L_1 could pass and generate a signal of size greater than $(L_1 + L_2)/2$ was the radius of the interaction cross section. The magnitude of \tilde{R} depended on the sizes L_1 and L_2 only. These sizes were determined by the frequencies and the convection speed. The simple model was used to determine the corresponding size for each frequency. The interaction cross section is illustrated in Figure VIII-12. The shaded area in the center is the interaction cross section. Only one beam is shown for clarity. Let $\tilde{L} = (L_1 + L_2)/2$. Then

$$\begin{aligned} \frac{L_1^2}{4} &= \frac{\tilde{L}^2}{4} + R^2 \\ \tilde{R}^2 &= \frac{L_1^2}{4} - \frac{\tilde{L}^2}{4} \\ &= \frac{L_1^2}{4} - \frac{(L_1 + L_2)^2}{4} \\ &= \frac{L_1^2}{4} - \frac{L_1^2 + 2L_1L_2 + L_2^2}{4} \\ &= \frac{L_1^2}{4} - \frac{1}{4} \left(\frac{L_1^2 + 2L_1L_2 + L_2^2}{4} \right) \\ &= \frac{L_1^2}{4} - \frac{L_1^2}{16} - \frac{L_1L_2}{8} - \frac{L_2^2}{16} \\ &= (3L_1^2 - 2L_1L_2 - L_2^2)/16 \\ I &= \pi \tilde{R}^2 = \frac{\pi}{16} (3L_1^2 - 2L_1L_2 - L_2^2) \end{aligned}$$

The interaction cross section, I , was used in Section V-E-2.

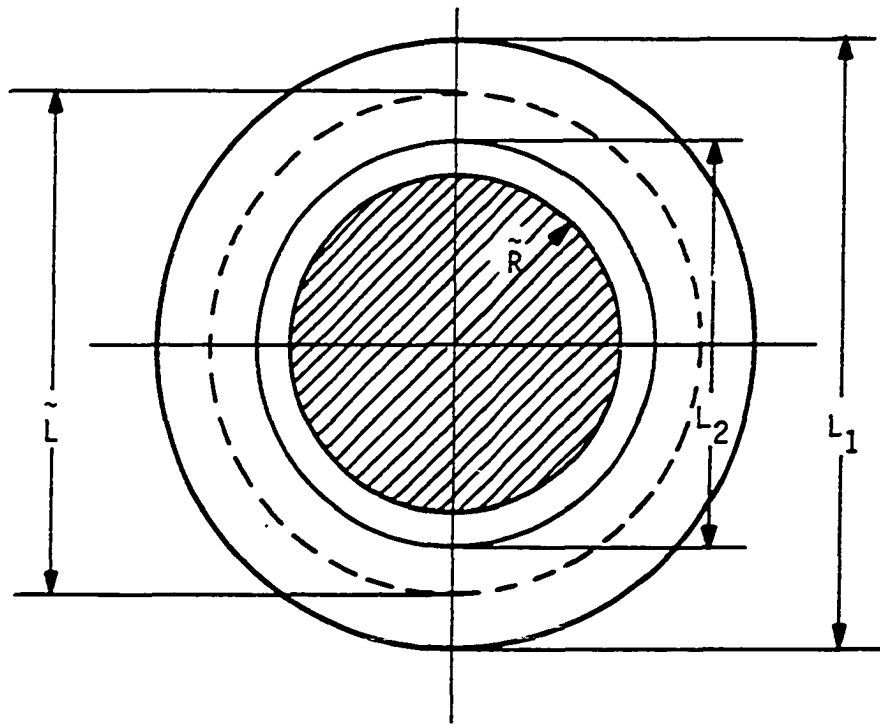


Figure VIII-12. Geometry of Beam-Kernel Interaction, Viewed from above, as Used to Determine the Interaction Cross-Section. Shaded Area Represents Interaction Cross-Section.